PARTICLE HYDRODYNAMIC INTERACTIONS IN INTERMEDIATE REYNOLDS NUMBER FLOWS

A Dissertation

Presented to the Faculty of the Graduate School

of Cornell University

in Partial Fulfillment of the Requirements for the Degree of

Doctor of Philosophy

by

Açmae El Yacoubi

January 2013

PARTICLE HYDRODYNAMIC INTERACTIONS IN INTERMEDIATE REYNOLDS NUMBER FLOWS

Açmae El Yacoubi, Ph.D.

Cornell University 2013

Collective behavior and self-organization are ubiquitous mechanisms in nature. From animate creatures, such as swarming insects, flocking birds and schooling fish, to inanimate natural processes such as sedimentation and cloud formation, these phenomena arouse the curiosity of physicists and engineers alike. Early studies using analytical models and experiments in the low Reynolds number helped shed the light on the intricacies of particle interactions, as in clouds or arrays of spheres. In the intermediate Reynolds number regime however, the unsteadiness introduced by the fluid inertia, coupled to the object dynamics, add to the complexity of the problem. Numerical methods become then the tool par excellence to solve for these dynamics.

The goal of this thesis is to lay out the foundations for a better understanding of particle interactions in fluids. Namely, we investigate the two-dimensional dynamics of interacting particles in a viscous fluid, in the intermediate Reynolds number range. We develop a direct numerical scheme based on the Immersed Interface Method to simulate the coupling of the dynamics of freely moving objects with the surrounding fluid. The method is used to study the dynamics of arrays of cylinders settling under gravity, and how these dynamics depend on the number of particles and their initial separation. We then provide a simple force law model which accounts for the initial repulsive force experienced by any two adjacent cylinders, at close range.

When the particle density is high, collisions are almost inevitable. To treat close range interactions and resolve the interstitial flow in the narrowing gap between particles or between a particle and a wall, we further extend the immersed interface method to take into account the lubrication effects. We solve Reynolds equations and use the analytical solution in the lubrication region. Doing so enables us to avoid *ad hoc* methods where an artificial repulsive force is added or two-dimensional collision equations are used with a modified coefficient of restitution.

BIOGRAPHICAL SKETCH

Born in 1984 in Agadir, Morocco, Açmae exhibited early signs of inquisitiveness and love for math. Her first toys were letters and numbers and she learned how to read and write at the age of two. No wonder she developed myopia since the tender age of five. Growing up with her younger brother and raised by a single parent (father) since the age of four, her childhood was shaped by rigorous discipline and a strong attachment to her nuclear family.

At the age of seventeen, she left her nest to pursue higher education in France, quite a challenging task for a lone minor, in a foreign culture. Two years in Paris for Classes Préparatoires aux Grandes Écoles proved to be the toughest academic experience she ever had. After successfully passing the nation-wide written and oral exams, she entered her dream Grande École, École Nationale Supérieure de l'Aéronautique et de l'Espace (Supaéro) in Toulouse, which as you might have guessed, is a three-year school for Aerospace Engineering. She graduated in October 2006, with both a Diplôme d'Ingénieur in Aeronautical Engineering and a Master's Degree in Fluid Mechanics. Açmae's Master's thesis was on the flight dynamics of damselflies and she wanted to further learn about these creatures and their fascinating flight prowess. So, a PhD seemed to be reasonable. However, her father unexpectedly fell ill and she decided to spend a sabbatical year during 2007 to look after him, while applying for graduate school at Cornell University.

Açmae got accepted into the PhD program of the formerly known department of Theoretical and Applied Mechanics, to work with Prof. Z. Jane Wang. While in Ithaca, she realized how pasty white her skin actually was given the lack of sunlight, how locals are addicted to local food and dance festivals, and how it is almost impossible to access campus without crossing a spectacular

gorge.

Besides her studies, Açmae is an avid sport and outdoors young lass. A runner by nature, she picked up cycling, and combined the two into triathlons. Competitive running and cycling helped her keep her mental sanity and enabled her to make her best friends in Ithaca. Açmae is also a seasonal backpacker, a newly converted weight-lifter and a former skydiver, with fifty bird's-eye-view jumps over Southern France and ... Ovid, NY.

Finally, Açmae is a language whiz, speaking six languages, Moroccan Arabic, Classical Arabic, French, English (Ah! The obvious ...), Hebrew and Spanish, and is continuously seeking to improve on or learn new languages.

To my beloved dad, Kamal, who has always had a blind confidence in me.

To my brother, Yahia, who I like to call my siamese twin.

ACKNOWLEDGEMENTS

Completing my PhD degree is the culmination of twenty-five years of academics, and is probably the most challenging undertaking in my academic life. Yes. Even more than the Classes Préparatoires. The best and worst moments of this seemingly Sisyphean endeavor were shared with people who are dear to me and who I would like to thank.

My thanks go first to my thesis adviser, Prof. Z. Jane Wang, who has shown patience and provided valuable guidance during the past four years. Our journey has been quite hectic, with memorable moments. Despite my initial trouble settling onto a thesis project, Jane has shown flexibility and tried me on several projects until I found something suitable. There were probably more troughs than crests during these years, yet, Jane decided to keep me on board, and I thank you for that Jane. I also would like to thank Prof. Sheng Xu, who proved to be an outstanding listener and mentor, and who provided insightful discussions and advice when everything seemed to hit a dead end. My thanks also go to my minor committee members, Prof. Don Koch and Prof. John Guckenheimer, two fountains of knowledge in their respective fields, for their insightful discussions and general suggestions.

I also would like to thank my previous labmates who, although I got to know for only two years, have been great listeners, tutors and chums: Attila and Gordon. Speaking of which, a shameless plug to Attila's Paprika-laden-Hungarian Goulash: the best. Period. Additionally, I wish to express my heartfelt appreciation to the departments of Theoretical & Applied Mechanics (T&AM), and Mechanical & Aerospace Engineering for their four-year support through Teaching Assistantships. It is amazing how much savings a graduate student can make on a measly stipend, and I thank you not only for your continuous financial

support during these years, but also for giving me the unique opportunity to teach students, develop and hone my teaching skills. This is by far one of the most valuable experiences I have had at Cornell University. Thank you.

Sincere thanks to my T&AM friends: Prof. Wolfgang Sachse, a great mentor, listener and upbeat person, who provided advice and help, from academic/career choices to photography. Thank you. Oh, and you still owe me a dinner at the lake house! Profs. Leigh Phoenix and Herbet Hui for their funny and lively non-academic discussions in the lounge; Cindy who left us so quickly but was the most efficient staff, and who introduced me to strawberry picking with her lovely family; the "Tammies" for their commiseration among others, especially Chris, Hiba, David, Pranav and Sanjay.

Special thanks go to all my cycling, running, swimming and weight-lifting friends for their great mental support, their incommensurable camaraderie, their training tips, support and the escape from research they provided: Naama, Gilly, Tal & Roy, Gil and Ofer for the century lake rides, LiLynn, Juan "Cycloblogger", Glenn "the bike-whiz" Swan, the Velo Bellas!, Andrejs for his BPAC support on my accident on the steel-bridge-of-death, the Cornell Cycling Club (2009-2011), the Finger Lakes Running Club, The Ithaca Triathlon Club, Veronica and Lines 5 & 6 at Teagle, and my friends from the weight room.

Last but not least, I will forever be indebted to my best of the best friend, accomplice and father, Kamal, who showered me with unconditional love, support and blind confidence since an early age. Thank you to my beloved brother and other best of the best friend, Yahia, who has always believed in my achievements and encouraged me to keep a level head during dark moments. I hope I am living up to their expectations and I dedicate this dissertation to them as an expression of my heartfelt gratitude.

TABLE OF CONTENTS

LIST OF TABLES

LIST OF FIGURES

OVERVIEW

The literature is rich with studies on particle interaction in Stokes flow. However, there are scant studies on particle interaction at intermediate Reynolds numbers. In this thesis, we present a new computational scheme to simulate the dynamics of the particles coupled to the Navier-Stokes solutions for the fluid. In order to understand the basic picture of particle-particle interactions in fluid, we investigate the dynamics of an array of freely falling cylinders with an initial spacing on the order of the particle diameter. We find that for a small number of particles ($n = 3,\ 4$), there are two distinct falling configurations which depend on the parity of n. For $n > 4$, the falling configuration is a mix of those previous modes. However, when the initial spacing between particles is below a threshhold, the array disintegrates into small clusters of 2 or 3 particles. We further quantify the pairwise interaction force between two falling particles as a function of their relative position, and compare them with results in the Stokes regime.

When the spacing between particles or between a particle and a wall falls below a certain threshold, the numerical code breaks down. To circumvent this problem, we implement a new scheme to resolve the hydrodynamic interactions using lubrication theory. This method enables us to handle collisions without resorting to the addition of *ad hoc* repulsive forces. Our implementation is then used on three fundamental cases on normal and oblique collisions between a particle and a wall. An additional case, featuring particle-particle collisions is presented as well.

CHAPTER 1

COMPUTATIONAL STUDY OF THE INTERACTION OF FREELY MOVING PARTICLES AT INTERMEDIATE REYNOLDS NUMBERS

Most of the material in this chapter can be found in the paper "Computational study of the interaction of freely moving particles at intermediate Reynolds numbers", published in the August 2012 special edition of the Journal of Fluid Mechanics, dedicated to Professor T. J. Pedley on his 70^{th} birthday [18].

1.1 Introduction

Collective behavior and self-organization of particles subject to hydrodynamic interactions are common among a wide range of biological systems and organisms, such as swarming, schooling or flocking [10, 47]. Hydrodynamic interactions play an important role in micro-organism colony growth through clustering mechanisms [8, 12, 14, 23, 49] and in diffusive mixing [27, 38, 40, 52, 56]. Collective dynamics of particles is also central to physical phenomena such as cloud formation, particle suspension and particle sedimentation [24, 58].

At low Reynolds numbers, where the flow is governed by Stokes equations, there has been extensive theoretical, numerical and experimental studies of hydrodynamic interactions of large collections of particles [11, 17, 28, 30, 31, 41]. The linearity of Stokes equations permits the use of the superposition of fundamental solutions known as stokeslets [25]. For instance, recent work has shown that a spherical cloud of particles settling in a viscous fluid spreads, and eventually evolves into a toroidal shape and separates into a cascade of smaller clumps [17].

In contrast, at intermediate Reynolds numbers, the dynamics of the particles are further complicated by the fluid inertia, which introduces the unsteadiness to these problems. There have been relatively few studies on particle interactions and clustering [4, 13, 33] and there appears to be a need to explore the rich dynamics of collections of particles in this regime.

In the present chapter, we perform a numerical investigation of multiple interacting particles in the intermediate Reynolds number range. The goal here is twofold. First, we introduce a new numerical method for solving the two-dimensional Navier-Stokes equation in the presence of freely moving particles of arbitrary shapes. The method is a further development of our previous immersed interface method [59, 60, 62] and allows for simultaneous solution to the dynamics of the particles and the fluid. The method for coupling the fluid and solid dynamics does not introduce additional constraints on the integration time step, hence allowing for an efficient simulation of multiple, arbitrarily moving particles. The second goal is to discover a rich set of new dynamics of multiple particles, interacting in a fluid, in the intermediate Reynolds number range. In particular, we will focus on the dynamics of arrays of falling cylinders, starting from different initial conditions.

1.2 Method

To simulate the dynamics of cylinders settling under gravity, we further develop the immersed interface method to simulate the interaction of a fluid with free moving particles. In the previous work done by Xu and Wang [59, 60], the motion of the rigid objects was prescribed. Here, the dynamics of the freely

moving rigid objects are coupled with those of the surrounding fluid. In what follows, we introduce an iterative scheme in the immersed interface method to handle this coupling without reducing the accuracy and stability of the method.

1.2.1 Equations of motion

The equations of motion for the fluid are governed by the Navier-Stokes equations subject to boundary conditions on the surfaces of the objects. The dynamics of the immersed objects are governed by Newton's equations. The motions for the fluid and the objects are coupled through the boundary conditions at the objects. In the formulation of the immersed interface method, the fluid velocity $\vec{v}$ and pressure p outside an object (multiple objects are considered similarly) satisfy:

$$\frac{\partial \vec{v}}{\partial t} + \vec{v} \cdot \nabla \vec{v} = -\nabla p + \frac{1}{Re} \nabla^2 \vec{v} + \int_\Gamma \vec{f}(\alpha, t)\, \delta(\vec{x} - \vec{X}(\alpha, t))\, d\alpha \tag{1.1a}$$

$$\nabla \cdot \vec{v} = 0 \tag{1.1b}$$

where $\vec{f}$ is the density of a singular force which enforces the boundary condition on the boundary Γ of the object. The boundary Γ is parameterized by α as shown in figure 1.1, $\delta(.)$ is the 2D Dirac delta function, $\vec{x} = (x, y)$ are the Cartesian coordinates of the Eulerian fluid, and $\vec{X}(\alpha, t)$ are the Cartesian coordinates of Lagrangian points on the boundary.

The rigid object is modeled as a rigid fluid. Thus, the velocity of a fluid particle inside the object is $\vec{v} = \vec{v}_c + \vec{\Omega} \times \vec{r}$, where $\vec{\Omega}$ is the angular rotation of the object (in 2D, $\|\vec{\Omega}\|_2 = \dot{\theta}$) and $\vec{r} = \vec{x} - \vec{x}_c$ is the relative position of the fluid particle to the center of mass $\vec{x}_c$ of the object. Hence, the acceleration of the fluid particle

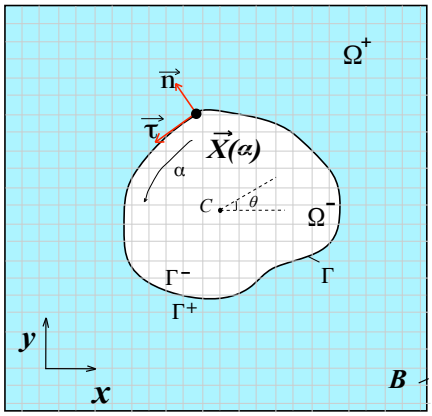

Figure 1.1: *Computational domain of an object immersed in a fluid.*

is

$$\frac{d\vec{v}}{dt} = \underbrace{\frac{d\vec{v}_c}{dt} + \vec{\Omega} \times (\vec{\Omega} \times \vec{r})}_{-\nabla p} + \underbrace{\frac{d\vec{\Omega}}{dt} \times \vec{r}}_{\vec{f}_b}. \tag{1.2}$$

The first two terms can be expressed as a pressure gradient and the last term is an additional body force $\vec{f}_b$ associated with the angular acceleration of the object. Inside the object, $\nabla^2 \vec{v} = \vec{0}$, and the pressure is

$$p = -\frac{d^2 x_c}{dt^2} x - \frac{d^2 y_c}{dt^2} y + \frac{1}{2} \Omega^2 \left((x - x_c)^2 - (y - y_c)^2 \right). \tag{1.3}$$

Finally, the equations of motion for the object are:

$$m_s \dot{\vec{v}}_c = \vec{F}_{ext} + \vec{F}_f \tag{1.4a}$$

$$I^* \ddot{\theta} = T_f \tag{1.4b}$$

where m_s is its mass, I^* moment of inertia with respect to its center of mass, $\vec{F}_{ext}$ is the external non-fluid force on the object, $\vec{F}_f$ is the fluid force on the object, and T_f is the fluid torque on the object with respect to its center of mass. Equations (1.1 – 1.4) constitute the coupled equations for the fluid and the solid that we will solve.

The singular force distribution in equation (1.1a) is related to the jumps in the

fluid variables and their derivatives across the fluid-object interface [59, 60, 61]. The tangential and normal components of the singular force in equation (1.1a) are given by

$$f_\tau = \vec{f} \cdot \vec{\tau} = -\frac{1}{Re}\left(\vec{\tau} \cdot \left.\frac{\partial \vec{v}}{\partial n}\right|_{\Gamma^+} - \frac{d\theta}{dt}\right) \tag{1.5a}$$

$$f_n = \vec{f} \cdot \vec{n} = \int \left(\frac{1}{Re}\left.\frac{\partial \omega}{\partial n}\right|_{\Gamma^+} + [\vec{f_b}] \cdot \vec{\tau}\right) J \, \mathrm{d}\alpha \tag{1.5b}$$

where $\omega = (\partial v/\partial x) - (\partial u/\partial y)$ is the vorticity, $\vec{\tau} = (\partial \vec{X}/J\partial\alpha)$, $(J = \|\partial \vec{X}/\partial\alpha\|_2)$ and $\vec{n}$ are the unit tangent and unit normal vectors to the boundary Γ, the brackets $[\cdot] = (\cdot)_{\Gamma^+} - (\cdot)_{\Gamma^-}$ are used to denote a jump across the interface, and the jump in the tangential component of the body force in equation (2.13b) is

$$[\vec{f_b}] \cdot \vec{\tau} = -\frac{d^2\theta}{dt^2}\left((X - x_c)\tau_y - (Y - y_c)\tau_x\right) . \tag{1.6}$$

The fluid force and torque acting on the object can be expressed through the integrals of the singular force

$$\vec{F}_f = -\int_\Gamma (f_\tau \vec{\tau} + p^+ \vec{n}) \; J \mathrm{d}\alpha \tag{1.7a}$$

$$\vec{T}_f = -\int_\Gamma (\vec{X} - \vec{x_c}) \times (f_\tau \vec{\tau} + p^+ \vec{n}) \; J \mathrm{d}\alpha \, . \tag{1.7b}$$

1.2.2 Dimensionless Parameters

In the computations presented here, we non-dimensionalize the equations by ρ_f, the fluid density, L, a reference length of the object (diameter of the cylinder, width of the plate), V, a reference velocity (terminal velocity of a falling object, associated with a unit-coefficient drag force), and $T = L/V$, the corresponding time scale. The Reynolds number Re is defined as $Re = \rho_f VL/\mu$, where μ is the dynamic fluid viscosity. The non-dimensional mass of the object is $m_s = \gamma \mathcal{A}$,

where $\gamma = \rho_s/\rho_f$ is the density ratio between the object and the fluid, and $\mathcal{A}$ is the nondimensional area of the object. In the cases studied next, $\vec{F}_{ext} = (m_s - m_f)\,\vec{g}$ is the buoyancy-corrected weight, where m_f is the mass of the displaced fluid. The non-dimensional gravity is $\overline{g} = gL/V^2$, where $g = \|\vec{g}\|_2$ is the gravitational constant. Because the reference velocity is obtained by equating the buoyancy-corrected weight of the object with a unit-coefficient drag force acting on it, $V = \sqrt{2(\gamma-1)gL\mathcal{A}}$, $\overline{g}$ depends only on the density ratio and the geometry of the object, $\overline{g} = 1/(2(\gamma-1)\mathcal{A})$. The buoyancy-corrected weight on the object become, in non-dimensional form, $\vec{F}_g = (\gamma-1)\mathcal{A}\overline{g}$. As we can see from our dimensional analysis, there is a total of five non-dimensional parameters, $Re, \overline{g}, \gamma, n, d_0$. In this study, we only focus on the effect of the number of objects, n, and the initial inter-particle center-to-center spacing, d_0, on the dynamics.

1.2.3 Numerical implementation

In the immersed interface method, equations (1.1a – 1.1b) are solved on a fixed grid by incorporating jump conditions across fluid-object interfaces into a numerical scheme [61]. The jump conditions are induced by and related to singular forces. A main difficulty in the numerical treatment of a freely moving object, compared to an object under prescribed motion [59, 60], is the coupling of the dynamics of the fluid with the object. The pressure external to the object depends explicitly on the normal component of the singular force, and thus the angular acceleration of the object, as implied by equation (2.13b). The angular acceleration, in turn, depends on the pressure.

The pair of unknown variables, the pressure **p** in the fluid, and the angular

acceleration $\mathbf{q}$ of the freely moving objects in the fluid, are governed by two coupled linear systems:

$$\begin{cases} L\mathbf{p} + C\mathbf{q} &= \mathbf{r} \\ \mathbf{q} &= S\mathbf{p} + \mathbf{d} \end{cases} \tag{1.8}$$

where $\mathbf{p}$ is the pressure defined on a discrete lattice, $\mathbf{q}$ is the vector formed by the angular acceleration of all the objects, L is a discrete Laplacian, C and S are coupling matrices, and $\mathbf{r}$ and $\mathbf{d}$ are known vectors. To solve the coupled systems efficiently, we apply an augmented variable approach [43] using the Generalized Minimal Residual Method (GMRES). By eliminating $\mathbf{p}$ from equation (1.8), we obtain the Schur-complement system for $\mathbf{q}$:

$$(I + SL^{-1}C)\mathbf{q} = \mathbf{d} + SL^{-1}\mathbf{r} \tag{1.9}$$

where I is the identity matrix. $\mathbf{q}$ can be solved for iteratively using GMRES, and consequently, $\mathbf{p}$ can be determined from equation (1.8).

We note that the GMRES iteration does not require the explicit form of L, C, S and $I + SL^{-1}C$. Instead, it only needs the matrix-vector product $(I + SL^{-1}C)\,\mathbf{q}^{(k)}$, where $\mathbf{q}^{(k)}$ is a guess solution at the k^{th} step. In the k^{th} step, we use the guess solution $\mathbf{q}^{(k)}$ to solve for $\mathbf{p}^{(k)}$, and use $\mathbf{p}^{(k)}$ to compute $\mathbf{q}^{(k+1)}$. It can be shown that the right-hand side vector $\mathbf{d} + SL^{-1}\mathbf{r}$ in the Schur-complement system is $\mathbf{Q}_0$, where $\mathbf{Q}_0$ is the value of $\mathbf{q}$ after the first iteration with zero initial guess. The matrix-vector product $(I + SL^{-1}C)\,\mathbf{q}^{(k)}$ in the k^{th} step is

$$(I + SL^{-1}C)\,\mathbf{q}^{(k)} = \mathbf{Q}_0 - \mathbf{q}^{(k+1)} + \mathbf{q}^{(k)}\ .$$

The GMRES iteration converges when $\mathbf{q}^{(k+1)} = \mathbf{q}^{(k)}$.

With the exception of the handling of the coupling between the fluid and the objects, the remainder of the numerical implementation in the present study

is similar to that in [59]. The momentum equations (1.1a), are solved using finite differences on a MAC grid. The time integration is an explicit fourth-order Runge-Kutta scheme, and the discrete pressure Poisson equation is solved via a Fast-Fourier Transform (FFT).

We carried out a grid-resolution analysis to test the convergence of our current implementation. The results show that it is second-order accurate, including along the boundaries of the objects. In addition, we observe that GMRES used in solving the Schur-complement system converges in only a few iterations, even for a large number of freely moving objects.

1.2.4 Validation of the numerical code

The novel aspect of our current implementation of the immersed interface method is the ability to handle freely moving objects in a fluid. To validate the new features of our code, we compare our results with experiments of freely fluttering and tumbling plates.

Andersen et *al* [1, 2] and Pesavento & Wang [50] experimentally and numerically investigated the dynamics of falling rectangular plates. Their study provides qualitative and quantitative data on different falling modes, including fluttering, tumbling and chaotic motion, which we use to test the current code. In our simulations, we use rounded-rectangular plates, similar to the experimental geometry, as opposed to ellipses [50]. The rounded plate has a smaller curvature at the tips and can be resolved numerically with fewer grid points. Given the difference in the plate geometry, and in order to match both the thickness-to-width ratio β and the non-dimensional moment of inertia

parameters	fluttering	tumbling
$(\beta\,,I^*\,,Re)$	$(\frac{1}{14}\,,0.16\,,1147)$	$(\frac{1}{5}\,,0.48\,,737)$
θ_0	20°	45°
$(\dot{x}_c,\dot{y}_c,\dot{\theta})_{t=0}$	$(0,0,0.5)$	$(0,0,0.5)$

Table 1.1: *Simulation parameters for the fluttering and tumbling motion of a rounded-rectangular plate, using the immersed interface method.*

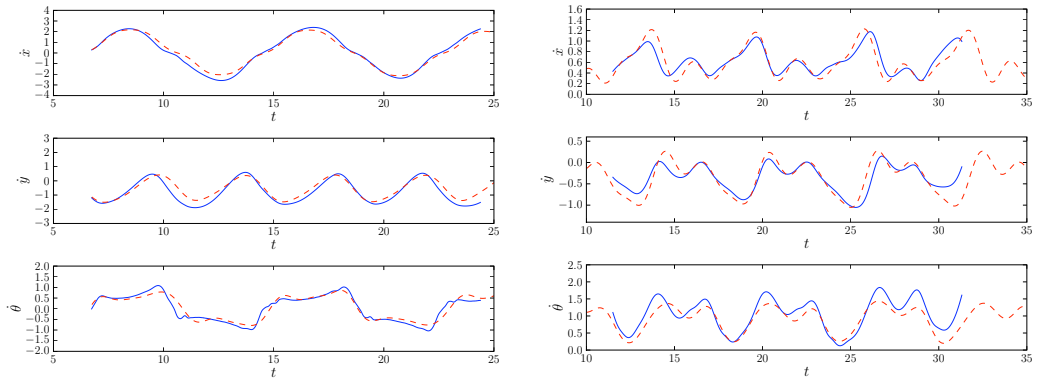

(a) *Fluttering* (b) *Tumbling*

Figure 1.2: *Comparison between experiments in [2] (dashed, red) and the current simulations (solid, blue) of a fluttering plate with* $I^* = 0.16$, $Re = 1147$, $\beta = 1/14$ *and a tumbling plate with* $I^* = 0.48$, $Re = 737$ *and* $\beta = 1/5$. *From top to bottom: x-velocity, y-velocity and angular velocity,* $\dot{\theta}$, *of the plate.*

$I^* = I/\rho_f L^4$, the density of the plates in the current study is slightly different from that in the experiments. The length scale is the width of the plate, the velocity scale is defined as the terminal velocity of the plate falling with unit drag coefficient, $V = \sqrt{2(\gamma-1)g\mathcal{L}\mathcal{A}}$, and the time scale is $T = L/V$. We reproduce the fluttering and tumbling cases in [2] and summarize our comparisons on figure 1.2 and table 1.2. In these computations, the grid resolution is 1600×3200, for a 10×20 domain size, and the time step is $\Delta t = 5\,10^{-3}$. In both cases, at steady state, the results match very well and the small difference may be attributed to the plate geometry.

parameters	**Andersen et *al* [2]**	**Current**
$(< \dot{x}_c >, < \dot{y}_c >, < \dot{\theta} >)$	(0.60 , −0.34 , 0.88)	(0.58 , −0.37 , 0.99)
Descent slope	29.2°	29.6°
Period: (short glide, long glide)	(1.1 , 3.2)	(1.2 , 3.5)

Table 1.2: *Comparison between experimental results in [2] and the current numerical results for a tumbling plate.* $< \dot{x}_c >$, $< \dot{y}_c >$ *and* $< \dot{\theta} >$ *are the average horizontal, vertical and angular velocities, respectively.*

1.3 Dynamics of arrays of settling cylinders in a 2D flow

In this section, we simulate horizontal arrays of settling cylinders at Reynolds number 200 and investigate the falling pattern and the connection between the dynamics of the particles and of the flow.

At zero Reynolds number, an array of settling spheres can exhibit a rich set of dynamics due to instabilities when the number of particles is sufficiently large [11, 30, 31, 45]. For example, Jayaweera & Mason [30] observed that clusters of less than seven spheres remain in a horizontal plane during the fall, spread out and the spheres tend to arrange themselves into regular polygonal shapes. More recently, Metzger et *al* [45] found that a spherical cluster of spheres settling under gravity in a viscous flow, is unstable and evolves into a torus before breaking up into smaller clusters.

At intermediate Reynolds numbers, the interactions between particles are complicated by the inertial effects. In our case, each cylinder will create a wake that extends for many diameter lengths and lead to non-local and time-dependent interactions. The forces experienced by each cylinder will be unsteady. It is therefore unclear, for a given set of initial conditions, whether the cylinders will approach a steady state, and how the steady state configuration

might depend on the initial arrangement. The steady state of a single particle is attained when the mean velocity, averaged over each period, is constant.

Finally, the study in this chapter is restricted to the cases where there is no collision and where the distance between particles can be well resolved by the immersed interface method. For cases where the initial spacing is sufficiently small, we observe that the particles are likely to collide in close encounter. To resolve the collision dynamics, we developed a method using lubrication theory to treat the thin layer between the particles. This scheme has been tested on fundamental scenarios involving normal and oblique collision between a cylinder and a wall, as well as between two approaching cylinders. Details can be founds in Chapter 2.

1.3.1 Falling pattern at steady state

In what follows, we study the dynamics of a horizontal array of n falling cylinders. We present a qualitative comparison of the falling patterns of the array. First, we fix the initial spacing, d_0, and vary the number of cylinders $n \in \{3, 4, 5, 6, 7, 8\}$. At any time, the spacing d is defined as the distance between the centers of two adjacent cylinders, hence $d = D + l$ where D is the diameter and l is the closest distance between their interfaces. The grid size and the time step are fixed at $\Delta x = \Delta y = 1/40$ and $\Delta t = 5\,10^{-3}$, respectively. We choose no-slip boundary conditions on all four fixed walls of the domain. This avoids specifying the far-field boundary conditions on a finite computational domain, in an unbounded fluid, which would involve modeling the wake of the objects. Figure 1.3(a) shows trajectories of the settling cylinders. When n

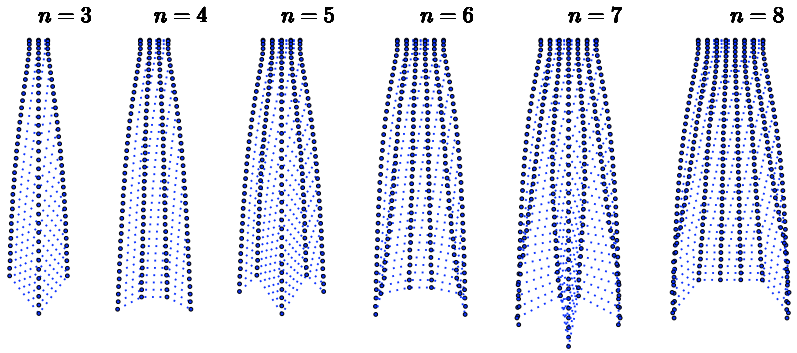

(a) Effect of n

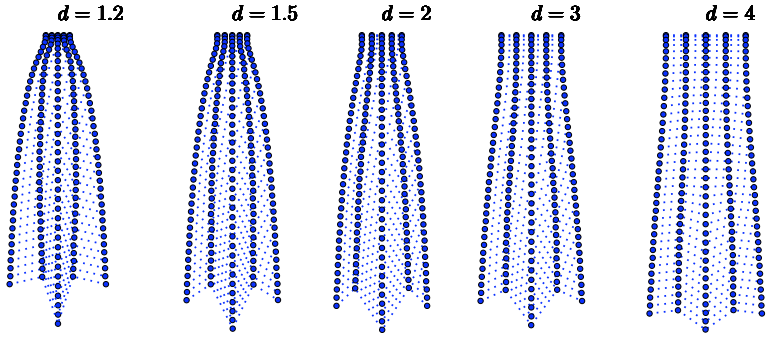

(b) Effect of d_0

Figure 1.3: *Effect of the number of cylinders, n, and the initial spacing, d_0, on the array falling pattern. (a) $d_0 = 2$ is fixed. (b) $n = 5$ is fixed. Snapshots are taken every $\delta t = 2$.*

is odd, the middle cylinder is always leading. Conversely, when it is even, the falling shape of the array at steady state is concave-down, provided that the initial spacing is not too small and no collisions occur. Regardless of the value of n, at steady state, the array displays a left and right mirror symmetry in the vortex shedding pattern and correspondingly, a mirror symmetry in the particle rotation. In other words, two particles symmetric about the centerline rotate in opposite directions and shed counter-rotating vortices (figure 1.5). This is consistent with the conservation of the total circulation, noting that particles are initially dropped with zero angular momentum. This claim has been checked

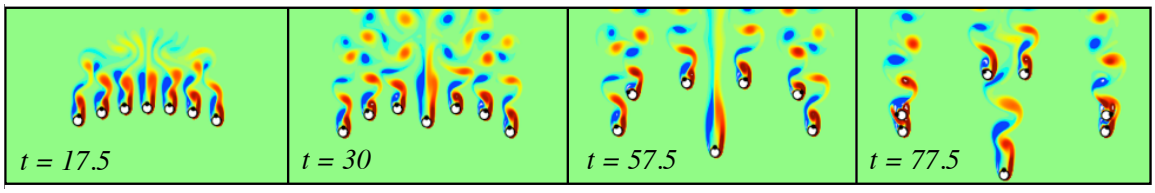

Figure 1.4: *Vorticity contours for $n = 7$ falling cylinders with initial spacing $d_0 = 2$. Clustering of the outermost pairs. Black dots on each cylinder are used to visually track their rotation.*

numerically. See Appendix A.

When $n \geq 5$, the two outermost cylinders tend to cluster. For example, when $n = 7$ (figures 1.3(a), 1.4), the two leftmost cylinders form a pair and tumble counter-clockwise. Similarly, the rightmost pair tumbles clockwise. The particles do not come into contact yet and their dynamics are reminiscent of the "drafting, kissing and tumbling" in fluidized beds of spheres [21]. It would be interesting to further investigate the long-term dynamics of these clusters, $t > 77.5$ on figures 1.4, using the lubrication equations during close contact, in large collections of particles.

We now allow the initial spacing d_0 to vary, while fixing the number of cylinders to $n = 5$. We summarize the effects of d_0 on the falling pattern in figure 1.3(b). We notice that the steady state configuration depends on the initial spacing. In particular, for the smallest d_0 that was simulated ($d_0 = 1.1$), the immediate neighbors of the middle cylinder approach the centerline, unlike in the other cases. In addition, the spread (or lateral drift) of the array is larger for smaller d_0 owing to the strong interaction force during the early stages of the fall. See details in section 1.3.3.

Together, these results suggest that arrays of falling cylinders, in an ini-

tial horizontal arrangement, can reach a steady state, the final configuration of which depends on the initial condition. This steady falling arrangement deviates significantly from the horizontal. This is in contrast with earlier work on the stability of an infinite array of settling cylinders at $Re \leq 100$, where infinite arrays of initially equally-spaced cylinders were found to be stable to displacements perpendicular and parallel to the array [54]. The difference may be due to the size of the array. But we suspect that it is most likely due to the Reynolds number which would affect the wake and the interaction between the particles.

1.3.2 Dynamics of the falling array

Given the rich dynamics exhibited by varying the number of cylinders and/or their initial spacing, we now focus on the dynamics of an array of three cylinders. In particular, we quantify the settling velocity, the flow history, the onset of vortex shedding, and the direction and rate of rotation of the cylinders. We will compare these dynamics for different initial spacings, as well as how the presence of neighboring cylinders affect the dynamics of the middle one, compared to an isolated settling cylinder. Additionally, we will contrast our results with those in Stokes flow.

Figure 1.5 shows the vorticity field of the fall of three cylinders with initial spacing $d_0 = 2$. As they settle, the array spreads out, the middle cylinder leads as it approaches a steady state, the left and right cylinders rotate in opposite directions and their wakes are symmetric about the centerline of the domain. The lateral expansion of the array is due to the strong initial repulsive force, as shown in figure 1.6, at $t \approx 7.5$.

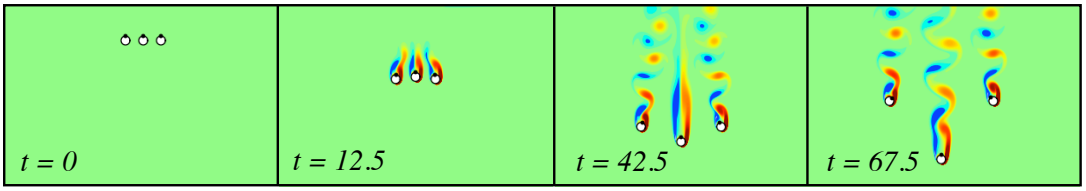

Figure 1.5: *Vorticity contours for $n = 3$ falling cylinders with initial spacing $d_0 = 2$. Mirror symmetry in the rotation of the cylinders. Counter-clockwise (positive) vorticity (red) and clockwise (negative) vorticity (blue). Black dots on each cylinder are used to visually track their rotation.*

To gain more insight into the dynamics of the middle cylinder, we first compare them to those of an isolated settling cylinder, under the same flow conditions. Then, we investigate the effect of the initial spacing d_0 on its kinematics and forces. Figure 1.7 shows the time series of the settling velocity, v, the drag coefficient, C_D, and the lateral force C_x, for the middle cylinder. The effective drag coefficient is larger than for an isolated one, due the presence of co-moving neighbors, and this leads to a decrease in the settling speed. The increase in drag is consistent with the previous computation of two cylinders moving in parallel at similar Reynolds numbers [57]. In contrast, in Stokes flow, the presence of neighboring particles causes a decrease in the drag force. This, in turn, results in an increase in the settling velocity [25]. The drag coefficient C_D for $d_0 = 1.1$ is smaller than for $d_0 = 1.5$ and $d_0 = 2$ initially, but greater than the other two after the onset of shedding. This is due to the cross-over in the fluid force. The net force on a particle is shown in figure 1.8, ($\ddot{y}$ *vs.* t). We can read the fluid force by shifting the curve up by a constant gravitational force. The fluid force for the case $d_0 = 1.1$ shows a cross-over similar to that seen in figure 1.7, although occurring at a different time because the drag coefficient is drag normalized by $\frac{1}{2}\rho_f U^2(t)L$. At steady state, the drag force does not differ much from the isolated cylinder case, and it differs mostly during the initial and transient stages where

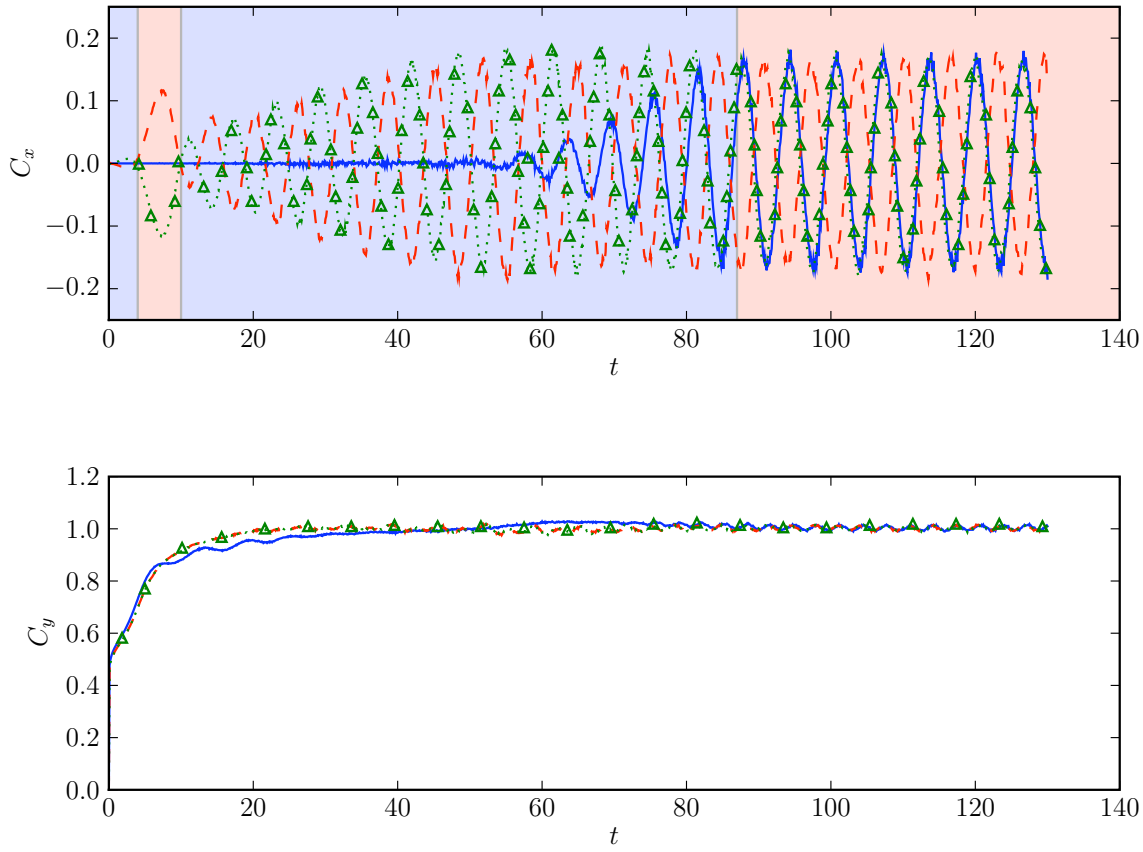

Figure 1.6: *Time series of the lateral (C_x, top) and vertical (C_y, bottom) fluid force on three settling cylinders: middle cylinder (blue, solid), right cylinder (red, dashed) and left cylinder (green, dotted, triangles). The shaded regions in the top figure correspond to the initial weak attraction, followed by a strong repulsive force, and a subsequent transition to steady state. The bottom figure shows that the cylinders attain a dynamic steady state at $t \sim 95$. $Re = 200$ and the initial spacing $d_0 = 2$.*

it is higher for the other three cases, resulting in a small settling velocity.

The settling velocity of an isolated cylinder reaches a maximum at $t \approx 57$. A closer look at figure 1.7 shows that this corresponds to the onset of vortex shedding. On the other hand, in the presence of its neighbors, the middle cylinder experiences wake instabilities much earlier during the fall, around $t \approx 18$ for

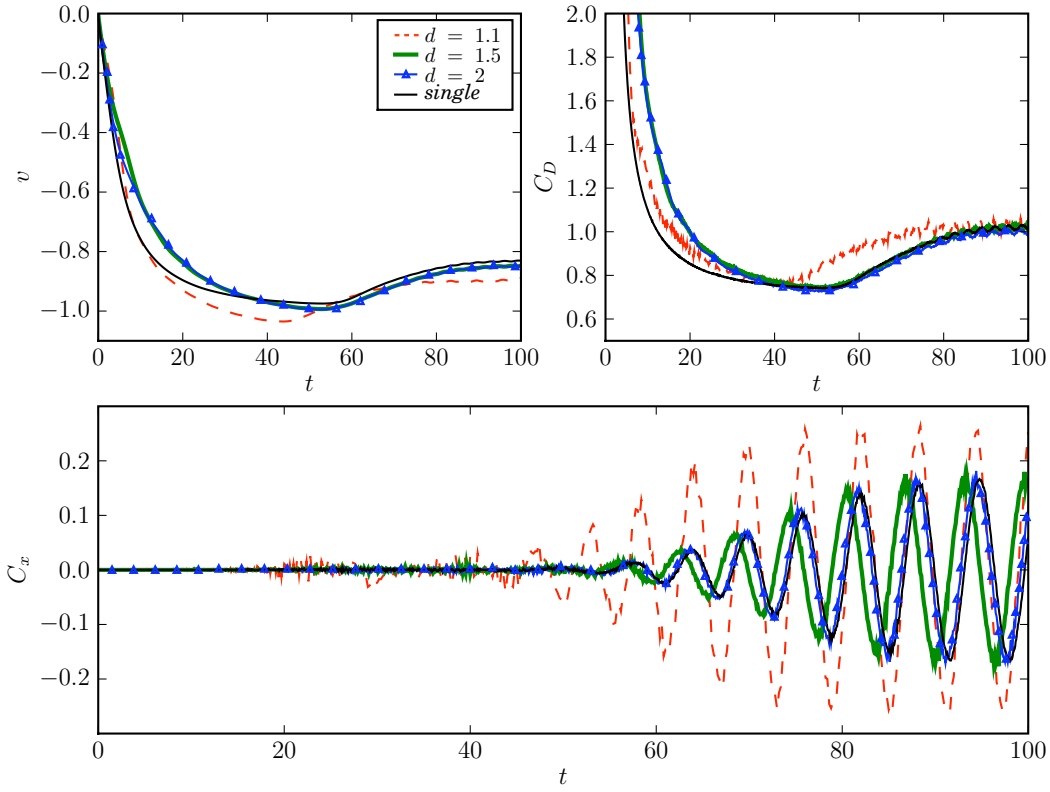

Figure 1.7: *Effect of the initial spacing on the drag coefficient, the settling velocity and the onset of vortex shedding for the middle cylinder. Comparison with an isolated falling cylinder.*

small d_0. As a comparison, for flow past a fixed cylinder at $Re = 200$, $t_{vs} \approx 20$, where t_{vs} is the time marking the onset of vortex shedding. The difference in t_{vs} underscores the difference between flow past a fixed cylinder and flow around a cylinder settling at steady state in a quiescent flow, due to the effect of the flow history. Given these results, we quantify the dynamics of the middle cylinder by varying $d_0 = 1.1$ to $d_0 = 3$ and choose to present three representative values $d_0 = 1.1, 1.5, 2$ and summarize the results in figure 1.8.

As mentioned above, the smaller d_0 is ($d_0 = 1.1$), the faster the middle cylinder settles, the sooner its wake symmetry is broken due to early vortex shedding and the sooner it reaches a steady state ($t_{vs} \approx 18, 50, 57$ for $d_0 = 1.1, 1.5, 2$,

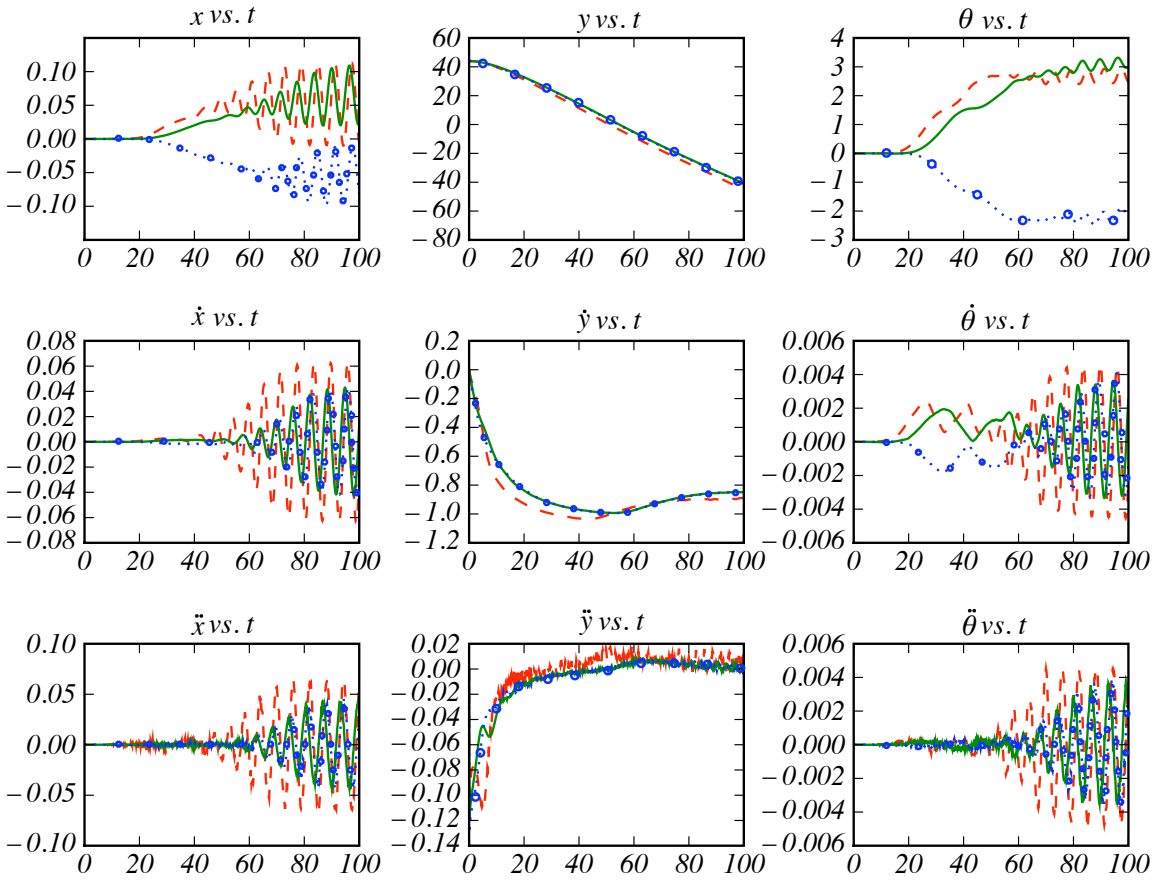

Figure 1.8: *Dynamics of the middle cylinder in a 3-cylinder settling array for different values of the initial spacing, d_0. $d_0 = 1.1$ (red, dashed), $d_0 = 1.5$ (green, solid) and $d_0 = 2$ (blue, dotted, circles). $Re = 200$.*

respectively). At steady state, and independently of the value of d_0, the middle cylinder sheds vortices which are in phase with those of either the left or the right cylinder. The non-dimensional shedding frequency in the horizontal direction is the same for all d_0 and is $S_{t,x} = \frac{fD}{V} \approx 0.157 - 0.158$. This can be seen in the time series of the lateral force, C_x, on figure 1.7, or the acceleration, $\ddot{x}$, and the velocity, $\dot{x}$, on figure 1.8.

Similar to fluttering plates or flow-induced vibrations over a fixed cylinder, the oscillation frequency of the middle cylinder along the flow is twice that across.

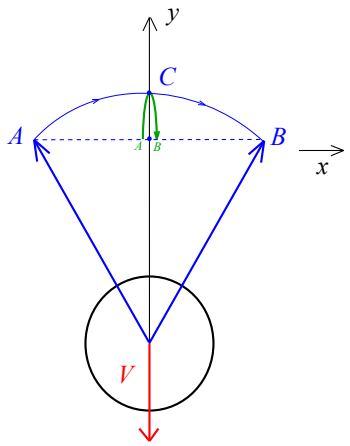

Figure 1.9: *Oscillation frequency of the force on the falling cylinder in the stream-wise (y) and cross-stream (x) directions. The oscillation frequencies satisfy* $f_y = 2f_x$.

This can be explained through figure 1.9. The fluid force vector on the cylinder oscillates between points A and B. When it goes from A to B, its y-component C_y goes a full cycle and comes back to the starting value, but its x-component C_x goes only a half cycle and changes the sign. Finally, figure 1.5 shows that the left and right cylinders rotate outwards, i.e clockwise for the left and counter-clockwise for the right. Consequently, their shed vortices are symmetric with respect to the centerline of the domain, i.e in anti-phase.

For arbitrary n, the outer pair rotates outwards. The inner cylinder, however, rotate inwards as shown on figure 1.10. The rate of rotation and lateral spread of the side cylinders increases when the array is initially closely packed, with an inter-particle gap below half a diameter.

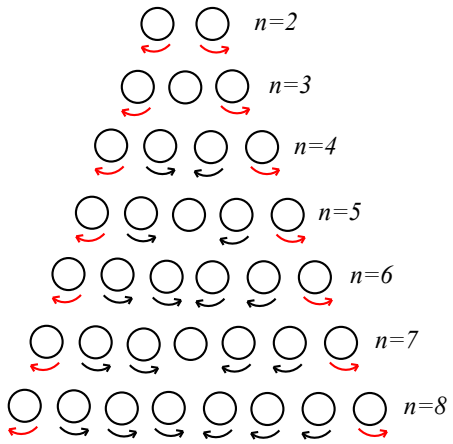

Figure 1.10: *Steady-state rotation pattern of the array of cylinders as a function of their number n.*

1.3.3 Pairwise interactions

To better understand the intricacies of hydrodynamic interactions between adjacent particles, we quantify pairwise interaction forces between two cylinders, dropped with zero initial velocity, and settling side by side. During the fall, the cylinders go through four phases, as shown on figure 1.6 for three cylinders. At the onset of their fall, they experience a short attractive force followed by a strong repulsive force along their line of centers. The fluid then dampens the subsequent lateral motion, before the cylinders settle to a dynamic steady state and shed vortices in their wakes. The repulsive force, which will be the focus in this section, was also observed in Stokes flow for falling cylinders, albeit not quantified [31]. It was also observed in flows past fixed side-by-side cylinders at intermediate Reynolds numbers [5, 37, 39, 44]. Similar to our case (figures 1.3(a) – 1.3(b)), the repulsive force was observed to cause a lateral spread of the collection of particles such as spherical clouds of particles [45].

In what follows, we vary the initial spacing between a pair of cylinders and

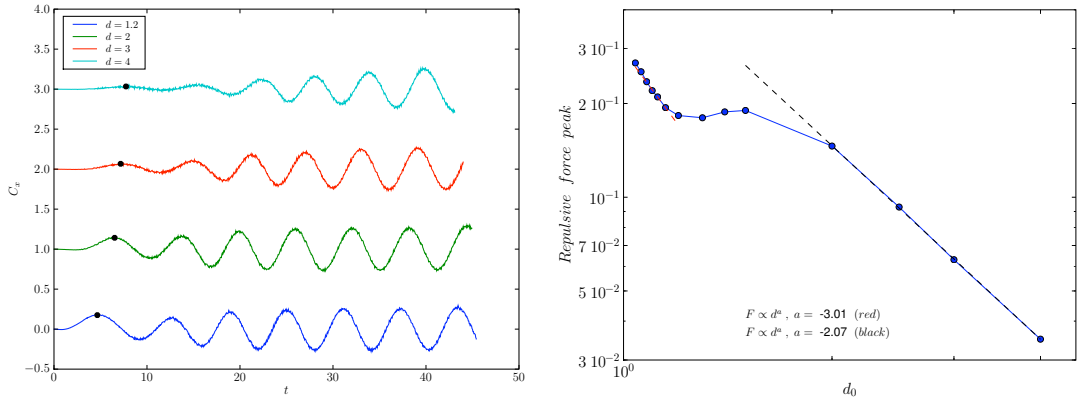

(a) (b)

Figure 1.11: *(a) Time history of the lateral fluid force coefficient, C_x, for the right cylinder, in a pair of settling cylinders, with different initial spacings. Except for the bottom curve, the y-axis does not reflect the magnitude of the force. The curves were shifted upward for ease of reading. (b) Force law model for the repulsive force as a function of the initial spacing, d_0. Re = 200.*

record the magnitude of the peak of the repulsive force. When the initial spacing was very small ($d_0 < 1.1$), the resolution was doubled ($\Delta x = \Delta y = 1/80$), in order for the interpolation scheme to hold. Figure 1.11(a) shows the time history of the lateral fluid force coefficient, C_x, for different initial spacings, for the right cylinder.

The results show that the closer the cylinders are initially, the earlier the onset of the repulsive force and the higher its magnitude. To find what force law model the repulsive force follows, we use a linear fit of the magnitude of the repulsive force, in a plot a log-log graph, as a function of the initial spacing d_0, where $d_0 \in [1.08, 4]$. Namely, we are looking for the value of the power $\alpha > 0$ such that the close-range interaction force is of the form $F \propto d_0^{-\alpha}$. Figure 1.11(b)

shows that,

$$F_{peak} \propto d_0^{-3} \quad \text{for} \quad d_0 < 1.2$$
$$F_{peak} \propto d_0^{-2} \quad \text{for} \quad d_0 \geq 2$$

It is interesting to compare this result with what happens in three dimensions for low Reynolds number flows. In Stokes regime, the repulsive force is similar to Stokes drag on sphere, with a correction term proportional to $1/d$. Indeed, for two spheres of common radius a, separated by a distance d, and drifting side-by-side at a velocity U, the repulsive force is

$$F_{LC} \approx 6\pi\mu a U \left(1 - \frac{3a}{4d}\right) \tag{1.10}$$

We remind the reader that the force law we found above does not apply at all times, but only for the peak of the repulsive force, for a given initial spacing. A more accurate expression will be derived in Chapter 2 for close range interactions, using the lubrication theory.

1.4 Conclusions and future work

In this paper, we studied the falling pattern and dynamics of a horizontal array of settling cylinders at Reynolds number 200, using direct numerical simulation. Given the unsteadiness of the flow, we asked whether such a system exhibits a steady state and if so, how it depends on the initial conditions. We investigated the dependence of the falling dynamics on the number of cylinders, n, and on the initial spacing, d_0. We found that the cylinders reach a steady state, independent of the value of n or d_0. The steady state configuration, however, depends both on n and d_0. When n is odd, the middle cylinder is always leading, whereas when n is even, the array adopts a concave-down shape. We then fixed $n = 3$ and studied the effect of the initial spacing on the dynamics of the middle cylinder. We compared them to those of an isolated settling cylinder as well as with results in Stokes flow. We found that the middle cylinder experiences a higher drag force due to the presence of its left and right neighbors, resulting in a slower settling velocity. This result is opposite of that at Stokes regime where a sphere in the presence of its neighbors settles faster than an isolated one. Our results also showed that the closer the initial spacing is, the sooner wake asymmetries arise for the middle cylinder and the sooner it settles to a steady state. At steady state, for all values of d_0, there is a left-right symmetry in the falling configuration, the wake pattern and the direction of rotation of the left and right cylinders, with respect to the centerline of the domain.

To solve for these dynamics, we developed a robust implementation of the immersed interface method. The novel aspect of this implementation is an efficient handling of the coupling between the rigid body and the fluid, using an iterative method. The method is stable at high Reynolds numbers, at standard

CFL (*Courant-Friedrichs-Lewy*) conditions. The method is almost second order accurate, including along the interface. The code was validated against experiments on falling plates in a fluid. This method provides an efficient tool for us to further investigate collective behavior and self-organization of particles subject to hydrodynamic interactions.

CHAPTER 2

ON THE HANDLING OF PARTICLE COLLISIONS IN A VISCOUS FLUID USING THE LUBRICATION EQUATIONS IN THE IMMERSED INTERFACE METHOD

This chapter is a work in progress, and we are currently processing the results. In what follows, I will summarize the current results. Most of the material can be found in a our manuscript in preparation for the Journal of Fluid Mechanics [19].

2.1 Introduction

The interaction of particles in fluids are key to understanding collective behavior of particles in particle-laden flows such as sedimentation [24], particle suspensions as well as biological phenomena. For example, Ireland & Collins [29] and Warhaft [58] reported that a better understanding of inertial particle clustering (e.g. raindrops) is key to studying natural processes, where particles are subject to entrainment, such as in cloud growth and evolution. In the biological field, the mechanisms behind mechanical contact and/or hydrodynamic interactions between swimming micro-organisms, are yet to be determined. However, it was suggested that when swarming, micro-organisms such as plankton or algal cells can enhance the biogenic mixing in oceans [38, 42]. These large scale collective dynamics thus help in the diffusion and transport of nutrients in the otherwise viscosity-dominant scale of an isolated micro-organism.

In the high particle-density limit, collisions become an important feature of the underlying physics. Collisions, by way of close range particle interactions,

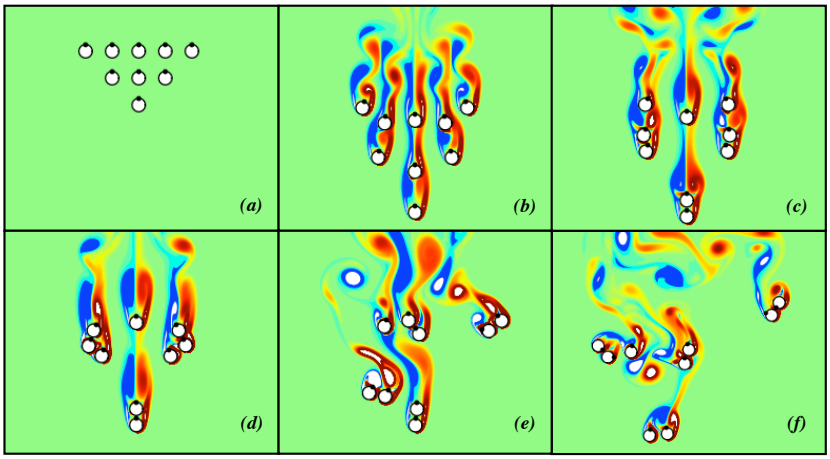

Figure 2.1: *Vorticity field of $n = 9$ particles settling under gravity in a fluid at $Re = 200$. The solid-to-fluid density ratio is $\gamma = 2.56$. Black dots are used to track the rotation of the particles.*

introduce a small length scale, in an otherwise inertia-dominated flow. To accurately solve for these dynamics, we need a method that can perform high Reynolds number simulations and also be able to handle the thin layer of fluid in the interstitial gap between particles. However, numerical methods generally fall into two distinct categories. Some methods simulate dynamics only in the Stokesian regime for particle-wall interactions [9, 28] or particle suspensions [6]. At the other end of the spectrum are methods that focus exclusively on the high Reynolds number regime [29, 58]. In this paper, we propose a numerical approach, based on the immersed interface method, where the lubrication equations are directly incorporated into the numerical scheme, hence enabling the simulation of both inertia-dominated and viscosity-dominated dynamics, as well as the intermediate ranges of Reynolds numbers.

We motivate our paper by the qualitative results displayed in figure 2.1. The figure shows the dynamics of a settling lattice of particles in a fluid, under gravity. The particles are two-dimensional cross-sections of infinitely long cylinders

and the Reynolds number is 200. As the lattice settles, interesting dynamics unfold. The lagging particles draft behind the leading ones, until they catch up and come into close contact (figure 2.1 (b,c)). The hydrodynamic attraction here is due to the low pressure wake and is different from the low Reynolds number regime $Re = O(10^{-1} - 10)$, where the attraction between spheres falling along their lines of centers is due to the induced velocity field created by each particle, treated as a point source. The doublets and triplets form an elongated body that falls edge-on. Owing to a turning couple, this configuration is unstable in a Newtonian fluid (figure 2.1 (d)), and the elongated body disintegrates into pairs that tumble (figure 2.1 (e,f)). This mechanism was called *Drafting-Kissing-Tumbling* (DKT) by Joseph et *al* [34] and summarizes a fundamental dynamical phenomenon taking place in suspensions of particles, when particle inertia matters. However, these dynamics were also observed experimentally by Happel & Pfeffer [26] in the Oseen regime ($Re = 0.3 - 0.7$), albeit owing to different mechanisms. They used Stimson's calculations [55], which are based on Stokes drag model, modified by a correction factor to take into account the interaction effect. They showed that the bottom particle is slowed down due to "inertial" forces, whereas the velocity of the top particle is not affected and falls according to the Smoluchowski theory (see [26]). The top particle then rolls over the bottom one until they become parallel. The nature of the interaction force is then a repelling one, and the pair separates. The results in figure 2.1 were obtained using a classical two-dimensional dry collision model, when particles are in close contact. The goal of this paper is to model such collisions by solving *directly* for the flow using the lubrication equations in the interstitial fluid.

We now present an overview of the literature on particle interactions and collisions, from the experimental as well as the theoretical and numerical per-

spective. Several theoretical models using the lubrication equations have been developed in order to solve for the particle dynamics during close contact. Cooley [9] and O'Neill & Stewartson [48] studied the slow motion of a sphere near a wall or another sphere. They decomposed the flow into an inner region, where lubrication equations were used, and an outer region where the flow is weakly sheared. They used matched asymptotic expansions between the two regions and found that the fluid force acting opposite to the motion of the sphere is singular and inversely proportional to the minimum gap clearance. When transverse motion is considered [28], the forces and couples on the sphere have a logarithmic dependence on the minimum gap clearance.

Likewise, in the past few decades, several experiments were carried out and validated against new theoretical models. Joseph et *al* [36] conducted experimental measurements on the coefficient of restitution during approach and rebound of particles colliding with a wall. They showed that the nature of the collision depends on the Stokes number, defined as a measure of particle inertia to viscous forces. The higher the Stokes number, the higher the coefficient of restitution, and the greater the distance at which the particle starts to decelerate due to the built-up of the pressure in the gap. Additionally, Joseph & Hunt [35] found that lubrication effects caused a lower friction coefficient for immersed oblique collisions of smooth particles. To account for this decrease, they proposed an analytical model based on the lubrication theory for the fluid viscosity in the gap. Their model showed that the dependence of the fluid viscosity on the pressure (and temperature) was key to explaining the reduction in the friction coefficient and the rotational torque impulse on particles upon collision. Yang & Hunt [63] conducted experiments and developed a theoretical model based on the hydrodynamic impulse theory, and showed that the dynamics of normal

and oblique collisions are decoupled. Similar to [35], their model showed that the coefficient of friction for the oblique collisions is affected by the interstitial fluid.

When the interstitial gap becomes narrow, the requirement of an infinitesimal grid spacing makes numerical methods computationally costly. Following Joseph et *al*'s experiments on fluidized beds of particles [34], Feng et *al* [20] conducted a finite-element-based direct numerical simulation of two settling particles at various Reynolds numbers. At $Re \sim 70$, they found that the particles never come into contact owing to the increase in pressure in the lubrication layer. However, their meshing scheme, in addition to being costly, breaks down when particle inertia is large and particles tend to collide. This issue was encountered in several numerical methods and has been addressed using *ad hoc* approaches. Sing et *al* [54] developed a modified Disributed Lagrange Multiplier (DLM) method that allowed close contact of particles and the full resolution of the hydrodynamic forces. However, a repulsive force was added when the particles overlapped. Ardekani et *al* [3] and Ardekani & Rangel [4] also developed a DLM-based, finite-volume method where a uniformly distributed, impulsive contact force is added to each particle upon collision and vanishes when the particles separate. These methods could, however, lead to unrealistic physics such as the rebound of particles where rebound may not take place in reality.

Nguyen & Ladd [46] used a lattice-Boltzmann based method to simulate particle suspensions at low but finite Reynolds numbers. Unlike other methods which resort to the addition of a repulsive force, their method incorporates force and torque components from lubrication theory, thus adding a correction

to their numerical scheme for particles in close contact. Their method handles well the problem of conservation of mass when two particles are in close contact, as well as the stiffness of the differential equations for the particle velocities, due to high lubrication forces. However, their method does not take into account the effects on the outer flow of the force density on the particles in the lubrication region.

Sangani & Mo [53] developed a method to include close-range lubrication forces into multi-particle numerical simulations. Unlike previous multipole expansions-based methods (not cited here), where accurate computations required a high number of multipoles in the small gap region, their method has the advantage of directly incorporating the singular forces from lubrication in the gap and only retaining few multipoles at the center of the particles. Albeit limited to Stokes flow calculations, their method, valid for both spheres and cylinders, has the advantage of solving for the full lubrication problem. In two dimensions, for instance, the (outer) fluid flowing through narrow gaps between cylinders is accounted for in the lubrication calculations; and the lubrication force density and the size of the area over which it acts was taken into account in both their two- and three- dimensional calculations.

In the present chapter, we give an overview of our numerical method and how lubrication equations are incorporated into the numerical scheme. We then present results of three fundamental cases, which serve as a validation of our code, and cover the basic dynamics of closely interacting particles. The first case is that of a cylinder falling vertically toward a fixed wall. This case captures the dynamics of normal collisions. The two remaining cases, fixed cylinder above a translating wall and rotating cylinder above a fixed wall, capture the dynamics

of oblique collisions, where the relative tangential velocities and shear forces are predominant. Unlike most numerical methods, our current implementation is capable of treating both the inertia-dominant regime (e.g during settling) as well as the Stokes limit (e.g during close approach). Additionally, similar to [53], our method solves for the full lubrication problem in that the effect of the outer flow outside the lubrication region is taken into account in the lubrication calculation, and this latter, in turn, affects the bulk flow.

2.2 Method

2.2.1 Statement of the problem

The immersed interface method is a numerical method that enables the simulation of the dynamics of objects immersed in a fluid. The present method is built on previous work [18, 59]. In [18], the method was developed to simulate freely moving objects by simultaneously solving for the object dynamics and Navier Stokes equations for the fluid. The dynamics for the fluid are governed by Navier Stokes equations, subject to boundary conditions on the surface of the objects. The dynamics of the object are governed by Newton's equations. The presence of the object in the fluid is accounted for by a singular force density distribution along the object interface. This singular force is related to and responsible for jump conditions on the velocity and pressure fields.

The singular force components at any point on the interface, are computed using a three-point stencil-based interpolation from the velocity or vorticity field, at adjacent nodes in the fluid domain (see figure 4 in [59]). However, when

the gap between two objects or an object and a wall falls below three grid cells, the interpolation scheme fails. To circumvent this numerical hurdle, we use the lubrication theory equations to solve for the velocity and pressure gradient in the lubrication region, defined as the portion of the gap where the distance to the adjacent object or to the wall is less than four grid cells. We chose four instead of three grid cells to avoid the limit case where the third node is right on the wall or the adjacent object. The analytical expressions of the velocity and pressure gradient are then used to find the analytical expressions of f_τ and $(\partial f_n/\partial\alpha)$, thus bypassing the interpolation. Outside the lubrication region, the interpolation scheme is still in use.

The fluid is assumed to be incompressible and Newtonian, with constant density, ρ_f and viscosity μ. The particle of interest is a two-dimensional cross-section of an infinitely long cylinder. The surface of the cylinder is assumed to be smooth and the gap between the cylinder and the wall is in the y-direction.

2.2.2 Lubrication theory equations and assumptions

The two-dimensional incompressible Navier-Stokes equations are

$$\frac{\partial u}{\partial x} + \frac{\partial v}{\partial y} = 0 \tag{2.1a}$$

$$\rho_f \left(\frac{\partial \vec{u}}{\partial t} + \vec{u} \cdot \nabla \vec{u} \right) = -\nabla p + \mu \nabla^2 \vec{u} \tag{2.1b}$$

where $\vec{u} = (u, v)$ is the fluid velocity, p is the pressure, ρ_f and μ are the fluid density and viscosity, respectively. In non-dimensional form, equations 2.1a, 2.1b become

$$\frac{\partial u}{\partial x} + \frac{\partial v}{\partial y} = 0 \tag{2.2a}$$

$$\frac{\partial \vec{u}}{\partial t} + \vec{u} \cdot \nabla \vec{u} = -\nabla p + \frac{1}{Re} \nabla^2 \vec{u} \tag{2.2b}$$

where the Reynolds number, $Re \triangleq \rho_f L V_s / \mu$, is based on appropriate length, L, and velocity, V_s, scales. For the remainder of the paper, $L = D$ is the diameter of the cylinder and V_s will be defined on a case by case basis (terminal settling velocity, steady rotation of the cylinder, translational velocity of the wall). In general, the terms in equation 2.2b are *a priori* $O(1)$. However, when the gap height (in the y-direction) becomes very small, the orders of magnitude of these terms change. To further simplify the Navier-Stokes equations in the lubrication theory limit, we perform an order of magnitude analysis to discard negligible terms in equation 2.2b. Let U and V be the velocity scales and L and h be the length scales for velocity variations in the x and y- directions, respectively. From the continuity equation 2.2a, we have

$$V \sim \frac{Uh}{L}$$

When $h/L \ll 1$, a condition met in our cases, and $V/U \ll 1$, the pressure variations in the y direction can be neglected, i.e

$$\frac{\partial p}{\partial y} = 0 \quad \Rightarrow \quad p = p(x)$$

Thus, p is function of x only. In the x-component of equation 2.1b, we have

$$\left\{ \rho_f \frac{\partial u}{\partial t} \, , \, \rho_f \vec{u} \cdot \nabla \vec{u} \, , \, \frac{dp}{dx} \right\} \sim \frac{\rho_f U^2}{L}$$

$$\mu \frac{\partial^2 u}{\partial x^2} \sim \frac{\mu U}{L^2} \quad , \quad \mu \frac{\partial^2 u}{\partial y^2} \sim \frac{\mu U}{h^2}$$

When $h \ll L$, we have $\mu |\partial^2 u / \partial x^2| \ll \mu |\partial^2 u / \partial y^2|$, and equation 2.1b in the x-direction, divided by $\rho_f U^2 / L$, becomes

$$\underbrace{\frac{\partial u}{\partial t} + u \frac{\partial u}{\partial x} + v \frac{\partial u}{\partial y}}_{O(1)} = -\frac{dp}{dx} + \frac{1}{Re} \underbrace{\frac{\partial^2 u}{\partial y^2}}_{O((h/L)^2)} \tag{2.3}$$

This gives an order of magnitude of the pressure gradient,

$$\frac{dp}{dx} = O\left(\frac{1}{Re\, h^2/L^2}\right)$$

which is kept in equation 2.3 to avoid a trivial solution. Contrary to equation 2.2b, not all terms are of the same order of magnitude at the limit of a small gap. Consequently, equation 2.3 becomes

$$0 = -\frac{dp}{dx} + \frac{1}{Re}\frac{\partial^2 u}{\partial y^2} \tag{2.4}$$

known as *Reynolds equation* which is a modified Navier-Stokes equation at the lubrication theory limit. Equation 2.4 is valid when $h/L \ll 1$ and $Re\, h^2/L^2 \ll 1$. These are the two conditions for the lubrication theory to hold. At this limit, the object motion can be considered as quasi-steady. In summary, we are solving the following problem for an incompressible, newtonian fluid

$$\frac{\partial u}{\partial x} + \frac{\partial v}{\partial y} = 0 \tag{2.5a}$$

$$\frac{\partial^2 u}{\partial y^2} = Re\frac{dp}{dx} \tag{2.5b}$$

2.2.3 Solution to the Reynolds equations in the lubrication limit

We consider the general case of two objects in close contact. In what follows, all quantities are non-dimensional, unless otherwise stated. To simplify the calculations, we assume the motion to be in the y-direction (vertical). The configuration is shown in figure 2.2. In a more general case, one can define a local coordinate system, co-moving with the objects, with axes along and perpendicular to the line of centers. See appendix B. We first solve equation 2.5b for the

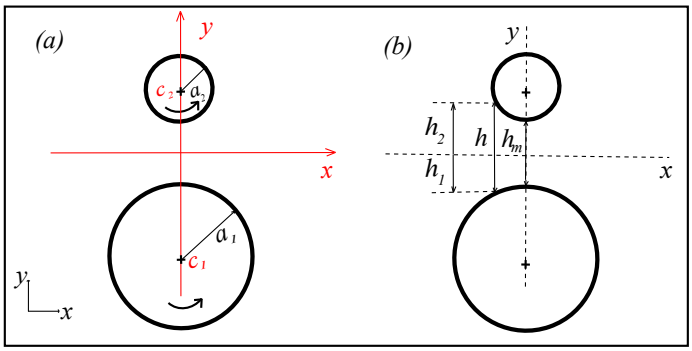

Figure 2.2: *Sketch of two cylinders in close contact. (a) The radii of the cylinders are a_1 and a_2. (b) At abscissa x, the separation is $h = h_2 - h_1$. h_m is the minimum separation at $x = 0$.*

velocity u and apply the boundary conditions

$$u = u_i \quad at \quad y = h_i,\ i = 1, 2$$

u_i is the x-velocity of a point P_i on object "i", located at abscissa x. We obtain

$$u = u_1 + \frac{u_2 - u_1}{h}(y - h_1) + \frac{Re}{2}\frac{dp}{dx}((y - h_1)^2 - (y - h_1)h) \tag{2.6}$$

where $h = h_2 - h_1 = h_m(t) + a_1 + a_2 - \sqrt{a_1^2 - x^2} - \sqrt{a_2^2 - x^2}$. To get the pressure gradient, we use the volume flux along the x-direction

$$\begin{aligned} Q &= \int_{h_1}^{h_2} u\, dy \\ &= u_1 h + \frac{u_2 - u_1}{2}h - \frac{Re\, h^3}{12}\frac{dp}{dx} \\ &= \overline{u}h - \frac{Re\, h^3}{12}\frac{dp}{dx} \end{aligned} \tag{2.7}$$

where $\overline{u} = (u_1 + u_2)/2$. We then integrate the continuity equation across the gap

$$\int_{h_1}^{h_2} \frac{\partial u}{\partial x}\, dy = -\int_{h_1}^{h_2} \frac{\partial v}{\partial y}\, dy = -\frac{\partial h}{\partial t} \tag{2.8}$$

We re-write equation 2.8 to involve the volume flux Q

$$\begin{aligned} \int_{h_1}^{h_2} \frac{\partial u}{\partial x}\, dy &= \frac{\partial}{\partial x}\left(\int_{h_1}^{h_2} u\, dy\right) - u_2\frac{dh_2}{dx} + u_1\frac{dh_1}{dx} \\ &= \frac{\partial Q}{\partial x} - u_2\frac{dh_2}{dx} + u_1\frac{dh_1}{dx} \end{aligned} \tag{2.9}$$

We combine equations 2.7-2.9, and obtain the equation for pressure

$$\frac{\partial h}{\partial t} + \frac{\partial}{\partial x}(\overline{u}h) + u_1\frac{dh_1}{dx} - u_2\frac{dh_2}{dx} = \frac{Re}{12}\frac{\partial}{\partial x}\left(h^3\frac{dp}{dx}\right) \tag{2.10}$$

We can solve analytically for the pressure gradient by integrating equation 2.10 once with respect to x

$$\frac{dp}{dx} = \frac{12}{Re}\left\{\frac{\overline{u}}{h^2} + \frac{\dot{h}x}{h^3} - \frac{(\dot{\theta}_2 - \dot{\theta}_1)x^2}{2h^3} + \frac{\dot{x}_{c_1}\sqrt{a_1^2 - x^2}}{h^3} + \frac{\dot{x}_{c_2}\sqrt{a_2^2 - x^2}}{h^3} + \frac{C(t)}{h^3}\right\} \tag{2.11}$$

where $C(t)$ is a constant of integration which will be determined by matching either the velocity field or the volume flux at a given location x along the gap. The reader should note that our approach in equations 2.6 - 2.11 is for any arbitrary relative motion between two approaching particles and can be extended to any collection of particles where lubrication regions exist. The volume flux, Q, accounts for all terms, except the first, in equation 2.11. And as such, determining the unknown $C(t)$ relies on determining Q. Three examples will be presented in this chapter to illustrate how Q or, equivalently $C(t)$, is determined. Finally, unlike [46], the singular force in the lubrication region enters into the computation and the update of the bulk flow, i.e the flow external to the lubrication region.

In summary, equations 2.6 and 2.11 give the solutions (u,p) to Reynolds equations 2.5a, 2.5b, in the most general case; that is, for any relative motion between approaching particles. These equations will be further simplified for the cases presented later in this paper. For the case where the line of centers of the two particles in not parallel to the vertical axis of the lab frame, the solutions are projected onto the local co-moving frame as explained in appendix B.

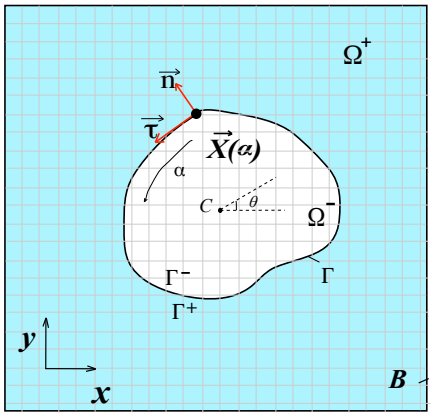

Figure 2.3: *Computational domain of an object immersed in a fluid. Courtesy [18]*

2.3 Implementation in the immersed interface method

To solve for the dynamics of a freely moving object immersed in a viscous fluid, we use our previous formulation of the immersed interface method in [18]. The two-dimensional Navier-Stokes momentum equation, in non-dimensional form, is

$$\frac{\partial \vec{v}}{\partial t} + \vec{v} \cdot \nabla \vec{v} = -\nabla p + \frac{1}{Re} \nabla^2 \vec{v} + \int_\Gamma \vec{f}(\alpha, t) \delta(\vec{x} - \vec{X}(\alpha, t))\, d\alpha \tag{2.12}$$

where $\vec{v}$ and p are the fluid velocity and pressure, respectively, $Re = \rho_f L V_s / \mu$ is the Reynolds number based on characteristic length, L, and velocity, V_s, scales, and on the fluid density, ρ_f, and viscosity, μ. The singular force density, $\vec{f}$, enforces the boundary condition on the interface Γ of the object (see figure 2.3). The tangential and normal components of the singular force density $\vec{f}$ are given by

$$f_\tau = -\frac{1}{Re}[\omega] = -\frac{1}{Re}\left[\vec{\tau} \cdot \frac{\partial \vec{v}}{\partial n}\right] \tag{2.13a}$$

$$f_n = \int \left(\frac{1}{Re}\left[\frac{\partial \omega}{\partial n}\right] + [\vec{f_b}] \cdot \vec{\tau}\right) J\, d\alpha \tag{2.13b}$$

where $\omega = (\partial v/\partial x) - (\partial u/\partial y)$ is the fluid vorticity in two dimensions, $\vec{\tau} = (\partial \vec{X}/J\partial\alpha)$ is the unit tangent vector to the interface Γ, which is parameterized by α, and $J = \|\partial \vec{X}/\partial\alpha\|_2$. The brackets, $[\bullet] = (\bullet)^+ - (\bullet)^-$, denote a jump across the interface. $\vec{X} = (X, Y)$ are the cartesian coordinates of a lagrangian point on the boundary Γ and $\vec{x_c} = (x_c, y_c)$ are those of the center of mass of the object. See figure 2.3. $\vec{f_b} = \vec{\Omega} \times (\vec{X} - \vec{x_c})$ is a body force which enforces rigid body motion of the fluid inside the object, where $\vec{\Omega}$ is the angular rotation of the object.

The equations of motion for the immersed object are:

$$m_s \dot{\vec{v}}_c = \vec{F}_{ext} + \vec{F}_f \tag{2.14a}$$

$$I^* \ddot{\theta} = T_f \tag{2.14b}$$

where m_s is the mass of the object, $\vec{v}_c$ is its velocity in the lab frame, at its center of mass, I^* its moment of inertia with respect to its center of mass, $\vec{F}_{ext}$ is the external non-fluid force on the object (e.g. buoyancy corrected weight), $\vec{F}_f$ is the fluid force on the object, and T_f is the fluid torque on the object with respect to its center of mass. The fluid force and torque acting on the object can be expressed through the integrals of the singular force

$$\vec{F}_f = -\int_\Gamma (f_\tau \vec{\tau} + p^+ \vec{n})\ J \mathrm{d}\alpha \tag{2.15a}$$

$$\vec{T}_f = -\int_\Gamma (\vec{X} - \vec{x_c}) \times (f_\tau \vec{\tau} + p^+ \vec{n})\ J \mathrm{d}\alpha \tag{2.15b}$$

where p^+ is the pressure outside the object. Equations 2.12, 2.14 and 2.15 underscore the coupling between the dynamics of the fluid and the object.

In the immersed interface method, f_τ and $(\partial f_n/\partial\alpha)$ are computed using an interpolation from the velocity field, via a three-point stencil, in a one-sided finite difference scheme (see figure 4 in [59]). However, when the gap between two objects or an object and a wall falls below three grid cells, the interpolation fails.

In what follows, we will explain how we address this problem using the lubrication equations derived in section 2.2. We will use the term "lubrication phase" to denote the phase of the simulation during which the lubrication equations are used.

2.3.1 Numerical parameters

As explained in section 2.2.3, the Reynolds equations 2.5a and 2.5b in the lubrication limit are valid when

$$h_m \ll 1 \quad and \quad Re.h_m^2 \ll 1 \tag{2.16}$$

where h_m is made non-dimensional through a division by $L = D$, the diameter of the cylinder. For a given resolution, the second condition in equation 2.16 puts a constraint on the choice of the Reynolds number, which has to satisfy the inequality at the maximum h_m, i.e $h_m = 4\Delta n = 4\Delta y$, where $\Delta n = \sqrt{\Delta x^2 + \Delta y^2}$ is the length of a grid cell along the normal to the interface. See figure 2.4. To test our method, we choose the Reynolds number to be $Re = 10$, and a grid cell size $\Delta x = \Delta y = 1/80$ for a domain size 640×2560. The time step satisfies the *Courant-Friedrich-Lewy* (known as CFL) condition $\Delta t < Re\,.\,CFL/(1/(\Delta x)^2 + 1/(\Delta y)^2)$. The solid-to-fluid density ratio, $\gamma = 1.5$, is fixed for the entire study. When the lubrication equations are used, the time step is reduced proportionally to the minimum gap height, h_m, in order to capture the rapidly changing dynamics of the object and the flow. At the onset of the lubrication phase, the middle point is the only point in the lubrication region. In this case, the normal distance to the wall is simply the gap height at the middle h_m. With our choice of the Reynolds number and the grid resolution, we have $h = h_m = 4\Delta n = 4\Delta y = 0.05$ and

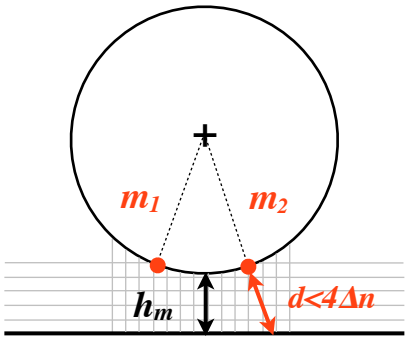

Figure 2.4: *Sketch of a cylinder approaching a wall at the onset of the lubrication phase. m_1 and m_2 are the lagrangian points demarkating the lubrication region, h_m is the minimum gap height and d is the normal distance from a lagrangian point to the wall*

$Re.h_m^2 = 0.025$ at the onset of the lubrication phase, and the conditions in equation 2.16 are satisfied. Obviously, as the object continues to fall, these quantities get smaller and the conditions in equation 2.16 remain valid. Additionally, the flow in the lubrication region along the gap, i.e along a distance of $\sqrt{a\,h_m}$, is also well resolved, since we have at least ten grid points throughout the simulation.

2.3.2 Singular forces in the lubrication limit

The main issue with the immersed interface method is that the singular force components, f_τ and $(\partial f_n/\partial\alpha)$, are computed using an interpolation from the velocity field, using a three-point stencil, in a one-sided finite difference scheme. We modify equations 2.13a - 2.13b and use their analytic expressions in the lubrication region. From an academic standpoint, we will present the case of a cylinder falling vertically toward a fixed wall. The procedure is similar for other cases.

The tangential singular force

From equation 2.13a, we have

$$f_\tau = -\frac{1}{Re}(\omega^+ - \omega^-)\,, \tag{2.17}$$

where the vorticity outside and inside the cylinder is $\omega^+ = (\partial v/\partial x)^+ - (\partial u/\partial y)^+$ and $\omega^- = 2\dot{\theta}$, $\dot{\theta}$ being the angular velocity of the cylinder. For ω^+, we have $|\partial v/\partial x| \sim Uh/L^2$ and $|\partial u/\partial y| \sim U/h$, with $h/L \ll 1$. Thus

$$f_\tau \approx \frac{1}{Re}\left(\frac{\partial u}{\partial y}\right)^+ \tag{2.18}$$

where u is given by equation 2.6. Subscripts "1" and "2" in equation 2.6 refer to the wall and the cylinder, respectively. All terms involving subscript "1" disappear and the radius a_1 is infinite. Likewise, because the cylinder does not rotate nor moves sideways, $u_2 = 0$. Thus, equations 2.6, 2.10 become

$$u = \frac{Re}{2}\frac{dp}{dx}\,y\,(y-h)\,, \tag{2.19a}$$

$$\frac{dp}{dx} = \frac{12}{Re}\frac{\dot{h}x}{h^3}\,, \tag{2.19b}$$

where the height h, at abscissa x, is shown on figure 2.5. The constant of integration, after integrating equation 2.10 once, is zero, since $dp/dx = 0$ at $x = 0$, i.e the pressure reaches a maximum at the center. It is interesting to note that the velocity profile is essentially that of a Poiseuille flow driven by a non-constant pressure gradient. Finally, combining equations 2.18, 2.19a, 2.19b, the tangential singular force is

$$f_\tau = \frac{h}{2}\frac{dp}{dx} = \frac{6\dot{h}x}{Re\,h^2}\,. \tag{2.20}$$

See equation (19) in [51].

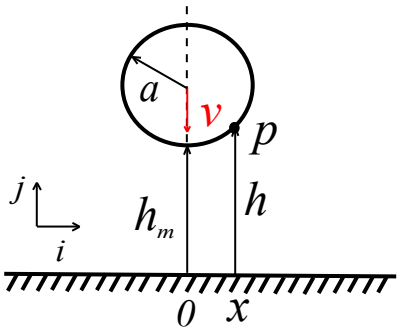

Figure 2.5: *Sketch of a cylinder of radius a, falling vertically toward a fixed wall. v is the settling velocity. h is the height at position x, at point P, and h_m is the minimum gap height, i.e at $x = 0$.*

The normal singular force

We proceed in a similar way with the normal component of the singular force. From equation 2.13b, we have

$$\frac{\partial f_n}{\partial \alpha} = J\left(\frac{1}{Re}\left[\frac{\partial \omega}{\partial n}\right] + [\vec{f_b}]\cdot\vec{\tau}\right) , \tag{2.21}$$

where $[\partial\omega/\partial n] = (\partial\omega/\partial n)^+$ since ω^- is uniform. The body force $\vec{f_b}$ is zero, since the cylinder does not rotate in this case. From the previous analysis with f_τ, $\omega^+ \approx -(\partial u/\partial y)^+$ and the normal derivative is

$$\frac{\partial \omega}{\partial n} = \frac{\partial \omega}{\partial x}n_x + \frac{\partial \omega}{\partial y}n_y .$$

Using the fact that $|\partial/\partial x| \ll |\partial/\partial y|$, we have

$$\left[\frac{\partial \omega}{\partial n}\right] \approx -\frac{\partial^2 u}{\partial y^2}n_y = -Re\frac{dp}{dx}n_y , \tag{2.22}$$

where $n_y = -\sqrt{1-(x/a)^2}$ is the y-component of the outward unit normal vector to the interface, at abscissa x, and a is the radius of the cylinder (we drop all subscripts "2" for ease of reading). Re-arranging the three equations above and using the expression of the pressure gradient in equation 2.19b, we finally obtain

$$\frac{\partial f_n}{\partial \alpha} = -J\sqrt{1-(x/a)^2}\frac{12}{Re}\frac{\dot{h}x}{h^3} . \tag{2.23}$$

Equations 2.20, 2.23 will be used during the lubrication phase as detailed next. As a reminder, these expressions are for a cylinder falling vertically toward a fixed wall. The same approach we followed in their derivation is used for other cases where rotation of the cylinder or translation of the wall occur.

2.3.3 Algorithmic treatment in the immersed interface framework

In what follows, we will give an overview of the collision model using the lubrication equations, for the case of a cylinder falling vertically toward a wall. The general concept is similar for other configurations and needs only some adjustments depending on the geometry (e.g. two objects *vs.* an object and a wall).

At each time step, the distance d between any lagrangian point and the wall, along the normal direction, is computed. When $d < 4\Delta n \approx 4\sqrt{(\Delta x)^2 + (\Delta y)^2}$ as shown on figure 2.4, the lubrication region is defined. Initially, it contains only the lagrangian point where the minimum gap height is attained. As the cylinder continues falling, the lubrication region covers more lagrangian points and is bounded by the points m_1 and m_2 where the condition $d < 4\Delta n$ starts, as shown on figure 2.4.

Consequently, for all points between m_1 and m_2, the new (analytic) expressions of f_τ and $(\partial f_n/\partial\alpha)$ (e.g. equations 2.20 and 2.23 for a vertically falling cylinder) are applied. For lagrangian points outside the lubrication region, the standard interpolation scheme is still in use. A 64-mode, Fast Fourier Transform-based filter (FFT) is used to filter out the noise from the sequences f_τ and $(\partial f_n/\partial\alpha)$ over all

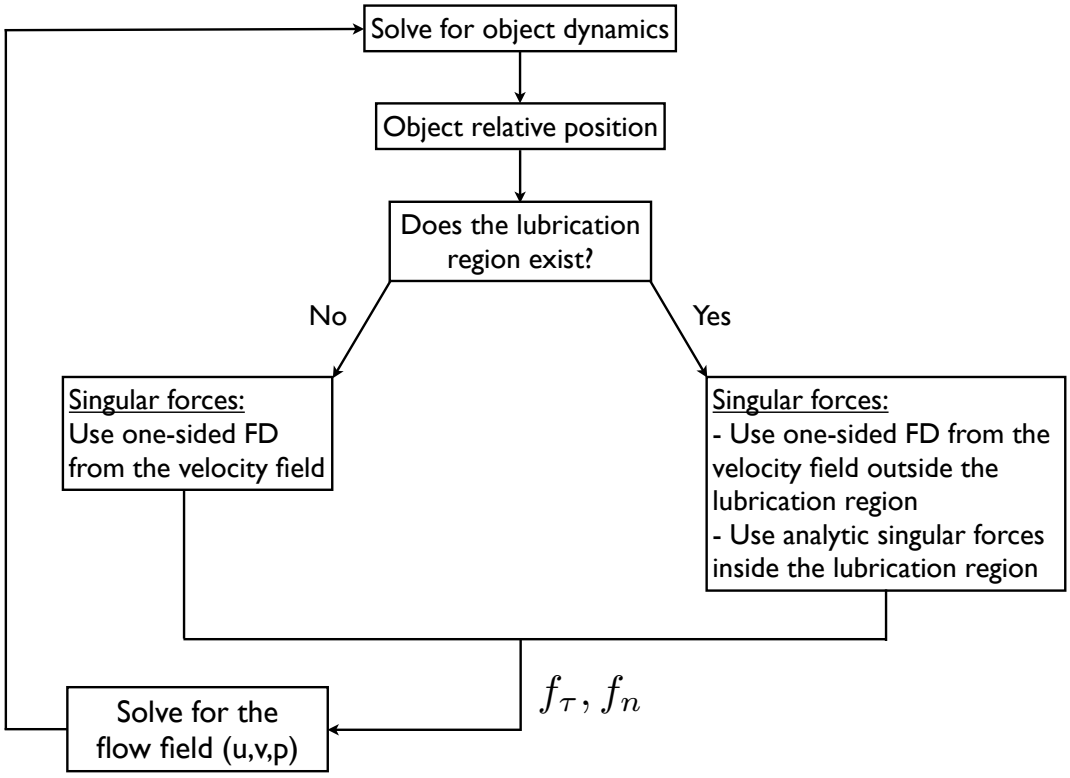

Figure 2.6: *Code-flow chart for the implementation of the lubrication theory.*

lagrangian points. An inverse FFT is also used to integrate $(\partial f_n/\partial\alpha)$ and obtain f_n. A sample code-flow chart is shown on figure 2.6. The object dynamics are solved for using equations 2.14, and then integrated using a fourth-order Runge Kutta scheme to get the object position. Then, the normal distance to the wall, at each lagrangian point, is computed. The singular forces are then computed accordingly, using the standard interpolation from the velocity field and/or the analytical expression from the lubrication theory when the lubrication region exists (see figure 2.4). These singular forces are then filtered and used back in equations 2.12 and 2.14 to update the field quantities and the object dynamics.

2.4 Results

2.4.1 Validity of the lubrication equations

In order to justify the use of the lubrication equations, we compare the pressure and fluid velocity in the gap region before and after using the analytical solution from the lubrication approximation. Namely, we compare the numerical u and (dp/dx) in the gap region, with their values using the analytic expressions from the lubrication equations. We use the results of a cylinder falling vertically toward a fixed wall, which will be detailed in section 2.4.2. The analytic expression of the velocity and the pressure gradient are given by equations 2.19a - 2.19b. The resolution in the vertical direction was doubled in order to have enough grid points to resolve the boundary layer, $\Delta y = \Delta y_{old}/2 = 1/160$. The triggering of the lubrication equations is kept with the same criterion as before ($d < 4\sqrt{(\Delta x)^2 + (\Delta y_{old})^2}$), since the conditions for Reynolds equations hold. The domain size is 640×2560, with no-slip boundary conditions on the bottom wall and Neumann boundary conditions on the left and right walls $(\partial\vec{v}/\partial x) = \vec{0}$, and on the top wall $(\partial\vec{v}/\partial y) = \vec{0}$.

Figure 2.7 shows the velocity u (top) and the pressure gradient dp/dx (middle) along the bottom-most grid line of the fluid domain. The inset shows that the analytical and numerical data match well, even right before using the lubrication solution. Additionally, since the singular forces are the quantities we enforce in our implementation of the lubrication theory, it is essential to compare their numerical and analytical values as well. Figure 2.7 (bottom) shows the distribution of f_τ and $(\partial f_n/\partial\alpha)$. In the lubrication region, there is a perfect match between the numerical and analytical data during the lubrication phase,

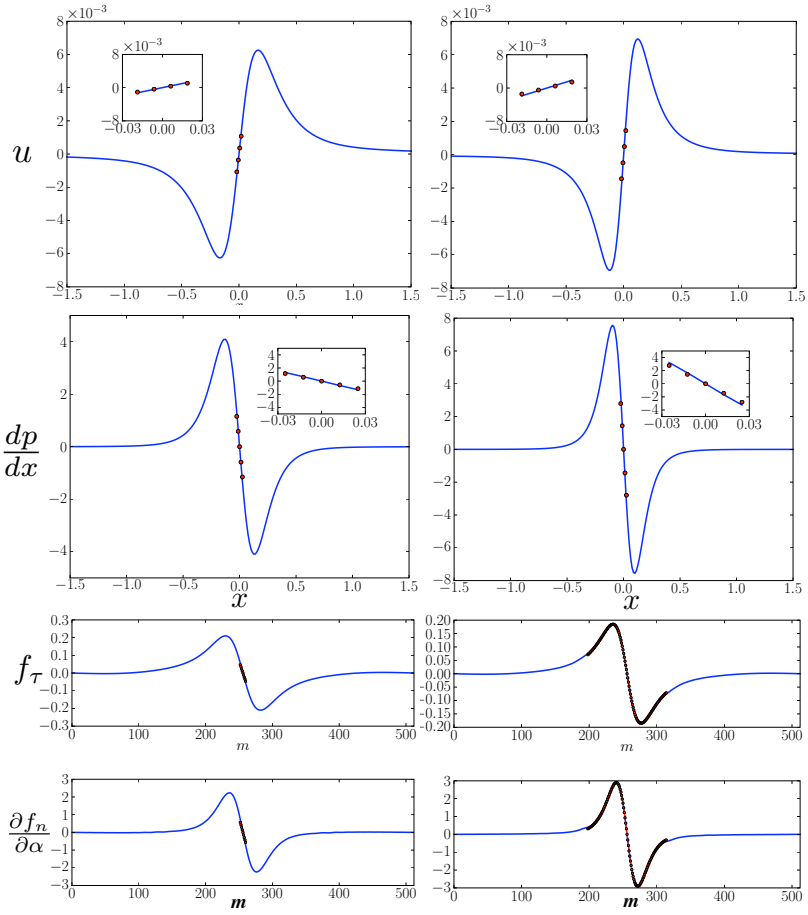

Figure 2.7: *Comparison between Navier Stokes solution (blue, solid lines) and lubrication results (red, dots) for the fluid velocity $u(x)$ (top), the pressure gradient dp/dx (middle), and the singular forces (bottom). Left: before the lubrication phase. Right: during the lubrication phase. Insets zoom on the lubrication region. The data for u and dp/dx are computed at the bottom-most grid line of the fluid domain.*

and the curves are consistent, even before the analytical solutions from lubrication are used.

Finally, during the lubrication phase, the pressure gradient and viscous term in equation 2.3 are four to five orders of magnitude higher than the inertia terms, hence justifying that the Navier-Stokes momentum equation 2.3 becomes Reynolds equation 2.5b in the lubrication limit.

2.4.2 Vertical fall of a cylinder toward a fixed wall

To validate our method, we present the case of a cylinder falling vertically toward a fixed wall. This configuration can be viewed as a limit case of two colliding cylinders, where one cylinder has an infinite radius.

First, in the absence of gravity, we compare the dynamics of a cylinder approaching a wall with data available from the literature on a sphere. We show that in the case of a cylinder, the gap height decays much slower than for a sphere, justifying the validity of the lubrication approximation for longer times, before other effects such as the surface roughness and molecular forces become dominant.

Next, we investigate the role of gravity in the settling dynamics of a cylinder. We quantify how the gap height depends on the Reynolds number and how the drag coefficient depends on the settling velocity in the inertial range. Additionally, we show that in the presence of gravity, the velocity cannot be zero in a finite time, since otherwise, there won't be a fluid force to balance the buoyancy force. Consequently, no contact occurs between the cylinder and the wall, in a finite time.

Comparison of the decay in the gap height for a cylinder and a sphere approaching a wall, in the absence of gravity

In the following section, we compare the dynamics of a cylinder approaching a wall, in the absence of gravity, with analytic data from the literature on spheres. We will show that for a cylinder, the gap height decreases algebraically as a function of a "modified" Stokes number, whereas the decay is exponential for

a sphere. Additionally, our results show that similar to a sphere, the cylinder comes to rest at a non-zero height from the wall, confirming that no contact occurs.

In the lubrication limit, a cylinder approaching a wall in the absence of gravity is subject to the force due to the pressure distribution in equation 2.19b. After integration, and keeping the leading term in $O(h_m^{-3/2})$ [32], we have the following ODE in v,

$$m_s \frac{dv}{dt} = -12\pi\mu v \left(\frac{a}{2h_m}\right)^{3/2} , \tag{2.24}$$

where $v = \dot{h}_m$ and μ is the fluid viscosity. We define $K = 12\pi\mu(a/2)^{3/2}/m_s$, and re-write equation 2.24 in terms of h_m

$$\ddot{h}_m + K\dot{h}_m h_m^{-3/2} = 0 . \tag{2.25}$$

We integrate once with respect to time and obtain an expression for the velocity v,

$$v = v_0 + 2K\left(\frac{1}{\sqrt{h_m}} - \frac{1}{\sqrt{h_{m,0}}}\right) , \tag{2.26}$$

where $v_0 = v(t_0)$, $h_{m,0} = h_m(t_0)$ and t_0 is the time marking the onset of the lubrication approximation. The initial conditions are fixed and are such that $v_0 = -1$ at an initial gap height $h_{m,0} = 0.04$, at which the lubrication effects exist. We solve for the value h_m^∞ of the minimum gap height at which the cylinder comes to rest. $v = 0$ implies that

$$\frac{h_m^\infty}{h_{m,0}} = \left(1 - \frac{v_0\sqrt{h_{m,0}}}{2K}\right)^{-2} . \tag{2.27}$$

The product $v_0\sqrt{h_{m,0}}/2K$ simplifies to

$$\frac{v_0\sqrt{h_{m,0}}}{2K} = -\frac{\gamma Re}{12}\sqrt{\frac{h_{m,0}}{2a}} ,$$

where $\gamma = \rho_s/\rho_f$ is the solid-to-fuild density ratio and $Re = \rho_f(2a)|v_0|/\mu$ is the Reynolds number, based on the cylinder diameter, $2a$, and the magnitude of the

initial velocity, v_0. We define $\tilde{S}_t \triangleq \gamma Re \sqrt{h_{m,0}/2a}$. Equation 2.27 thus becomes

$$\frac{h_m^\infty}{h_{m,0}} = \left(1 + \frac{\tilde{S}_t}{12}\right)^{-2} . \tag{2.28}$$

Consequently, h_m^∞ depends on a single non-dimensional parameter, $\tilde{S}_t$, which includes the effects of the fluid viscosity, the solid-to-fluid density ratio and the initial gap height. We will see, further below, that this parameter is the equivalent of a modified Stokes number. In this study, $\gamma = 1.5$ and $h_{m,0}/2a = 0.04$ are fixed, and the effect of $\tilde{S}_t$ is thus the effect of the Reynolds number. In our manuscript in preparation for a JFM paper [19], we will explore the effects of the solid-to-fluid density ratio γ and the initial gap height, $h_{m,0}$. Figure 2.8, left, shows the time series of the gap height and the approach velocity, for different values of the Reynolds number $Re = 2, 5, 10, 20, 50, 100, 250$, corresponding to $\tilde{S}_t = 0.6, 1.5, 3, 6, 15, 30, 75$. The lighter the grayscale, the higher the Reynolds. It is interesting to note that as Re increases, the profile of v resembles that of a step function. Figure 2.8, right, shows a log-log plot of the solution h_m^∞ to equation 2.28 as a function of the Reynolds number. When $Re \to \infty$, the gap height scales as $h_m^\infty \sim Re^{-2}$. This is shown through the dashed line.

We proceed in a similar way for a sphere approaching a wall. In the lubrication limit, the dynamics of a sphere in the absence of gravity are governed by the following ODE

$$m_s \frac{dv}{dt} = -6\pi\mu v a^2/h_m . \tag{2.29}$$

We define $K = 6\pi\mu a^2/m_s$ and re-write equation 2.29 in terms of h_m

$$\ddot{h}_m + K\frac{\dot{h}_m}{h_m} = 0 . \tag{2.30}$$

We integrate once and obtain an expression for v

$$v - v_0 + Klog\left(\frac{h_m}{h_{m,0}}\right) = 0 , \tag{2.31}$$

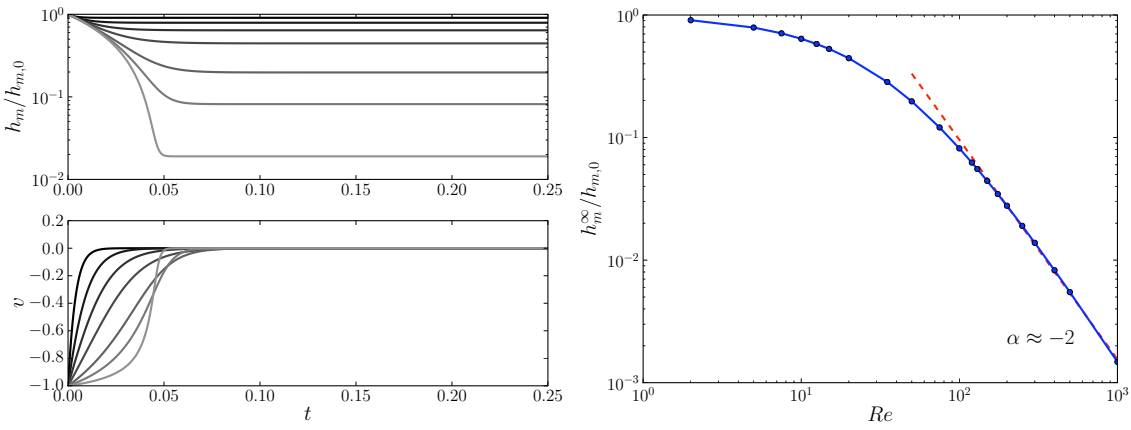

Figure 2.8: *Left: time series of the gap height (top), and the approach velocity (bottom) of a cylinder toward a wall, in the absence of gravity, for* $Re = 2, 5, 10, 20, 50, 100, 250$. *Lighter grayscale corresponds to higher Re. Right: Gap height* $h_m^\infty/h_{m,0}$ *at rest vs. Re. Solid, blue: analytic solution in equation 2.28. Dashed, red: linear fit in the log-log plot for large Re.*

where $v_0 < 0$ is the initial velocity imparted to the sphere, at an initial gap height $h_{m,0}$. The ratio v_0/K is

$$\frac{v_0}{K} = \frac{-|v_0|}{K} = -\frac{m_s|v_0|}{6\pi\mu a^2} = -S_t$$

where S_t is the Stokes number, defined as the ratio of the particle inertia to viscous forces. For a sphere, it is proportional to the Reynolds number $S_t = (1/9)(\rho_s/\rho_f)Re$, where the Reynolds number is based on the diameter of the sphere ($2a$) and the magnitude of the approach (initial) velocity $|v_0|$. To get the gap height when the sphere comes to rest, we set $v = 0$ and solve for $h_m = h_m^\infty$

$$\frac{h_m^\infty}{h_{m,0}} = e^{-St}\,. \tag{2.32}$$

Thus, the gap height has an exponential decay in terms of the Stokes number [22]. Comparing equations 2.28 and 2.32 shows significant differences between the dynamics in two and three dimensions. For a cylinder, the decay is algebraic; for a sphere it is exponential. The key parameter for a cylinder is the "modified"

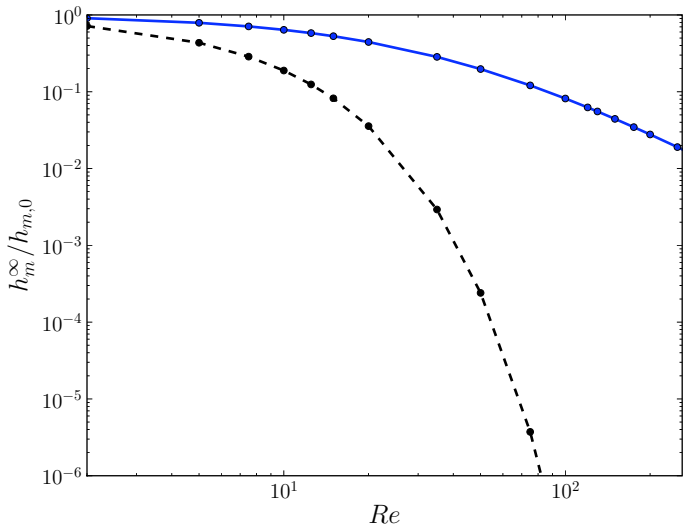

Figure 2.9: *Comparison between the gap height at rest for a cylinder (solid, blue, equation 2.28) and a sphere (dashed, black, equation 2.32), approaching a wall, in the absence of gravity.*

Stokes number, $\tilde{S}_t = \gamma Re\,\sqrt{(h_{m,0}/2a)}$, which not only depends on the density ratio γ and the Reynolds number, but also on the initial gap height. In contrast, the key parameter for a sphere is the Stokes number $S_t = \gamma Re/9$.

Figure 2.9 contrasts the gap height at rest for a cylinder and a sphere approaching a wall, in the absence of gravity. This result implies that for a cylinder, it will take a much longer time before micro-scale effects (surface roughness, van der Waals forces, etc) set in. As such, the lubrication approximation for a cylinder is valid for a longer time.

We conclude this subsection with a brief discussion on the non-contact argument between a cylinder or sphere and the wall. In three dimensions, previous experimental and theoretical studies [16, 22, 36, 63] have shown that for spheres in close contact, no rebound occurs provided the particles' Stokes number is finite and less than a critical value $S_t < S_{t,cr} \sim 10$. When $S_t < 10$, the particle inertia is small and cannot compensate for the viscous effects due to the inter-

stitial fluid. This causes the particles to slow down and come to a rest at a given separation. Theoretically, a particle with finite kinetic energy cannot come into contact with a smooth wall [28], in the incompressible continuum limit. Indeed, the kinetic energy accounts for the work of the increasing pressure force as the object approaches a wall

$$KE \propto \int F \, dh_m$$

where F is the resisting force. At the leading order, for a sphere, F is inversely proportional to the minimum gap height h_m [9, 22, 28]. For a cylinder, it is proportional to $h_m^{-3/2}$ [32]. The condition that the kinetic energy is finite, and not logarithmically or algebraically divergent, imposes that h_m is strictly positive, i.e no contact is to take place.

Effects of gravity on the dynamics of a cylinder approaching a wall

An important feature of our method is its ability to solve for the dynamics of particles both in the inertia dominant regime (e.g settling) and in the viscosity dominant regime (e.g lubrication phase). We illustrate this in figure 2.10 which shows snapshots of a settling cylinder under gravity. The particle accelerates as it settles and reaches its steady state velocity. This phase is characterized by a dominance of inertia. During its approach to the wall, the interstitial gap pressure builds up, causing the particle to decelerate and asymptotically come to rest. During this phase, the lubrication approximation is used and the flow is dominated by viscous effects.

In this section, we investigate the role of gravity on the dynamics of a settling cylinder. In particular, we ask whether the cylinder will come to rest as it approaches the wall and if contact is possible. In the incompressible, continuum

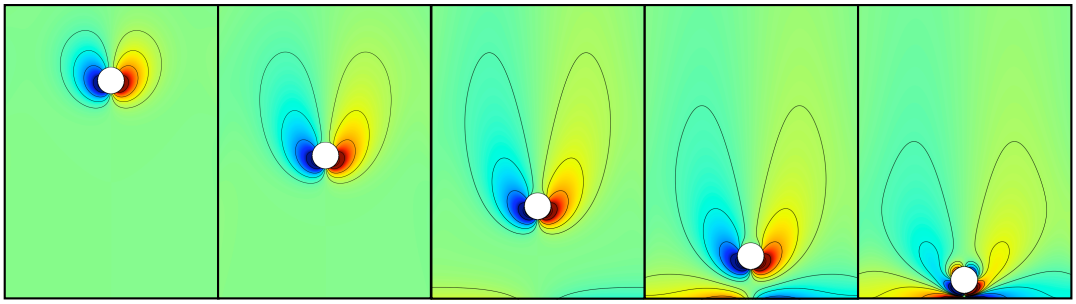

Figure 2.10: *Vorticity contour of a settling cylinder toward a fixed wall.* $Re = 10$.

limit, we will show that the settling velocity v cannot be zero in a finite time, since otherwise, there won't be a fluid force to balance the buoyancy force. As such, there cannot be a contact between the cylinder and the wall, in a finite time.

The dynamics of a cylinder settling under gravity are governed by the following ODE

$$m_s \frac{dv}{dt} = -(m_s - m_f)g - F_p \,, \tag{2.33}$$

where the pressure force due to lubrication is

$$F_p = 12\pi\mu v \left(\frac{a}{2h_m}\right)^{3/2} - \frac{6\mu a v}{h_m} \,. \tag{2.34}$$

We only keep the leading order term in in $O(h_m^{-/2})$ and define

$$K_1 = 12\pi\mu(a/2)^{3/2}/m_s \;\;,\;\; K_2 = (m_s - m_f)g/m_s$$

and re-write equation 2.33 in terms of h_m

$$\ddot{h}_m + K_1 \dot{h}_m h_m^{-3/2} + K_2 = 0 \tag{2.35}$$

Equation 2.35 is known as *Liénard's equation*. We integrate once to get the velocity v

$$v - v_0 - 2K_1 \left(\frac{1}{\sqrt{h_m}} - \frac{1}{\sqrt{h_{m,0}}}\right) + K_2(t - t_0) = 0 \tag{2.36}$$

where t_0 is the time marking the onset of the lubrication approximation, $\dot{h}_{m,0} = v_0 = v(t_0)$ and $h_{m,0} = h_m(t_0)$. In non-dimensional form, equation 2.36 becomes

$$v' - v'_0 - C_1 \left(\frac{1}{\sqrt{h'_m}} - \frac{1}{\sqrt{h'_{m,0}}} \right) + C_2(t' - t'_0) = 0 \,, \tag{2.37}$$

where $C_1 = 12/(\gamma Re)$ and $C_2 = 1/(2\gamma)$. The scales used in the dimensional analysis in equation 2.37 are $L = 2a$, $V = V_\infty$ the terminal velocity of the settling cylinder, long before its approach to the wall, $T = L/V$ and Re is based on L and V. To compute V_∞, we write the momentum equation of the cylinder at steady state and assume that the fluid force is a unit drag coefficient force. See section 3 in [18].

The analytic expression for the gap h_m is not readily available, so we integrate equation 2.37 numerically for different Reynolds numbers. Figure 2.11 shows the time history of the gap height (left) and magnitude of the settling velocity (right) for $Re = 10, 25, 50, 100, 120, 200$. The solid blue portions of the curves correspond to the numerical solution in the immersed interface method and the dashed red portions to the solution of equation 2.35. For a given time t, the higher the Reynolds number Re, the smaller the gap height and the velocity are. In other words, as the Reynolds number decreases, there is a remarkable increase in the time it takes before micro-scale effects (surface roughness, molecular nature of the fluid) set in. Additionally, the velocity curves show that the velocity, albeit small, is not zero (within the machine accuracy). The solution to equation 2.35 is computed with an initial condition such that there is an overlap with the numerical solution. We do so in order to highlight the onset of the lubrication effects before the gap actually reaches the threshold value that sets in the lubrication calculations in the code. These effects are shown in the inset of figure 2.11, where the time, t^*, marking the peak in the acceleration, and thus

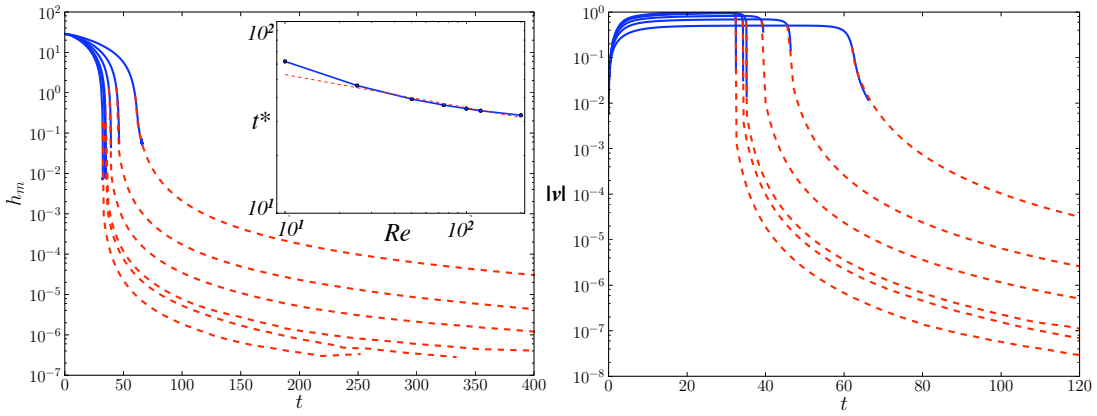

Figure 2.11: *Time series of the gap height h_m (left) and magnitude of the settling velocity (right), for different Reynolds numbers $Re = 10, 25, 50, 100, 120, 200$. the higher the Reynolds number, the smaller h_m is. Solid, blue: numerical results. Dashed, red: analytic results from lubrication approximation. Inset: log-log plot of the onset of the lubrication effect vs. Re.*

the onset of the lubrication effects, is plotted against the Reynolds number. The log-log plot shows that there is a linear fit for $Re \geq 25$, that is, $t^* \propto Re^{\alpha}$, where $\alpha = -0.14$.

During the inertial phase, that is, when the cylinder falls and reaches its steady-state terminal velocity before approaching the wall, we compare the terminal velocity and the dependency of the drag coefficient on the Reynolds number. The drag coefficient is defined as the fluid force coefficient, C_y, divided by the square of the non-dimensional velocity v, i.e $C_D \triangleq (C_y/v^2)$. Figure 2.12 shows an example of the relationship between C_D and v, using a log-log plot, at $Re = 10$. The solid blue curve corresponds to the numerical results. The lower portion corresponds to the inertial phase, and the upper one to the phase where lubrication effects set in. The red, dashed curve is a linear fit for the inertial phase, which shows that $C_D \propto v^{\alpha}$, $\alpha = -1.82$. This means that for the fluid force coefficient, we have, $C_y \propto v^{0.18}$. This relationship also applies for other values of

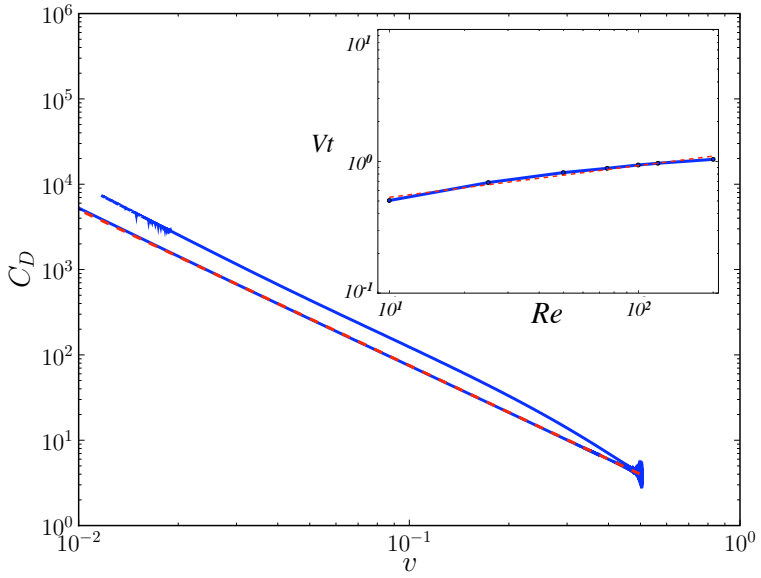

Figure 2.12: *Log-log plot of the drag coefficient $C_D(t)$ vs. the settling velocity $v(t)$, for $Re = 10$. Inset: terminal velocity during the inertial phase vs. Re, for $Re = 10, 25, 50, 75, 100, 120, 200$. Solid, blue: numerical data. Red, dashed: linear fit in the log-log plot (see text). Data for a cylinder settling under gravity.*

$Re = 10 \ldots 200$, and the exponent varies $\alpha = -1.82 \ldots -1.88$. The inset in figure 2.12 shows a log-log plot of the terminal velocity V_t of the cylinder, during the inertial phase, as a function of the Reynolds number. The linear fit (red, dashed) shows that $V_t \propto Re^{\alpha}$, $\alpha \approx 0.25$.

Finally, for illustrative purposes, we choose the case $Re = 10$ and present results on the settling velocity, acceleration, gap height as well as the pressure distribution in the gap, for a cylinder settling under gravity. Figure 2.13(a) shows that the cylinder accelerates initially due to gravity, reaches its terminal velocity around $t \approx 30$, then decelerates as the effect of the pressure force increases, $t \approx 60 \ldots 62$. The analytic solution in equation 2.35 is in agreement with our numerical results, as shown by the red, dotted portion of the curves in figure 2.13(a). Since equation 2.36 is valid only when the gap height at the center, h_m,

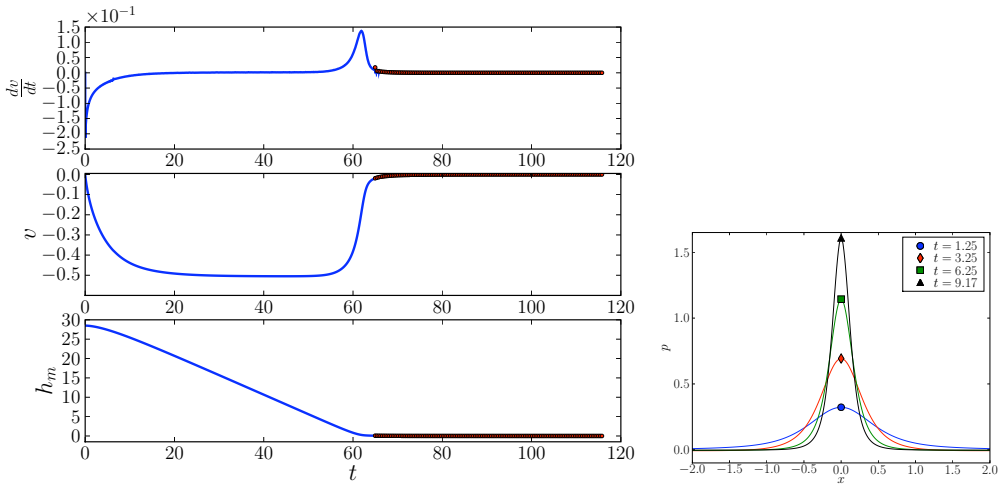

(a) *Acceleration, velocity and gap height* (b) *Interstitial pressure*

Figure 2.13: *(a) Acceleration, velocity and gap height of a cylinder falling vertically toward a fixed wall. Numerical (solid, blue) and analytic solution of equation 2.36 (red, circle). (b) Pressure distribution, at different times, on the bottom-most grid line for a cylinder falling vertically toward a fixed wall.* $Re = 10$.

is small enough for the lubrication theory to hold, we use the initial condition $v = v_0$ corresponding to the time when the lubrication phase is triggered in the simulation (i.e $h_m \leq 4\Delta y$). Using v_0 for when the peak in acceleration is reached, leads to similar results. In the ODE solver, we included the term in $O(1/h_m)$ $(6\mu va/h_m)$ in the expression of the pressure force F_p to have a better match with numerics, at the onset of the lubrication phase.

Pressure and body forces balance and the cylinder comes asymptotically to rest, at a distance $h_m \approx 0.04$ from the wall. Note that this distance from the numerics decreases for higher values of Re. For example, $h_m \approx 0.007$ for $Re = 200$. The analytic portion of the gap height curve in figure 2.11 shows that h_m asymptotically tends to $h_m^\infty = O(10^{-5})$, and v, albeit small, is not zero. Thus, as claimed, contact does not occur. This is opposite to what happens in the absence

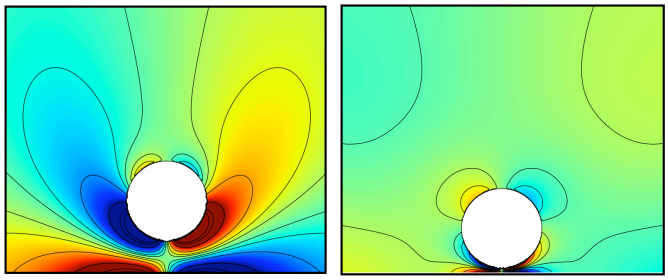

Figure 2.14: *Vorticity contours during approach, for a cylinder falling vertically toward a fixed wall. Clockwise vorticity (red), counter-clockwise vorticity (blue). Contour lines in white are used for ease of reading.* $Re = 10$.

of gravity, as shown in the previous subsection.

The pressure distribution on the bottom-most horizontal grid line is shown on figure 2.13(b). As time increases, the pressure peak in the gap increases and the neck becomes narrower. Finally, figure 2.14 shows the vorticity contours during approach, at $Re = 10$.

2.4.3 Fixed cylinder above a translating wall

The results presented in section 2.4.2 give predictions for head-on (normal) collisions in the lubrication limit. We now wish to capture the basics of the dynamics of oblique collisions. During oblique collisions, shear forces are predominant and the motion is characterized by a non-zero relative tangential velocity and rotation. In this section, we focus on the relative tangential motion and study the dynamics of a cylinder fixed over a translating wall. The gap distance is kept fixed to $h_m = 0.05$, a height at which the lubrication equations are valid (see section 2.4.2). However, in this case, we increase the resolution in the y-direction $\Delta y = \Delta x/2 = 1/160$ in order to have more grid points for the same height as

before. The test for the lubrication region is the same as before, with the old y-resolution, $d < 4\sqrt{(\Delta x)^2 + (2\Delta y)^2}$, ($\Delta y_{old} = 2\Delta y$). The domain size is 1280×640. We use a Dirichlet boundary condition on the bottom wall, $\vec{v} = (U, 0) = (1, 0)$ where $U = 1$ is the velocity of the wall; and Neumann boundary conditions, ($\partial\vec{v}/\partial x = \vec{0}$) on the left and right walls, and ($\partial\vec{v}/\partial y = \vec{0}$) on the top wall.

In equation 2.6, the boundary conditions are $u_1 = U$, $u_2 = 0$. Hence,

$$u = U\left(1 - \frac{y}{h}\right) + \frac{Re}{2}\frac{dp}{dx}y(y - h) \tag{2.38}$$

For the pressure gradient, the only non-zero term on the left-hand side of equation 2.10 is

$$\frac{\partial(\overline{u}h)}{\partial x} = \frac{U}{2}\frac{dh}{dx}$$

and the equation for pressure is

$$\frac{U}{2}\frac{dh}{dx} = \frac{Re}{2}\frac{d}{dx}\left(h^3\frac{dp}{dx}\right) \tag{2.39}$$

The volume flux across the gap, Q, is

$$\begin{aligned} Q &= \int_0^h u\,dy \\ &= \frac{Uh}{2} - \frac{Re\,h^3}{12}\frac{dp}{dx} \qquad (2.40) \\ \Rightarrow \qquad \frac{dp}{dx} &= \frac{6U}{Re\,h^2} - \frac{12Q}{Re\,h^3} \qquad (2.41) \end{aligned}$$

Unlike the case in section 2.4.2, the volume flux Q here is constant, because there is no change in height at a given location x. In particular, at $x = 0$,

$$Q = Q_0 = \frac{Uh_m}{2} - \frac{Re\,h_m^3}{12}\frac{dp}{dx}_0 \tag{2.42}$$

Numerically, the pressure gradient $(dp/dx)_0$ can be approximated, at each time step, from the pressure field, using a centered finite-difference scheme at $x = 0$,

$$\frac{dp}{dx}_0 \approx \frac{p(\Delta x) - p(-\Delta x)}{2\Delta x}$$

Combining equations 2.40, 2.41, 2.42 and the approximation for $(dp/dx)_0$, we obtain the solution for the pressure gradient in the lubrication limit

$$\frac{dp}{dx} = \frac{6U}{Re\, h^2}\left(1 - \frac{h_m}{h}\right) + \left(\frac{h_m}{h}\right)^3 \frac{p(\Delta x) - p(-\Delta x)}{2\Delta x} \tag{2.43}$$

In summary, equations 2.38 and 2.43 are the solutions to Reynolds equations 2.5a - 2.5b for a cylinder fixed above a translating wall, in the lubrication limit. The tangential component of the singular force is obtained by combining equations 2.18 and 2.38,

$$f_\tau = -\frac{U}{Re\, h} + \frac{h}{2}\frac{dp}{dx} \tag{2.44}$$

We remark that the difference between this expression of f_τ and equation 2.20 is the shear contribution from the Couette flow due to the translation of the wall. Likewise, for the normal component, we combine equations 2.21 and 2.22, and use the fact that the body force $\vec{f_b}$ is zero, since the cylinder is fixed

$$\frac{\partial f_n}{\partial \alpha} = J\sqrt{1 - (x/a)^2}\,\frac{dp}{dx} \tag{2.45}$$

where dp/dx is given by equation 2.43.

Figure 2.15 shows the pressure and pressure gradient distributions along the bottom-most grid line of the domain. The inset shows that the numerical and analytical data match very well in the lubrication region. As time increases, the boundary layer at a given location x thickens and causes the pressure to augment, as we can see, for example, from the time evolution of the pressure peak on figure 2.15(b).

Figure 2.16(a) shows the velocity profile across the gap at four different locations: at the middle, half-way, at the exit and outside of the lubrication region. The abscissa x_{max} is that of the lagrangian point m_2 on figure 2.4. There is a good match between the numerical and analytic data from equation 2.38. The velocity

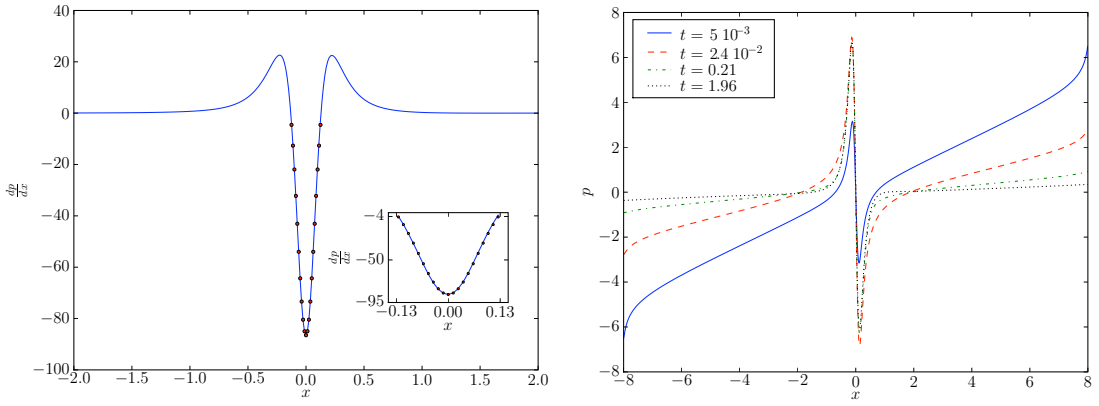

(a) *Pressure gradient* (b) *Pressure*

Figure 2.15: *Pressure gradient and pressure distribution on the bottom-most grid line for a cylinder fixed over a translating wall. (a) Numerical (solid, blue) and analytical (equation 2.43) (dots, red) data. The inset zooms on the lubrication region. (b) Pressure distribution at different times, on the bottom-most grid line.*

profiles highlight the competition between the Couette and the Poiseuille contributions in equation 2.38. The former has a linear profile in y, whereas the latter has a parabolic profile. The pressure gradient is negative for $x = 0,\ x_{max}/2,\ x_{max}$ and its magnitude is higher the closer to $x = 0$, signaling a predominance of the Poiseuille flow. Hence, the velocity profile is concave-down (solid, dashed and dot-dashed curves on figure 2.16(a) and the curvature decreases the further from the middle (dot-dashed curve).

Outside the lubrication region where $dp/dx > 0$ on figure 2.15(a), the Poiseuille contribution acts against the Couette flow. This causes a concave-up velocity profile as shown on the dotted curve ($x = a/2$) in figure 2.16(a). We remark that the analytic and numerical data also match well outside of, but close enough to, the lubrication region. The shapes of these profiles are in agreement with those in [51], p. 247, when flipped upside-down, given that the case

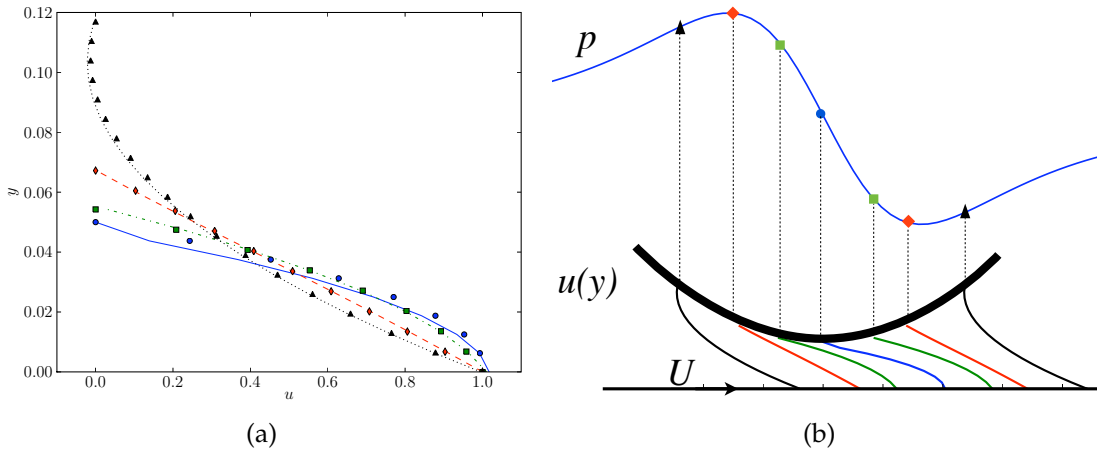

(a) (b)

Figure 2.16: *Velocity profile $u(y)$ in the gap between a cylinder fixed above a wall translating at velocity U. (a) Numerical (curves) and analytic (symbols) data: at the middle ($x = 0$, blue, solid, circles), half-way in the lubrication region ($x = x_{max}/2$, green, dot-dashed, squares), at the exit of the lubrication region ($x = x_{max}$, red, dashed, diamonds), and outside the lubrication region ($x = a/2$, black, dotted, triangles). (b) Pressure and velocity profiles at corresponding points. See (a). The thick arc represents the cylinder.*

reported in by [51] is for a translating cylinder over a fixed wall.

The pressure profile on figure 2.15(b) shows that the cylinder is separated from the wall on the left and attracted to the wall on the right. This will create a counter clockwise torque on the cylinder about its center of mass

$$T_{/c} = a \int_{\Gamma} f_\tau \, d\theta \tag{2.46}$$

where f_τ is given by equation 2.44 and $d\theta = dx/\sqrt{a^2 - x^2}$. We emphasize that the position and rotation of the cylinder are constrained (fixed cylinder) and that the computed torque is experienced by the cylinder at its hinge (center) due to the shear force. Equation 2.46 can be integrated analytically between the limits of the lubrication region $x = -x_L \ldots x_L$ where the contribution of the shear force

is predominant,

$$T_{/c} = -\frac{2Ua}{Re}\underbrace{\int_{-x_L}^{x_L}\frac{dx}{h\sqrt{a^2-x^2}}}_{(1)} + \frac{6Qa}{Re}\underbrace{\int_{-x_L}^{x_L}\frac{dx}{h^2\sqrt{a^2-x^2}}}_{(2)} \tag{2.47a}$$

where

$$(1) \approx \frac{2\pi}{a}\left(\frac{a}{2h_m}\right)^{1/2} \qquad \textit{and} \qquad (2) \approx \frac{2\pi}{a^2}\left(\frac{a}{2h_m}\right)^{3/2}$$

We use the flux Q given by equation 2.42 and keep the leading terms in $O((a/h_m)^{1/2})$. We obtain

$$T_{/c} \approx -\frac{\pi U}{Re}\left(\frac{a}{2h_m}\right)^{1/2} \tag{2.47b}$$

For $a = 0.5$, $h_m = 0.05$, $U = 1$, $Re = 10$, we have

$$T_{/c} \approx -0.702$$

And numerically, we obtain

$$T_{/c}^{num} = -0.820$$

The slight discrepancy is attributed to the truncation error in the analytic expression.

2.4.4 Rotating cylinder above a fixed wall

Another aspect of the relative motion of two objects is their relative rotation. To capture these dynamics in the lubrication limit, we study the dynamics of a cylinder rotating above a fixed wall, with a constant angular velocity. Similar to the case in section 2.4.3, the gap distance is kept fixed to $h_m = 0.05$, the resolution in the y-direction is $\Delta y = \Delta x/2 = 1/160$ and the same test for the lubrication is used $d < 4\sqrt{(\Delta x)^2 + (2\Delta y)^2}$, ($\Delta y_{old} = 2\Delta y$). The domain size is 1280×640. We use a Dirichlet boundary condition on the bottom wall, $\vec{v} = \vec{0}$, and Neumann

boundary conditions, ($\partial\vec{v}/\partial x = \vec{0}$) on the left and right walls, and ($\partial\vec{v}/\partial y = \vec{0}$) on the top wall. Unlike the case in section 2.4.3, the lagrangian points in the lubrication region change as the cylinder rotates.

In equation 2.6, the boundary conditions are $u_1 = 0$, $u_2 = \dot{\theta}\sqrt{a^2 - x^2}$, where $\dot{\theta} = 1$ is fixed. Hence,

$$u = \frac{\dot{\theta}\sqrt{a^2 - x^2}}{h}\, y + \frac{Re}{2}\frac{dp}{dx} y(y - h) \tag{2.48}$$

The volume flux across the gap is

$$\begin{aligned} Q &= \int_0^h u\, dy \\ &= \frac{\dot{\theta}\sqrt{a^2 - x^2}h}{2} - \frac{Re\, h^3}{12}\frac{dp}{dx} \qquad (2.49) \\ \Rightarrow \qquad \frac{dp}{dx} &= \frac{6\dot{\theta}\sqrt{a^2 - x^2}}{Re\, h^2} - \frac{12Q}{Re\, h^3} \qquad (2.50) \end{aligned}$$

Since the height of the gap does not change, the flux along the horizontal is constant and we can equate its value to that at $x = 0$

$$Q = Q_0 = \frac{a\dot{\theta}h_m}{2} - \frac{Re\, h_m^3}{12}\frac{dp}{dx}_0 \tag{2.51}$$

We follow the same steps in section 2.4.3 to find $(dp/dx)_0$ using a centered finite-difference scheme approximation.

The tangential singular force is

$$\begin{aligned} f_\tau &= -\frac{1}{Re}(\omega^+ - \omega^-) \\ &= -\frac{1}{Re}\left(-\frac{\partial u}{\partial y} - 2\dot{\theta}\right) \\ &= \frac{1}{Re}\left(\frac{\dot{\theta}\sqrt{a^2 - x^2}}{h} + 2\dot{\theta}\right) + \frac{h}{2}\frac{dp}{dx} \qquad (2.52) \end{aligned}$$

The expression of $(\partial f_n/\partial\alpha)$ is the same as in equation 2.45 since $\ddot{\theta} = 0$ and hence, the body force component in equation 2.21 is $[\vec{f_b}] \cdot \vec{\tau} = 0$.

Figure 2.17 shows the pressure and pressure gradient distributions along the

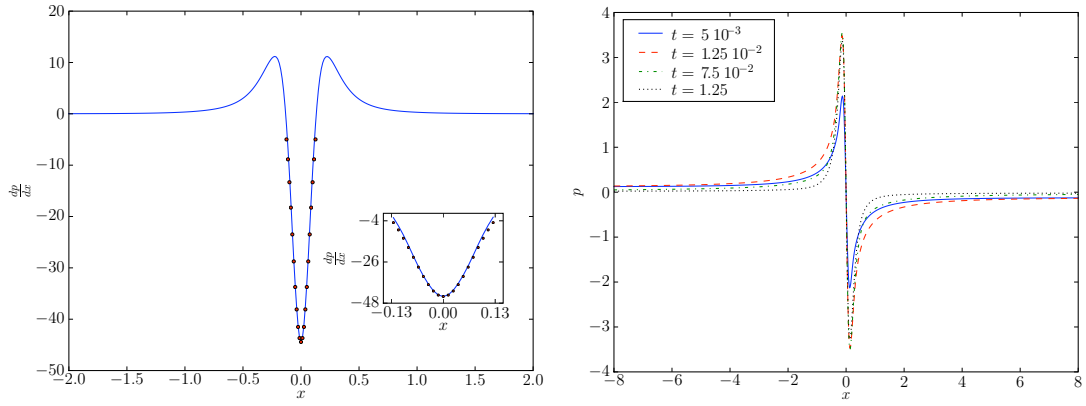

(a) *Pressure gradient* (b) *Pressure*

Figure 2.17: *Pressure gradient and pressure distribution on the bottom-most grid line for a cylinder rotating above a fixed wall. (a) Numerical (solid, blue) and analytical (equation 2.50) (dots, red) data. The inset zooms on the lubrication region. (b) Pressure distribution at different times, along the bottom-most gridline.*

bottom-most horizontal grid line of the domain. The inset shows that the numerical and analytical data match very well in the lubrication region.

Figure 2.18(a) shows the profile of the velocity u in the gap, at different locations x. The numerical and analytic results are in good agreement inside the lubrication region, with slight discrepancies outside.

The rotation of the cylinder create a pressure a profile, such that the cylinder is attracted tot he wall on the right, and repelled from the wall on the left. This generates a clockwise torque on the cylinder. Using the expression of the singular force in equation 2.52, the torque with respect to the center of mass of the cylinder is

$$T_c = \int -f_\tau (a\, d\theta) = \int -a\, f_\tau \frac{dx}{\sqrt{a^2 - x^2}}\,.$$

We combine the expressions in equations 2.50 and 2.52 and obtain

$$f_\tau = \frac{2\dot{\theta}}{Re}\left(\frac{2\sqrt{a^2 - x^2}}{h} + 1\right) - \frac{6Q}{Re\, h^2} \tag{2.53}$$

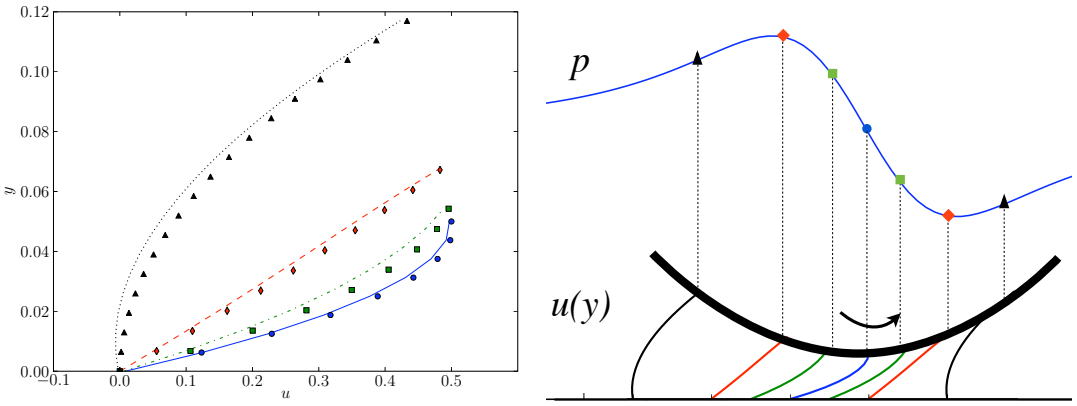

(a) (b)

Figure 2.18: *Velocity profile $u(y)$ in the gap between a cylinder rotating above a fixed wall. (a) Numerical (curves) and analytic (symbols) data: at the middle ($x = 0$, blue, solid, circles), half-way in the lubrication region ($x = x_{max}/2$, green, dot-dashed, squares), at the exit of the lubrication region ($x = x_{max}$, red, dashed, diamonds), and outside the lubrication region ($x = a/2$, black, dotted, triangles). (b) Pressure and velocity profiles at corresponding points. See (a). The thick arc represents the rotating cylinder.*

Thus,

$$T_{/c} = \int_{-x_L}^{x_L} -\frac{2\dot{\theta}a}{Re}\left(\frac{2}{h} + \frac{1}{\sqrt{a^2 - x^2}}\right) dx + \int_{-x_L}^{x_L} \frac{6Qa}{Re} \frac{dx}{h^2\sqrt{a^2 - x^2}} \tag{2.54a}$$

with $\pm x_L$ being the bounds of the lubrication region, as in the previous case. Keeping the dominant term, we obtain

$$T_{/c} = -\frac{4\pi a\dot{\theta}}{Re}\left(\frac{a}{2h_m}\right)^{1/2} + O(1)\,. \tag{2.54b}$$

See [32].

The vorticity contours on figure 2.19 indicate the presence of separation and reattachment points of the flow. To find their locations, we solve for x_{SP}

$$\frac{\partial u}{\partial y} = 0 \qquad at \qquad y = 0 \tag{2.55}$$

where the velocity profile u is given by equation 2.48. Given the left-right symmetry, we will solve for $x_{SP} > 0$. Equation 2.55 has four roots, two positive and two negative. Of the positive ones, one is a separation point, x_{SP}, and the other is a reattachment point, x_{RP}, with $x_{SP} < x_{RP}$. We obtain $x_{SP} \approx 0.254$. This is the analytical separation point. Numerically, it is sufficient to find the x-coordinate of the point where the vorticity is zero since $\omega \approx -(\partial u/\partial y)$. We find that $x_{SP} \approx 0.212$. In [32], the right separation point is located at $X = \sqrt{2}$, where

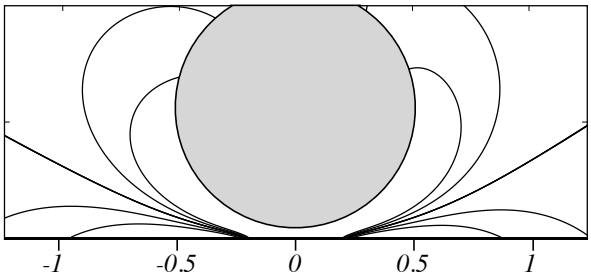

Figure 2.19: *Vorticity contours for a cylinder rotating above a fixed wall. Vorticity bubbles below the cylinder indicate the presence of separation and reattachment points.*

$X = x/a\sqrt{\epsilon}$, $\epsilon = h_m/a$. Re-writing X with our dimensional analysis, we have

$$X' = \frac{x}{2a} = \frac{\sqrt{h_m/a}X}{2} \approx 0.223$$

in close agreement with our result.

2.5 Conclusion

We have developed a numerical scheme to treat collisions of objects in a viscous fluid in the immersed interface method framework. Upon close interaction, the Reynolds equations are solved in terms of the velocity field, u, and the pressure gradient, (dp/dx), in the lubrication theory limit. These solutions are then used

to compute the analytical expressions of the singular forces, thus bypassing the one-sided, three-point stencil finite-difference interpolation from the velocity or the vorticity field, in the lubrication region. The interpolation is still used in the outer region, and a weighted ramping smoothing is used between the inner and outer regions. We solved the Reynolds equations for three fundamental cases of close interactions between solid interfaces: cylinder vertically falling toward a fixed wall, fixed cylinder above a translating wall and rotating cylinder above a fixed wall. The former case provides an insight into normal collisions between objects whereas the two latter cases provide key results on oblique collisions, where shear and relative transverse motion are dominant.

In all three cases, our analytical pressure and pressure force expressions are in agreement with previous theoretical results. The numerical results for the velocity profiles in the gap region, the location of the separation points (rotation case), the prediction of the no-rebound of the vertically falling cylinder are also in agreement with previous theoretical studies.

We provided more insight into the dynamics of a cylinder approaching a wall. In the absence of gravity, we compared the dynamics of a cylinder with analytic data from the literature on spheres. We showed that for a cylinder, the gap height decreases algebraically as a function of a "modified" Stokes number, which factors in the effects of the solid-to-fluid density ratio, the Reynolds number and the initial gap height. In contrast, for a sphere, the decay is exponential in the Stokes number, which accounts for the effects of the Reynolds number and the solid-to-flui density ratio. This results implies that for a cylinder, it will take a much longer time before micro-scale effects (surface roughness, van der Waals forces, etc) set in. As such, the lubrication approximation for a cylinder is

valid for a longer time. Additionally, our results show that similar to a sphere, the cylinder comes to rest at a non-zero height from the wall, confirming that no contact occurs.

We then quantified the effects of gravity on the dynamics of a cylinder approaching a wall. We showed that with gravity, the particle cannot come to rest in the incompressible continuum limit, since otherwise, there won't be a fluid force to balance the buoyancy force. As such, there cannot be a contact between the cylinder and the wall, in a finite time.

Finally, we emphasize that our method has the advantage of treating dynamics of particles both in the inertia-dominant regime and in the viscosity dominant regime. The current method is under development to treat close-range multi-particle interactions.

CHAPTER 3

EFFECT OF THE REYNOLDS NUMBER AND THE SEPARATION ON THE DYNAMICS OF FALLING PLATES

3.1 Introduction

Andersen et *al* [1, 2] and Pesavento & Wang [50] studied the dynamics of freely falling plates in a quasi-steady flow in the intermediate Reynolds number regime ($Re = O(10^2 - 10^3)$). Their results show that the falling plates followed either a periodic motion or a chaotic one. In the former, the dynamics were insensitive to initial conditions, and the plates were either fluttering or tumbling. The fluttering motion is characterized by long glides at low angles of attack, and were achieved by plates with a low thickness-to-width ratio. The tumbling motion, by contrast, is characterized by the predominance of rotation and a side-to-side rocking motion. On the other hand, the chaotic falling mode is not sensitive to initial conditions. Pesavento & Wang [50] then developed a quasi-steady model, which is a fluid force model based on ordinary differential equations, derived from their experimental and direct simulation results. The quasi-steady model allowed for the exploration of the rich set of dynamics and showed how they depended on the Reynolds number of the flow, the moment of inertia and the thickness-to-width ratio of the plates. The model also predicted the transition between fluttering and tumbling.

In their study [1, 2, 50], Andersen, Pesavento and Wang produced a phase diagram spanned by the Reynolds number, the non-dimensional moment of inertia and thickness-to-width ratio of the plates. The fluid properties were fixed and the plate geometry was varied. In this chapter, we use our new imple-

mentation of the immersed interface method to simulate freely falling plates. In particular, for a fixed geometry of the plate, we study how the Reynolds number affects the dynamics of a falling plate and how these fit in the previous phase diagram. We then fix the Reynolds number and the plate geometry, and study its dynamics in the presence of a neighboring plate. We find that this configuration is equivalent to that of a plate falling nearby a wall.

3.2 Effect of the Reynolds number

We solve for the coupling between the free falling plate and the surrounding fluid using the immersed interface method. Namely, we solve Navier-Stokes equations coupled to Newton's dynamics, similar to equations 1.1 and 1.4 in section 1.2.1. In non-dimensional form, we write:

$$\frac{\partial \vec{v}}{\partial t} + \vec{v} \cdot \nabla \vec{v} = -\nabla p + \frac{1}{Re} \nabla^2 \vec{v} + \int_\Gamma \vec{f}(\alpha, t)\, \delta(\vec{x} - \vec{X}(\alpha, t))\, d\alpha \tag{3.1a}$$

$$\nabla \cdot \vec{v} = 0 \tag{3.1b}$$

$$m_s \dot{\vec{v}}_c = \vec{F}_{ext} + \vec{F}_f \tag{3.1c}$$

$$I^* \ddot{\theta} = T_f \tag{3.1d}$$

where m_s is the non-dimensional mass of the plate, I^* its moment of inertia with respect to its center of mass, $\vec{F}_{ext}$ is the external non-fluid force on the plate (buoyancy-corrected weight), $\vec{F}_f$ is the fluid force on the plate, and T_f is the fluid torque on the plate with respect to its center of mass. We use a rounded rectangular plate, comprised of a rectangle, of width a, with two half disks of diameter b on each side, as shown on figure 3.1. In the dimensional analysis, we used $L = a + b$, the width of the plate, as the length scale. The velocity scale is the

average descent speed V, obtained by balancing the buoyancy-corrected weight with a unit-drag coefficient quadratic drag force. See section 1.2.2. The mass and moment of inertia are made non-dimensional through a division by $\rho_f L^2$ and $\rho_f L^4$, respectively. Note that our value of I^* is different from that in [2] by a factor of $\pi/32$, where $\tilde{I}^* = I/(\pi\rho_f L^4/32)$. To avoid any confusion, we define $\tilde{I}^*$ as non-dimensional I following the convention in [2]. The plate thickness-to-width

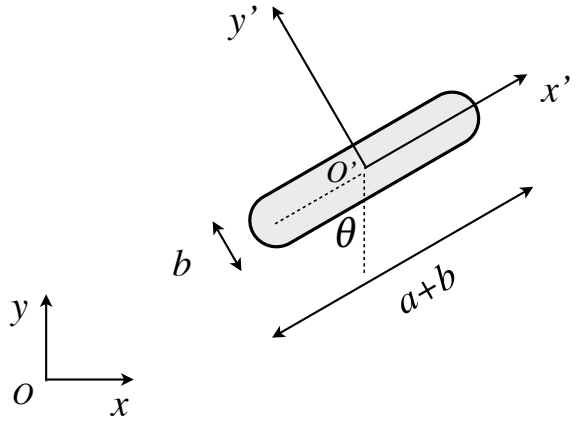

Figure 3.1: *Sketch of the plate geometry and the local co-moving frame* (O', x', y'). *b and* $a + b$ *are the thickness and width of the plate, respectively.* θ *is the angle between the major axis of the plate and the vertical.*

ratio is fixed at $\beta = 1/5$, the density of the plate to the fluid is $\gamma = \rho_s/\rho_f = 2.56$ and the non-dimensional moment of inertia is $I^* = 0.04$, corresponding to $\tilde{I}^* = 0.4$. The domain size is 24×32, with a grid cell size $\Delta x = \Delta y = 1/80$ providing enough grid points across the thickness. The time step Δt varies in the range $10^{-3} - 4\,10^{-3}$ for a Reynolds varying between 50 and 200. The plate is dropped edge-on with zero initial velocity.

Figure 3.2 shows trajectory snapshots of the falling plate for different Reynolds numbers. The dynamics vary significantly. For $Re \leq 60$, the plate exhibits a broadside, dampened motion. As the Reynolds number increases, the plate starts to flutter for $75 \leq Re \leq 100$, with a mix of fluttering and tum-

bling for $Re \sim 125$. The plate then falls into a period-one tumbling motion, with a long lateral drift and a -45° descent angle for $Re = 150$. Finally, for $Re = 200$, the plate falls into a period-two tumbling motion, characterized by steep glides, interspersed between two consecutive tumbles. A closer look at the $(\theta, \dot{\theta})$ phase

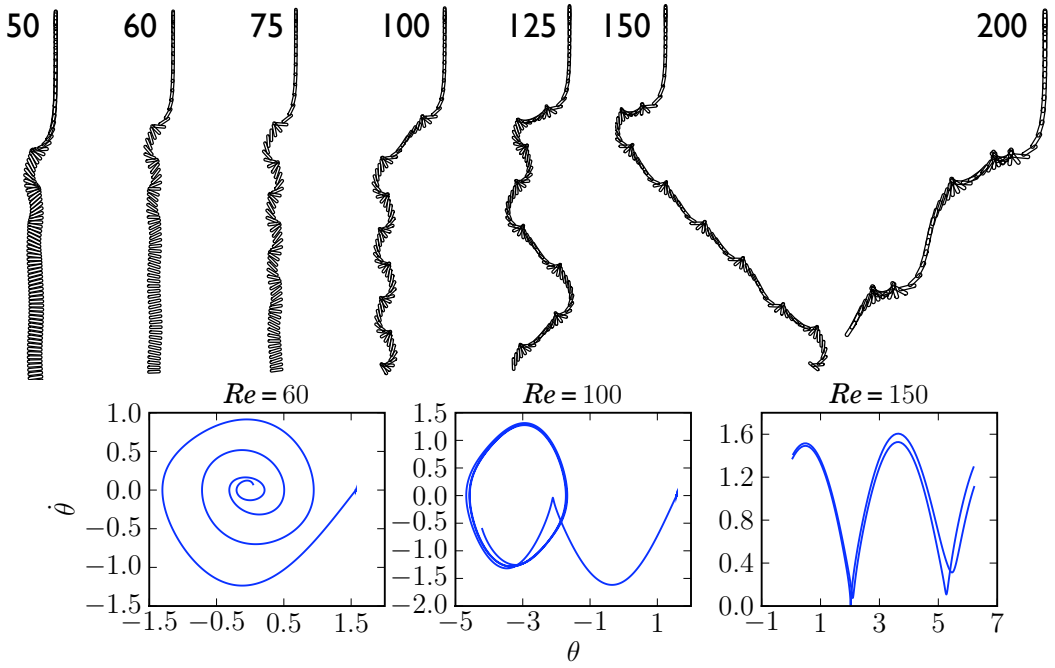

Figure 3.2: *Top: Trajectories of an edge-on falling plate for different Reynolds numbers. Bottom: phase portrait in the $(\theta, \dot{\theta})$ plane, varies from a stable fixed point ($Re = 60$), to an unstable limit cycle ($Re = 100$), which bifurcates into a homoclinic trajectory ($Re = 150$). θ in radians. For $Re = 150$ (tumbling), we plot mod$(\theta, 2\pi)$.*

plane at the bottom of figure 3.2 shows that the broadside falling motion is a stable (attractive) fixed point. At $Re = 100$, we observe a limit cycle, which is unstable since trajectories in the $(\theta, \dot{\theta})$ plane deviate from it when $Re \neq 100$. The details of the Hopf bifurcation characterizing the transition between fluttering and tumbling can be found in [1].

The plate dynamics, for fixed geometry and varying fluid properties, are in agreement with those in the phase diagram on figure 3.3, which was obtained

by [1] using the quasi-steady model. The red horizontal rectangle corresponds to the reading of the $(\tilde{I}^*, \mu_1)$ phase space in [1], where the fluid properties (μ_1) were fixed, and the plate geometry $(\tilde{I}^*)$ was varied. The plate, then, underwent a fluttering motion (open circles), followed by tumbling (stars), then chaotic motion (triangles) and finally broadside-on falling motion (crosses) as $\tilde{I}^*$ increased. In our case, we observe similar dynamics. Decreasing values of the

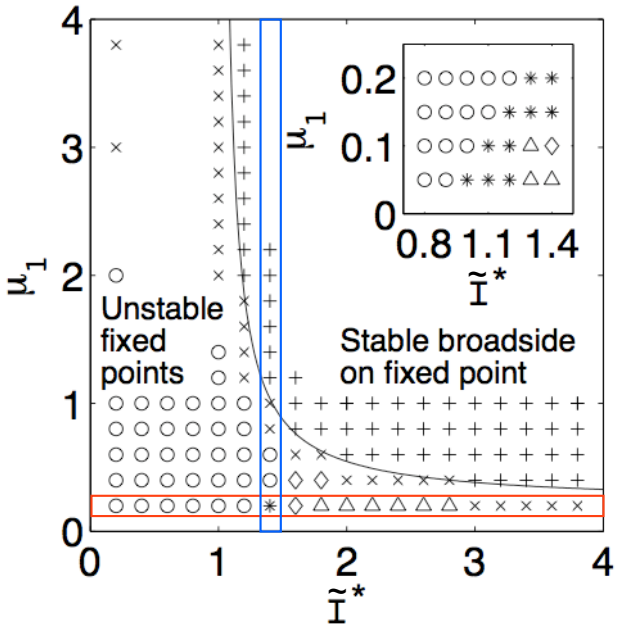

Figure 3.3: *Phase diagram in the $\tilde{I}^*$ vs. μ_1 plane, where μ_1 characterizes the fluid viscosity (see text above). For an explanation of the blue and red rectangular regions, see text. Original figure courtesy of [1].*

non-dimensional parameter μ_1 correspond to increasing values of the Reynolds number. In [1], μ_1 is a non-dimensional parameter in the dissipative torque model, which determines the time scale for the oscillations relative to the time scale of the vertical descent. As we can see from the blue vertical rectangle in figure 3.3, the plate follows a steady broadside-on descent (plus signs), then fluttering motion (open circles), followed by tumbling motion (stars), as μ_1 (or equivalently, *Re*) decreases (increases). For ease of reading and comparison, we

used data on figure 3.3 for $\tilde{I}^*$ higher than our case ($\tilde{I}^* = 0.4$).

In summary, although the mechanisms behind the instability in [1] are due to effects of the plate inertia, and in our case, they are flow-induced instabilities, the resulting dynamics are similar.

3.3 Effect of the relative separation

We now wish to study how the dynamics of a falling plate are affected by the presence of another plate. We use the same plate geometry as in section 3.2, where the thickness-to-width ratio is $\beta = 1/5$ and the solid-to-fluid density ratio is $\gamma = 2.56$. The Reynolds number is fixed at $Re = 200$. The plates are dropped edge-on, with zero initial velocity. The domain size is 32×32, with no-slip boundary conditions on all four walls. From a computational standpoint, we ask if the configuration of two side-by-side falling plates, separated by an initial center-to-center distance d_0, is equivalent to that of a single falling plate, initially at a distance $d_0' = d_0/2$ from a fixed wall. If that is the case, then we can explore the effect of the initial separation between two plates on their dynamics by simply studying a single falling plate near a wall. This will enable us to reduce the size of the computational domain by half, this saving in computing time.

We simulate two side-by-side edge-on falling plates, initially separated by $d_0 = 0.5$. The trajectories of the plates are shown on the left of figure 3.4(a). We notice a left-right mirror symmetry as well as a synchrony in their motion and dynamics. The trajectories consist of an overall fluttering motion, where each fluttering period consists of two tumbles. Instead of evolving into two independently tumbling plates, as is the case for an isolated plate (see figure 3.2,

$Re = 200$), the plates reverse their motion and remain side-by-side for the entire simulation. Initially, the domain was smaller (20×24) and it was speculated that the side walls caused the plates to revert back to the domain centerline. We however ruled out this hypothesis by choosing a larger domain (32×32) which yielded the same results. It seems then, that when two plates are dropped edge-on, from the same height, their dynamics are locked in synchronously for the entire motion. Figure 3.4(a) also shows the time history of the horizontal and

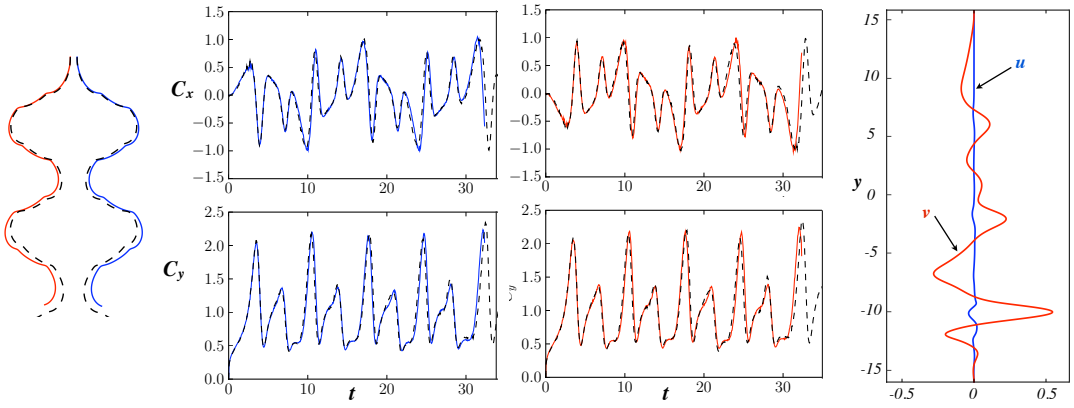

Figure 3.4: *(a) Trajectories (left) and time history of the lateral and vertical fluid force coefficients C_x and C_y, of edge-on falling plates. Black and dashed curves: two side-by-side falling plates; blue curves: single (right) plate near the left wall; red curves: single (left) plate near the right wall. (b) Fluid velocity on the vertical middle line of the domain at the end of the simulation. $Re = 200$.*

vertical fluid force coefficients. The black dashed curves are for two side-by-side plates, the blue (respectively, red) curves are for a single plate, near the left (respectively, right) wall, which is equivalent to the right (respectively, left) plate in a two-plate configuration. The time histories of a single plate near the left wall and those of the right plate in a two-plate configuration (blue curves) match well. The same applies to the red curves. The trajectories are also in good agreement, albeit with a slight discrepancy further in the fall. The reason

being that, by dropping single plates near a *fixed* wall, we assumed that the fluid velocity on the vertical centerline of the domain is zero. This assumption is not entirely correct, at least for the vertical component of the velocity, given the slip velocity due to shed vortices. Nevertheless, the lateral fluid velocity is negligible as shown on figure 3.4(b), hence justifying our approximation. We will therefore study a single plate falling near a fixed wall.

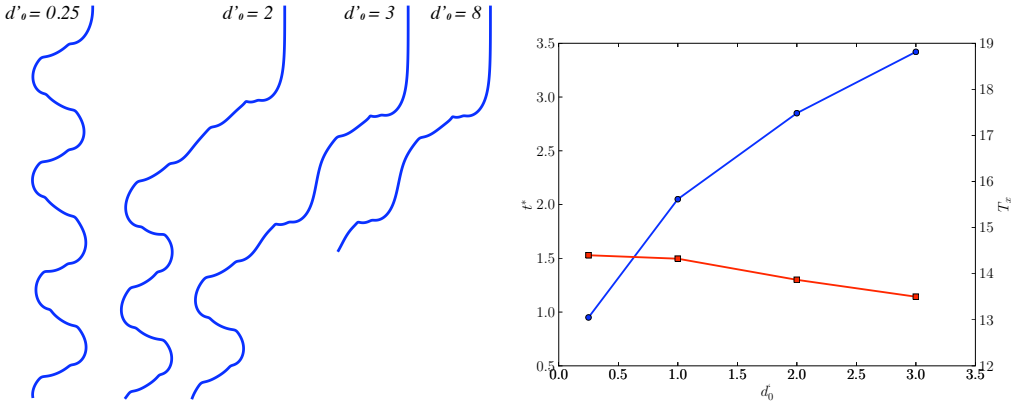

Figure 3.5: *(a) Trajectories of a single falling plate near the right wall, as a function of the initial distance d_0' to the wall. (b) Effect of the wall on t^*, the onset of the deviation from the vertical trajectory (blue, circle) and on the fluttering period T_x at steady state (red, squares). $Re = 200$.*

Figure 3.5(a) shows trajectories of a plate falling near the right wall, for different initial spacings $0.25 \leq d_0' \leq 8$. The nature of the dynamics changes considerably. The motion is predominantly a fluttering mode, the closer the plate is to the wall. Each flutter is comprised of two tumbles at $d_0' = 0.25$. When d_0' increases, the transients are predominantly a period-one tumbling motion, for $d_0' = 2$, and period-two tumbling for $d_0' = 3$. The plate then settles to a fluttering-tumbling motion similar to that for $d_0' = 0.25$. At $d_0' = 8$, the plate settles into a period-two tumbling motion. In terms of two side-by-side falling plates, this means that for an initial spacing $d_0 = 2\,d_0'$ of the order of magnitude of the width

of the plates ($d_0 = 0.5, 4, 6$), the plates will fall close to one another and settle into a fluttering-tumbling steady state motion. When d_0 is an order of magnitude higher than the plate width ($d_0 = 16$), the trajectories of the two plates will separate to the left and right, and settle into a period-two tumbling motion. It thus seems that for small d_0' (less than three), the steady state configuration of the falling plate is that of an overall fluttering motion, with two tumbles within each flutter. Due to the computational cost of the simulations, although halved, we did not pursue a further investigation to determine whether or not the observed dynamics for $d_0' = 8$ were rather transients similar to those for $d_0' = 3$, albeit longer, nor that the plate would eventually settle to a fluttering-tumbling motion. We also could not further determine the value of d_0' at which the bifurcation in the nature of the steady state occurs, i.e a transition from the fluttering-tumbling steady motion to the period-two tumbling.

We now address the question of when the plate deviates from its initial vertical trajectory, and how the onset of deviation is affected by the distance to the wall. Figure 3.5(b) shows that the closer to the wall the plate is initially, the earlier in the fall it deviates from the edge-on position. For the case $d_0' = 8$, not reported here, the onset of deviation is slightly (5%) smaller than at $d_0' = 3$. The fluttering period, albeit slightly decreasing with increasing d_0', remains the constant $T_x \approx 14$ for all $d_0' \leq 3$.

Finally, it is interesting to note that the wall effect (figure 3.5(a)), or equivalently, the presence of a neighboring plate, leads to dynamics similar to those due to the Reynolds number effect (figure 3.2). The curious reader can also view the trajectories for three settling plates in appendix C.

3.4 Effect of the vertical staggering

We further explore how the relative position of two plates affects their dynamics. In section 3.3, we explored the effect of the initial center-to-center spacing. In this section, without delving into the details of the underlying dynamics, we will briefly present qualitative results on the effect of staggering on the dynamics of falling plates, i.e the effect of the relative angular position. Two plates, initially in an edge-on position, are dropped with zero initial velocity. The only difference with section 3.3 is that the plates are not falling from the same height, but have a vertical offset. The initial center-to-center distance is fixed at $d_0 = 2$ and the Reynolds number is $Re = 200$.

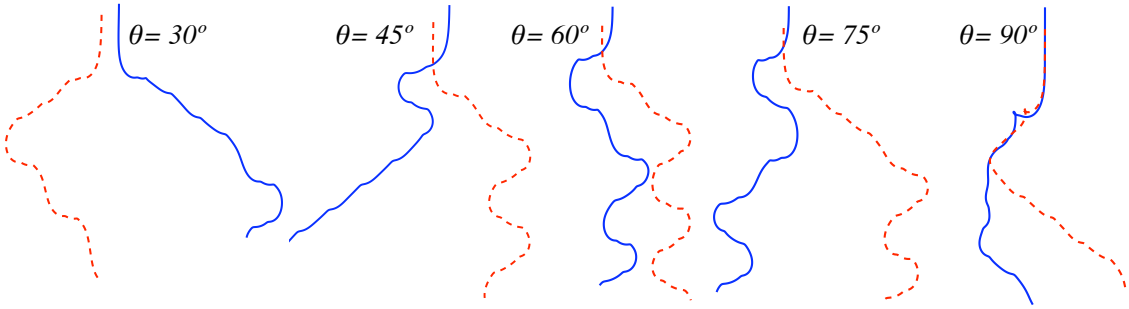

Figure 3.6: *Trajectories of two falling plates, with an initial vertical offset. The initial center-to-center distance is fixed at $d_0 = 2$, and the initial angle between the horizontal and the line of centers of the plates is varied $\theta = 30° \ldots 90°$. Right plate (blue, solid), left plate (red, dashed). $Re = 200$.*

Figure 3.6 shows how the trajectories vary significantly depending on the initial offset. The dynamics of the two plates are either similar, as is the case for $\theta = 60°, 75°$ where the plates settle into the overall fluttering motion, with two tumbles in each flutter. Or they can be different, as is the case for $\theta = 30°, 45°$ where the plates settle either into a period-one tumbling or a

fluttering-tumbling motion. For the case $\theta = 90°$, the plates exhibit full loops and no significant flutter or tumble. The dynamics are inherently complex when parameters such as the number of plates (see appendix C) or the initial spacing are varied, all flow properties remaining the same. A case by case study is thus required to determine the nature of the steady state dynamics and whether synchrony and interesting dynamics take place, for given parameters.

3.5 Conclusion

Using our implementation of the immersed interface method, which enables the simulation of freely moving objects, we studied the dynamics of an edge-on falling plate for different flow conditions and in the presence of another plate. The effect of the Reynolds number was similar to a variation of the non-dimensional moment of inertia of the plate. Our results are in agreement with the dynamical analysis in a previous study on falling plates [1, 2] and show that when $Re < 100$, the plate falls into a damped periodic broadside motion. The side to side motion becomes more noticeable as the Reynolds number increases. At $Re = 100$, the motion is that of a periodic fluttering, with two tumbles in each flutter. This state corresponds to a limit cycle in the $(\theta, \dot{\theta})$ phase plane. Then, for increasing Re, the plate undergoes motions varying from a mix of fluttering and tumbling, to period-one then period-two tumbling.

We then studied how the presence of another falling plate affected the dynamics of the original plate. This study was equivalent to studying the effect of the initial distance to a nearby wall. Our results show that as the distance from the wall increases, the trajectory of the plate was similar to that obtained with

an increasing Reynolds number. That is, the plate trajectory goes from fluttering motion to a mix of fluttering and tumbling then period-two tumbling motion. Additionally, the closer to the wall the plate is initially, the sooner it deviates from its initial edge-on position. The dynamics are further complicated when the plates have an initial vertical offset or when their number is more than two.

CHAPTER 4

SUMMARY

The goal of this research has been a better understanding of the dynamics of particles interacting in a fluid, in the intermediate Reynolds number regime. To do so, we developed a robust implementation of the immersed interface method. The originality of our implementation is the handling of the coupling between the dynamics of the rigid object and the surrounding fluid. This implementation allows for the simulation of freely moving bodies, as opposed to previous versions of the code, where the motion of the objects was prescribed. Our method is almost second-order accurate, including along the interface.

In this thesis, we investigated the dynamics of arrays of settling cylinders at $Re = 200$. In particular, we studied how the dynamics and falling pattern depended on the initial conditions. We found that the array reached a dynamic steady state, the configuration of which depended on the number of particles, n, and the initial inter-particle spacing, d_0. Namely, when n was odd, the middle cylinder was always leading, and the array had a concave up falling pattern for $n = 3$ and a "M" shape for $n > 3$. Conversely, when n was even, the array had a concave down falling pattern. In all cases, there was a left-right mirror symmetry in the rotating and wake pattern of the cylinders; and the outer cylinders always rotate outward. Additionally, the cylinders experienced a weak attractive force during the first time steps, followed by a strong repulsive force. This latter, whose magnitude increased with decreasing initial inter-particle spacing, caused the array to spread laterally. Given the complexity of these dynamics, we focused on an array of $n = 3$ falling cylinders and studied the effect of the initial spacing on the dynamics of the middle cylinder. Our results show that

the presence of the left and right neighbors caused the middle cylinder to experience a higher drag force, and consequently a slower settling velocity. This result contrasts what is observed in Stokes regime, where a sphere settles faster, in the presence of its neighbors, than an isolated one. Our findings also show that the smaller the initial inter-particle spacing is, the earlier the wake asymmetries arise and the earlier the array reaches the dynamic steady state.

When the particle density is high, collisions become unavoidable and it behooves us to treat the close-range interactions and solve for the flow when the current numerics fail. When the distance between the interfaces of two objects or an object and a wall is less than three grid points, the interpolation scheme in the immersed interface method, which is based on three-point stencil finite differences, fails. Unlike other numerical methods where *ad hoc* kludges, such as the addition of a repulsive force, are used, we proceed by directly incorporating the solutions to the Reynolds equations into the numerical scheme. The velocity and pressure gradient fields in the gap region are solved analytically in the lubrication limit. The solutions are then used in the expression of the singular force densities, which are used in solving the dynamics of the object and updating the flow field. We validated our implementation by providing three test cases: cylinder falling vertically toward a fixed wall, fixed cylinder above a translating wall and rotating cylinder above a fixed wall. These cases summarize the fundamental features of normal and oblique collisions. Our numerical results agree with both our analytic solutions and theoretical results from the literature, indicating the validity of our implementation.

Finally, we presented results on the dynamics of edge-on falling plates using the immersed interface method. Specifically, for a fixed plate geometry, we

studied the effect of the Reynolds number on the dynamics and trajectory of the falling plate and asked if its effect is similar to a variation of the moment of inertia of the plate. Our results show that it is indeed the case. Specifically, when $Re < 100$, the plate falls into a periodic broadside motion. At $Re = 100$, the plate undergoes a periodic fluttering with two tumbles in each flutter. This state corresponds to a limit cycle in the $(\theta, \dot{\theta})$ phase plane and is qualitatively different from the tumble-free fluttering motion in [1, 2]. As the Reynolds number increases, the plate starts to tumble in period-one then period-two tumbling motion. Together, these results agree with the dynamical analysis carried out by Andersen *et al.* [1, 2]. We then studied how the dynamics of the plate were affected by the presence of another plate. This configuration was equivalent to studying the effect of a wall at half distance from the plate. Our results show that increasing the initial distance d_0' from the wall produced dynamics similar to those obtained by increasing the Reynolds number for a single plate. That is, as the value of d_0' increased, the plate went through a fluttering motion, then a mix of fluttering and tumbling, followed by a period-one then period-two tumbling motion. Moreover, the smaller d_0' was, the earlier the plate deviated from its edge-on configuration. In terms of two plates, our results show that their dynamics are synchronized and are the mirror symmetry of each other with respect to the centerline of the numerical domain. This observation ceased to hold when the plates had an initial vertical offset.

Future work using the current version of the immersed interface method, which handles both freely moving objects and collisions, would focus on particle-particle collisions in large collections of particles, be they cylinders or other geometries, such as plates. The derivation of the analytical solution for two cylinders in close-range interaction has been presented in this thesis (see

appendix B) and the code is currently in progress for a vertical chain of two settling cylinders. The challenge for large clusters of particles is the necessity to provide analytic solutions to the lubrication equations for at least each pair of particles. Computationally, this will require a more efficient algorithmic implementation as well as faster machines.

APPENDIX A

CONSERVATION OF THE TOTAL CIRCULATION

For n objects immersed in a fluid, with zero total (object and fluid) initial angular momentum, we ask if the total circulation is conserved at all times. Note that we cannot used Kelvin's theorem as it applies for inviscid, barotropic flows with conservatives forces. Figure A.1 shows a typical configuration. We consider the system $\{objects + fluid\}$ and define ∂B_{ext} as the boundary comprised of the four lateral walls of the computational domain, ∂B_k as the boundary of the object k and $\partial B_{tot} = \partial B_{ext} + \bigcup_{k=1}^{n} \partial B_k$ as the entire oriented circuit on figure A.1. The straight close lines, oriented in opposite directions, are also part of ∂B_{tot}. So,

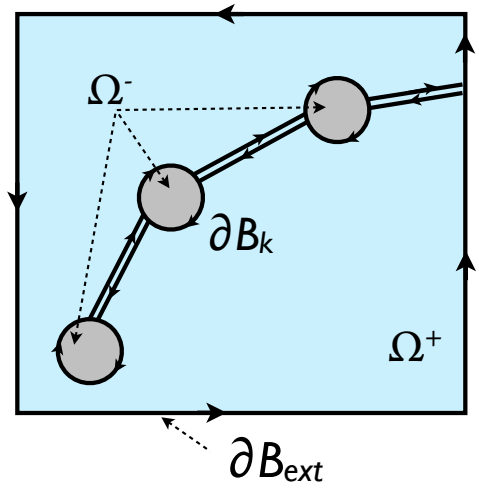

Figure A.1: *Sketch of objects immersed in a fluid. ∂B_{ext} is the boundary of the computational domain (four side walls) and ∂B_k is the interface of object k. The shaded region, Ω^-, is modeled as solid fluid in the numerical code. The fluid domain, outside the objects, is Ω^+.*

our question is $C_{tot}(t) \stackrel{?}{=} C_{tot}(0) = 0\,,\ \forall\ t$, where C_{tot} is the circulation around the numerical domain, i.e around the boundary ∂B_{ext}. The fluid velocity, $\vec{v}$, does not have continuous first partial derivatives across the total domain given the presence of the fluid-solid interfaces. Hence, we cannot directly use Stokes theorem

in the domain $\Omega^+ \cup \Omega^-$, but on Ω^+ and Ω^- separately (see figure A.1 or figure 1.1, p. 5).

∂B_{tot} is a simple, smooth, closed, simply connected and positively oriented contour, and $\vec{v}$ has continuous first partial derivatives in Ω^+. Using Stokes theorem, we have

$$\oint_{\partial B_{tot}} \vec{v} \cdot d\vec{s} = \iint_{\Omega^+} \vec{\omega} \cdot \vec{n}\, dA^+ \,. \tag{A.1}$$

But

$$\oint_{\partial B_{tot}} \vec{v} \cdot d\vec{s} = \oint_{\partial B_{ext}} \vec{v} \cdot d\vec{s} - \sum_{k=1}^{n} \iint_{\partial A_k} \vec{\omega}_k \cdot \vec{n}_k\, dA_k \tag{A.2}$$

where $d\vec{s}_k = a d\theta\, \hat{e}_{\theta_k}$. The integrals along the straight lines cancel out, since the lines are oppositely oriented and are separated by a distance $\delta \to 0$. On ∂B_k, we use the no-slip boundary condition and obtain $\vec{v}_k = a\dot{\theta}_k\, \hat{e}_{\theta_k}$. Hence

$$\begin{aligned} \oint_{\partial B_k} \vec{v}_k \cdot d\vec{s}_k &= \dot{\theta}_k a^2 . 2\pi \\ &= \underbrace{(2\dot{\theta}_k)}_{\omega_k} \underbrace{(a^2\pi)}_{A_k} \\ &= \iint_{A_k} \vec{\omega}_k \cdot \vec{n}_k\, dA_k \end{aligned}$$

Using this final result back into equations A.1 – A.2, we have

$$\oint_{\partial B_{tot}} \vec{v} \cdot d\vec{s} = \underbrace{\iint_{\Omega^+} \vec{\omega} \cdot \vec{n}\, dA^+}_{C^+} = \underbrace{\oint_{\partial B_{ext}} \vec{v} \cdot d\vec{s}}_{C_{tot}} - \underbrace{\iint_{\Omega^-} \vec{\omega} \cdot \vec{n}\, dA^-}_{C^-} \tag{A.3}$$

$$\therefore \;\; C_{tot}(t) = \oint_{\partial B_{ext}} \vec{v} \cdot d\vec{s} = \iint_{\Omega^+ \cup \Omega^-} \vec{\omega} \cdot \vec{n}\, dA$$

The area integral on $\Omega^+ \cup \Omega^-$ can be computed numerically at each time step. We found that for all time, $C_{tot}(t) = 0$. Hence, the total circulation is conserved.

APPENDIX B

SOLUTION TO THE REYNOLDS EQUATIONS IN THE GENERAL CASE OF TWO INTERACTING CYLINDERS

B.1 Velocity and pressure gradient

We consider the case of two cylinders in close contact. We define the local co-moving coordinate system (ξ, η) such that the η-direction is along the line of centers from object (1) to object (2) and ξ is perpendicular to η. We define the angle $\beta \triangleq \angle(\hat{x}, \hat{\eta})$ and treat the case where $\beta \not\equiv 0[\pi]$. We write and solve the

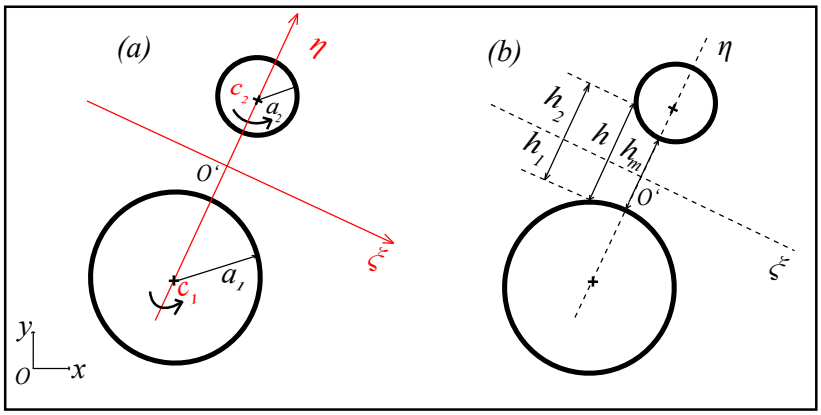

Figure B.1: *Sketch of two cylinders in close contact. (ξ, η) is the local coordinate system. (a) The radii of the cylinders are a_1 and a_2. (b) At abscissa ξ, the separation is $h = h_2 - h_1$. h_m is the minimum separation, at $\xi = 0$.*

Reynolds equation using the (ξ, η) coordinate system. We use the notation (x, y) and (u, v) for the coordinates and velocity components in the fixed lab frame $(\hat{x}, \hat{y})$, and (ξ, η) and (u', v') for the coordinates and velocity components in the

co-moving frame $(\hat{\xi}, \hat{\eta})$. Reynolds equations 2.4 become

$$\frac{\partial u'}{\partial \xi} + \frac{\partial v'}{\partial \eta} = 0 \tag{B.1}$$

$$-\frac{\partial p}{\partial \xi} + \frac{1}{Re}\frac{\partial^2 u'}{\partial \eta^2} = 0 \tag{B.2}$$

By the same token (see section 2.2.2), we can show that $p = p(\xi)$. The equations for the velocity and pressure gradient become

$$u' = u'_1 + \frac{u'_2 - u'_1}{h}(\eta - h_1) + \frac{Re}{2}\frac{dp}{d\xi}\left((\eta - h_1)^2 - (\eta - h_1)\,h\right) \tag{B.3}$$

$$\frac{\partial h}{\partial t} + \frac{\partial}{\partial \xi}(\overline{u'}h) + u'_1\frac{\partial h_1}{\partial \xi} - u'_2\frac{\partial h_2}{\partial \xi} = \frac{Re}{12}\frac{\partial}{\partial \xi}\left(h^3\frac{dp}{d\xi}\right) \tag{B.4}$$

where

$$u'_1 = \dot{x}_{c_1}\sin\beta - \dot{y}_{c_1}\cos\beta - \dot{\theta}_1\sqrt{a_1^2 - \xi^2} \tag{B.5}$$

$$u'_2 = \dot{x}_{c_2}\sin\beta - \dot{y}_{c_2}\cos\beta + \dot{\theta}_2\sqrt{a_2^2 - \xi^2} \tag{B.6}$$

are the velocities, along $\hat{\xi}$, of a point on the object "1" or "2", at abscissa ξ, and $\overline{u'} = (u'_1 + u'_2)/2$. $(\dot{x}_{c_i}, \dot{y}_{c_i})$ are the velocities of the object "i", projected in the $(\hat{x}, \hat{y})$ frame. h_1 and h_2 are the algebraic heights from the ξ-axis

$$h_{1,2}(\xi, t) = \mp\left(\frac{h_m(t)}{2} + a_{1,2} - \sqrt{a_{1,2}^2 - \xi^2}\right)$$

$h = h_2 - h_1$ and h_m is the minimum gap clearance, i.e the value of h at $\xi = 0$. Using these expressions, we can solve for the pressure gradient in equation B.4

$$\begin{aligned}\frac{dp}{d\xi} = \frac{12}{Re}\Bigg\{&\frac{\overline{u'}}{h^2} + \frac{\dot{h}\xi}{h^3} + \frac{(\dot{x}_{c_1}\sin\beta - \dot{y}_{c_1}\cos\beta)\sqrt{a_1^2 - \xi^2}}{h^3} + \\ &\frac{(\dot{x}_{c_2}\sin\beta - \dot{y}_{c_2}\cos\beta)\sqrt{a_2^2 - \xi^2}}{h^3} - \frac{(\dot{\theta}_2 - \dot{\theta}_1)\xi^2}{2h^3} + \frac{C(t)}{h^3}\Bigg\}\end{aligned} \tag{B.7}$$

where $C(t)$ is a constant of integration. In the immersed interface method code, which uses a cartesian grid, one has to give the expressions of the local coordinates (ξ,η) in terms of (x, y). Consider a point $P_{1,2}$ on object "1,2". Then,

$$\begin{aligned} \overrightarrow{O'P_{1,2}} = \xi_{1,2}\,\hat{\xi} + \eta_{1,2}\,\hat{\eta} &= \overrightarrow{O'C_{1,2}} - \overrightarrow{OC_{1,2}} + \overrightarrow{OP_{1,2}} \\ &= \vec{x}_{s_{1,2}} - \vec{x}_{c_{1,2}} \mp \left(\frac{h_m}{2} + a_{1,2}\right)\hat{\eta} \end{aligned} \tag{B.8}$$

where $\vec{x}_{s_i}$ are the cartesian coordinates of P_i, $\vec{x}_{c_i}$ are the cartesian coordinates of the center of mass C_i of object "i", and O and O' are the origins of the lab and co-moving frames, respectively. We project equation B.8 onto $(\hat{\xi}, \hat{\eta})$ and obtain

$$\xi_{1,2} = (x_{s_{1,2}} - x_{c_{1,2}})\sin\beta - (y_{s_{1,2}} - y_{c_{1,2}})\cos\beta \tag{B.9}$$

$$\eta_{1,2} = (x_{s_{1,2}} - x_{c_{1,2}})\cos\beta + (y_{s_{1,2}} - y_{c_{1,2}})\sin\beta \mp \left(\frac{h_m}{2} + a_{1,2}\right) \tag{B.10}$$

The expression of $\xi_{1,2}$ will be used in equation B.4. To find the value of $C(t)$, we

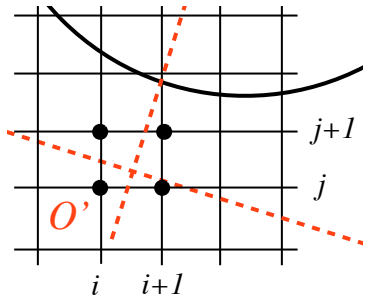

Figure B.2: *Sketch of the (ξ, η) point and the cartesian grid points used for the interpolation of the velocity u'.*

match the velocity field from numerics with the expression given from solving Reynolds equations (equation B.3) at any arbitrary point in the lubrication region. The most straightforward case is to match the velocity at O', the origin of the (ξ, η) system. We proceed by finding the corresponding cartesian coordinates, then the four surrounding grid points and average the velocities as

follows. See figure B.2.

$$\overrightarrow{OO'} = \vec{x}_{o'} = \overrightarrow{OC_1} + \overrightarrow{C_1O'} = \vec{x}_{c_1} + \left(\frac{h_m}{2} + a_1\right)\hat{\eta}$$

That is,

$$\begin{aligned} x_{o'} &= x_{c_1} + \left(\tfrac{h_m}{2} + a_1\right)\cos\beta \\ y_{o'} &= y_{c_1} + \left(\tfrac{h_m}{2} + a_1\right)\sin\beta \end{aligned}$$

The coordinates $(x_{o'}, y_{o'})$ fall in a grid cell whose vertices are (i, j), $(i+, j)$, $(i, j+1)$, $(i+1, j+1)$, as shown on figure B.2, where

$$i = \left\lfloor \frac{x_{o'} - (x_0 + \Delta x/2)}{\Delta x} \right\rfloor \quad , \quad j = \left\lfloor \frac{y_{o'} - (y_0 + \Delta y/2)}{\Delta y} \right\rfloor$$

where the $\lfloor\bullet\rfloor$ symbol refers to the floor function and $(x_0 + \Delta x/2, y_0 + \Delta y/2)$ are the coordinates of the bottom left corner of the numerical domain. We approximate the velocity at O' by doing a linear interpolation

$$u^N_{o'} \approx \frac{1}{4}\left(u_{i,j} + u_{i+1,j} + u_{i,j+1} + u_{i+1,j+1}\right) \tag{B.11}$$

where the superscript "N" refers to numerical data. Note that one could use a bilinear interpolation, where the relative distance to the grid cell walls is taken into account. The limit cases where the point O' falls on a grid line or at a vertex are left as an exercise to the reader. The transformation from the (ξ, η) to the (x, y) system, in term of the velocity u is

$$u = u'\sin\beta + v'\cos\beta \approx u'\sin\beta \quad (v' \ll u')$$

Therefore, to get the constant $C(t)$, we enforce the following velocity matching at O', where $(\xi_{o'}, \eta_{o'}) = (0, 0)$

$$u^N_{o'} = u^L_{o'} = u'_{o'}\sin\beta \tag{B.12}$$

where the superscript "L" refers to the analytical data using the lubrication velocity, and

$$u'_{o'} = \left[u'_1 + \frac{u'_2 - u'_1}{h}(\eta - h_1) + \frac{Re}{2}\frac{dp}{d\xi}\left((\eta - h_1)^2 - (\eta - h_1)\,h\right)\right]_{(\xi,\eta)=(0,0)}$$

Hence

$$u'_{o'} = \frac{u^N_{o'}}{\sin\beta} = \frac{u'_{1_{o'}} + u'_{2_{o'}}}{2} - \frac{Re\, h_m^2}{8}\left(\frac{dp}{d\xi}\right)_0 \qquad \text{at } \xi = 0 \tag{B.13}$$

Using equation B.4 at $\xi = 0$, we have

$$\left(\frac{dp}{d\xi}\right)_0 = \frac{12}{Re}\left\{\frac{u'_{1_{o'}} + u'_{2_{o'}}}{2\, h_m^2} + \frac{a_1(\dot{x}_{c_1}\sin\beta - \dot{y}_{c_1}\cos\beta) + a_2(\dot{x}_{c_2}\sin\beta - \dot{y}_{c_2}\cos\beta) + C(t)}{h_m^3}\right\} \tag{B.14}$$

where

$$u'_{1,2_{o'}} = \dot{x}_{c_{1,2}}\sin\beta - \dot{y}_{c_{1,2}}\cos\beta \pm a_{1,2}\dot{\theta}_{1,2}$$

Combining equations B.13 and B.14, we finally obtain

$$C(t) = -\left\{\frac{(u'_{1_{o'}} + u'_{2_{o'}})\, h_m}{6} + \frac{2u^N_{o'} h_m}{3\sin\beta} + a_1(\dot{x}_{c_1}\sin\beta - \dot{y}_{c_1}\cos\beta) + a_2(\dot{x}_{c_2}\sin\beta - \dot{y}_{c_2}\cos\beta)\right\} \tag{B.15}$$

where $u^N_{o'}$ is given by equation B.11.

B.2 Singular force density

The tangential and the derivative of the normal component of the singular force density are

$$f_\tau = -\frac{1}{Re}(\omega^+ - \omega^-) \tag{B.16}$$

$$\frac{\partial f_n}{\partial \alpha} = J\left\{\frac{1}{Re}\left[\frac{\partial \omega}{\partial n}\right] + [b_\tau]\right\} \tag{B.17}$$

where $\omega^- = 2\dot{\theta}$, $[b_\tau] = -\ddot{\theta}\left((x_s - x_c)\, n_x + (y_s - y_c)\, n_y\right.$ (see [59]) and

$$\omega^+ = \frac{\partial v'}{\partial \xi} - \frac{\partial u'}{\partial \eta} \approx -\frac{\partial u'}{\partial \eta}$$

Thus,

$$f_\tau = \frac{1}{Re}\left(\frac{\partial u'}{\partial \eta} + 2\,\dot{\theta}\right)$$

We use the derivative, with respect to η, of equation B.3 at $\eta = h_{1,2}$ and finally obtain

$$f_{\tau_{1,2}} = \frac{1}{Re}\left(\frac{u_2' - u_1'}{h} \mp \frac{Re\, h}{2}\frac{dp}{d\xi} + 2\,\dot{\theta}_{1,2}\right) \tag{B.18}$$

where u_1' and u_2' are given by equations B.5 and B.6. The first shear term is due to the Couette flow contribution, the second to the Poiseuille contribution, and the third to the solid body rotation.

Similarly, for the normal component, we have $[\partial\omega/\partial n] = (\partial\omega/\partial n)^+$ since $\omega^- = 2\dot{\theta}$ is uniform. The normal derivative is

$$\frac{\partial\omega}{\partial n} = \nabla\omega \cdot \hat{n} = \frac{\partial\omega}{\partial\xi}\, n_\xi + \frac{\partial\omega}{\partial\eta}\, n_\eta$$

The local coordinates of $\hat{n}$ are (see figure B.3)

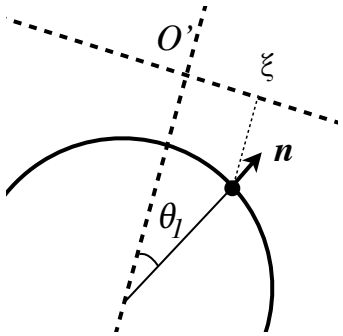

Figure B.3: *Sketch of the unit normal to object "1" at the abscissa ξ, and an angle θ_1 with the η-axis.*

$$\hat{n}_{1,2} = (\cos\theta_{1,2}, \pm\sin\theta_{1,2}) = \left(\frac{\xi}{a_{1,2}}, \pm\sqrt{1 - \xi^2/a_{1,2}^2}\right)$$

In the lubrication region, we always have $|\theta| < \pi/4$, thus $n_\xi < n_\eta$; and given that $|\partial\omega/\partial\xi| \ll |\partial\omega/\partial\eta|$, we have

$$\left[\frac{\partial\omega}{\partial n}\right] \approx \frac{\partial\omega}{\partial\eta}\, n_\eta \approx -\frac{\partial^2 u'}{\partial\eta^2}\, n_\eta \;\text{ where : }\; \frac{\partial^2 u'}{\partial\eta^2} = Re\frac{dp}{d\xi}$$

Finally

$$\left.\frac{\partial f_n}{\partial\alpha}\right|_{1,2} = J\left\{\mp\frac{dp}{d\xi}\sqrt{1 - \xi^2/a_{1,2}^2} - \ddot{\theta}_{1,2}((x_{s_{1,2}} - x_{c_{1,2}})\, n_{1,2}^x + (y_{s_{1,2}} - y_{c_{1,2}})\, n_{1,2}^y\right\} \tag{B.19}$$

APPENDIX C

TRAJECTORY OF MULTIPLE FALLING PLATES

As an extra for the reader and as a follow up for section 3.3, figure C.1 shows the trajectories of three falling plates, at $Re = 200$, with an initial center-to-center spacing $d_0 = 0.5$. The left and right plates start out with a period-one tumbling motion, and drift apart anti-symmetrically. They then settle into a mix of fluttering and period-two tumbling motion. The middle plate initially glides for a long period of time before settling into a mix of period-one and period-two tumbling motion.

Figure C.1: *Trajectory snapshots of three falling plates with initial spacing* $d_0 = 0.5$. $Re = 200$.

At this Reynolds number regime (intermediate) and as the number of plates increases, the nature of the dynamics and the trajectories become unpredictable, thus requiring case by case studies.

BIBLIOGRAPHY

[1] A. Andersen, U. Pesavento, and Z. J. Wang. Analysis of transitions between fluttering, tumbling and steady descent of falling cards. *J. Fluid Mech.*, 541:91–104, 2005.

[2] A. Andersen, U. Pesavento, and Z. J. Wang. Unsteady aerodynamics of fluttering and tumbling plates. *J. Fluid Mech.*, 541:65–90, 2005.

[3] A. M. Ardekani, S. Dabiri, and R. H. Rangel. Collision of multi-particle and general shape objects in a viscous fluid. *J. of Comp. Phys.*, 227:10094–10107, 2008.

[4] A. M. Ardekani and R. H. Rangel. Unsteady motion of two solid spheres in stokes flow. *Phys. of Fluids*, 10(103306), 2006.

[5] P. W. Bearman and A. J. Wadock. The interaction between a pair of circular cylinders normal to a stream. *J. Fluid Mech.*, 61:499–511, 1973.

[6] J. Brady and G. Bossis. Stokesian dynamics. *Ann. Rev. of Fluid Mech.*, 20:111–157, 1988.

[7] S. J. Bussell, D. L. Koch, and D. A. Hammer. The resistivity and mobility functions for a model system of two equal-sized proteins in a lipid bilayer. *J. Fluid Mech.*, 243:679–697, 1992.

[8] L. H. Cisneros, R. Cortez, C. Dombrowski, R. E. Goldstein, and J. O. Kessler. Fluid dynamics of self-propelled microorganisms, from individuals to concentrated populations. *Exp. Fluids*, 43:737–753, 2007.

[9] M. D. A. Cooley and M. E. O'Neill. On the slow motion generated in a viscous fluid by the approach of a sphere to a plane wall or a stationary sphere. *Mathematica*, 16:37–49, 1969.

[10] I. D. Couzin and J. Krause. Self-organization and collective behaviour in vertebrates. *Adv. Study Behav.*, 32:1–75, 2003.

[11] J. M. Crowley. Viscosity induced instability of a one-dimensional lattice of falling spheres. *J. Fluid Mech.*, 45:151–159, 1971.

[12] A. Czirók and T. Vicsek. Collective behavior of interacting self-propelled particles. *Physics A*, 281:17–29, 2006.

[13] W. B. Daniel, R.E. Ecke, G. Subramanian, and D Koch. Clusters of sedimenting high-reynolds number particles. *J. Fluid Mech.*, 625:371–385, 2009.

[14] N. C. Darnton, L. Turner, S. Rojevsky, and H. C. Berg. Dynamics of bacterial swarming. *Biophys. J.*, 98(10):2082–2090, 2010.

[15] R. H. Davis. Effects of surface roughness on a sphere sedimenting through a dilute suspension of neutrally buoyant spheres. *Phys. of Fluids A*, 4(12):2607–2619, 1992.

[16] R. H. Davis, J-M. Serayssol, and E. J. Hinch. The elastohydrodynamic collision of two spheres. *J. Fluid Mech.*, 163:479–497, 1986.

[17] M. L. Ekiel-Jeżewska, B. Metzger, and É. Guazzelli. Spherical cloud of point particles falling in a viscous fluid. *Phys. of Fluids*, 18(038104), 2006.

[18] A. El-Yacoubi, S. Xu, and Z. J. Wang. Computational study of the interaction of freely moving particles at intermediate reynolds numbers. *J. Fluid Mech.*, 705:134–158, 2012.

[19] A. El-Yacoubi, S. Xu, and Z. J. Wang. On the handling of particle collisions in a viscous fluid using the lubrication equations in the immersed interface method. *J. Fluid Mech.*, xxx:xx–xx, 2012.

[20] J. Feng, H. H. Hu, and D. D. Joseph. Direct numerical simulation of initial value problems for the motion of solid bodies in a newtonian fluid. part i. sedimentation. *J. Fluid Mech.*, 261:95–134, 1994.

[21] A. F. Fortes, D. D. Joseph, and T. S. Lundgren. Nonlinear mechanics of fluidization of beds of spherical particles. *J. Fluid Mech.*, 177:467–483, 1987.

[22] A. Gopinath, S. B. Chen, and D. L. Koch. Lubrication flows between spherical particles colliding in a compressible non-continuum gas. *J. Fluid Mech.*, 344:245–269, 1997.

[23] T. Gregor, K. Fujimoto, N. Masaki, and S. Sawai. The onset of collective behavior in social amoebae. *Science*, 328(5981):1021–1025, 2010.

[24] É. Guazzelli and J. Hinch. Fluctuations and instability in sedimentation. *Ann. Rev. of Fluid Mech.*, 43:97–116, 2011.

[25] J. Happel and H. Brenner. *Low Reynolds number hydrodynamics: with special applications to particulate media (Mechanics of Fluids and Transport Processes)*. Springer, 1973.

[26] J. Happel and R. Pfeffer. The motion of two spheres following each other in a viscous fluid. *A.I.Ch.E*, 6(1):129–133, 1960.

[27] J. P. Hernandez-Ortiz, C. G. Stoltz, and M. D. Graham. Transport and collective dynamics in suspensions of confined swimming particles. *Phys. Rev. Lett.*, 95(204501), 2005.

[28] L. M. Hocking. The behavior of clusters of spheres falling in a viscous fluid. part 2: slow motion theory. *J. Fluid Mech.*, 20:129–139, 1963.

[29] P. J. Ireland and L. R. Collins. Direct numerical simulation of inertial particle entrainment in a shearless mixing layer. *J. Fluid Mech.*, 704:301–332, 2012.

[30] K. O. L. F. Jayaweera and B. J. Mason. The behavior of clusters of spheres falling in a viscous fluid. part 1: experiment. *J. Fluid Mech.*, 20:121–128, 1963.

[31] K. O. L. F. Jayaweera and B. J. Mason. The behavior of freely falling cylinders and cones in a viscous fluid. *J. Fluid Mech.*, 22:709–720, 1965.

[32] D. J. Jeffrey and Y. Onishi. The slow motion of a cylinder next to a plane wall. *Q. Jl. Mech. Appl. Math.*, XXXIV, Pt. 2:129–137, 1981.

[33] M. Jenny, J. Dušek, and G. Bouchet. Instabilities and transition of a sphere falling or ascending freely in a newtonian fluid. *J. Fluid Mech.*, 508:201–239, 2004.

[34] D. D. Joseph, A. F. Fortes, T. S. Lundgren, and P. Singh. Nonlinear mechanics of fluidization of beds of spheres, cylinders and disks in water. *Adv. in Multiphase Flow and Related Problems (ed. G. Papanicolau), SIAM*, pages 101–122, 1987.

[35] G. G. Joseph and M. L. Hunt. Oblique particle-wall collisions in a liquid. *J. Fluid Mech.*, 510:71–93, 2004.

[36] G. G. Joseph, R. Zenit, M. L. Hunt, and A. M. Rosenwinkel. Particle-wall collisions in a viscous fluid. *J. Fluid Mech.*, 433:329–346, 2000.

[37] S. Kang. Characteristics of flow over two circular cylinders in a side-by-side arrangement at low reynolds numbers. *Phys. of Fluids*, 15(9):2486–2498, 2003.

[38] K. Katija and J. O. Dabiri. A viscosity-enhanced mechanism for biogenic ocean mixing. *Nature*, 460:624–627, 2009.

[39] I. Kim, S. Elghobashi, and W. Sirignano. Three-dimensional flow over two spheres placed side by side. *J. Fluid Mech.*, 246:465–488, 2005.

[40] M. Kim and K. S. Breuer. Enhanced diffusion due to motile bacteria. *Phys. of Fluids*, 16(L78), 2004.

[41] D. L. Koch and G. Subramanian. Collective hydrodynamics of swimming microorganisms: living fluids. *Ann. Rev. of Fluid Mech.*, 43:637–659, 2011.

[42] H. Kurtudlu, J. S. Guasto, K. A. Johnson, and J. P. Gollub. Enhancement of biomixing by swimming algal cells in two-dimensional films. *PNAS*, 108(26):10391–100395, 2011.

[43] Z. Li, X. Wan, K. Ito, and S. R. Lubkin. An augmented approach for the pressure boundary condition in a stokes flow. *Comm. in Comp. Phys.*, 1:874–885, 2006.

[44] J. R. Meneghini, F. Saltara, C. L. R. Siquiera, and J. A. Jr. Ferrari. Numerical simulation of flow interference between two circular cylinders in tandem and side-by-side arrangements. *J. of Fluids and Struct.*, 15:327–350, 2000.

[45] B. Metzger, M. Nicolas, and É. Guazzelli. Falling clouds of particles in viscous fluids. *J. Fluid Mech.*, 580:283–301, 2007.

[46] N.-Q. Nguyen and A. J. C. Ladd. Lubrication corrections for lattice-boltzmann simulations of particle suspensions. *Phys. Review E*, 66(046708):1–12, 2002.

[47] H. S. Niwa. Self-organizing dynamic model of fish schooling. *J. of Theo. Bio.*, 171(2):123–136, 1994.

[48] M. E. O'Neill and K. Stewartson. On the slow motion of a sphere parallel to a nearby plane wall. *J. Fluid Mech.*, 27:705–724, 1966.

[49] T. J. Pedley and J. O. Kessler. Hydrodynamic phenomena in suspensions of swimming microorganisms. *Ann. Rev. of Fluid Mech.*, 24:313–358, 1992.

[50] U. Pesavento and Z. J. Wang. Falling paper: Navier-stokes solutions, model of fluid forces, and center of mass elevation. *Phys. Rev. Lett.*, 93(14), 2004.

[51] O. Reynolds. On the theory of lubrication and its application to mr. beauchamp tower's experiments, including an experimental determination of the viscosity of olive oil. *Phuil. Trans. R. Soc. Lond. A*, 177:228–310, 1886.

[52] D. Saintillan and M. Shelley. Instabilities and pattern formation in active particle suspensions: Kinetic theory and continuum simulations. *Phys. Rev. Lett.*, 100(178103), 2008.

[53] A. S. Sangani and G. Mo. Inclusion of lubrication forces in dynamic simulations. *Phys. of Fluids*, 6(5):1653–1662, 1993.

[54] P. Singh, PH. Caussignac, A. F. Fortes, D. D. Joseph, and T. S. Lundgren. Stability of periodic arrays of cylinders across the stream by direct numerical simulation. *J. Fluid Mech.*, 205:553–571, 1989.

[55] M. Stimson and G. B. Jeffrey. The motion of two spheres in a viscous fluid. *Proc. Royal Soc. of Lon., Series A*, pages 110–126, 1926.

[56] J. L. Thiffeault and S. Childress. Stirring by swimming bodies. *Physics Lett. A*, 374:3487–3490, 2010.

[57] Z. J. Wang and D. Russell. Effect of forewing and hindwing interactions on aerodynamic forces and power in hovering dragonfly flight. *Phys. Rev. Lett.*, 99(148101), 2007.

[58] Z. Warhaft. Laboratory studies of droplets in turbulence: towards understanding the formation of clouds. *Fluid Dyn. Res.*, 41(011201), 2009.

[59] S. Xu. The immersed interface method for simulating prescribed motion of rigid objects in an incompressible viscous flow. *J. of Comp. Phys.*, 227:5045–5071, 2008.

[60] S. Xu and Z. J. Wang. An immersed interface method for simulating the interaction of a fluid with moving boundaries. *J. of Comp. Phys.*, 216:454–493, 2006.

[61] S. Xu and Z. J. Wang. Systematic derivation of jump conditions for the immersed interface method in three-dimensional flow simulation. *SIAM*, 27(6):1948–1980, 2006.

[62] S. Xu and Z. J. Wang. A 3d immersed interface method for fluid-solid interaction. *Comp. Meth. Appl. Mech. Engrg.*, doi:10.1016/j.cma.2007.06.012, 2007.

[63] F. L. Yang and M. L. Hunt. Dynamics of particle-particle collisions in a viscous liquid. *Phys. of Fluids*, 18(12):121506, 2006.